OPTICAL CHARACTERIZATION OF RARE EARTH DOPED GLASSES

A Thesis Submitted to the College of

Graduate Studies and Research

In Partial Fulfillment of the Requirements

For the Degree of Master of Science

In the Department of Electrical and Computer Engineering

University of Saskatchewan

Saskatoon

By

GOKULAKRISHNAN SOUNDARARAJAN

PERMISSION TO USE

In presenting this thesis in partial fulfilment of the requirements for a Postgraduate degree from the University of Saskatchewan, I agree that the Libraries of this University may make it freely available for inspection. I further agree that permission for copying of this thesis in any manner, in whole or in part, for scholarly purposes may be granted by the professor or professors who supervised my thesis work or, in their absence, by the Head of the Department or the Dean of the College in which my thesis work was done. It is understood that any copying or publication or use of this thesis or parts thereof for financial gain shall not be allowed without my written permission. It is also understood that due recognition shall be given to me and to the University of Saskatchewan in any scholarly use which may be made of any material in my thesis.

Requests for permission to copy or to make other use of material in this thesis in whole or part should be addressed to:

Head of the Department of Electrical and Computer Engineering

University of Saskatchewan

Saskatoon, Saskatchewan, Canada, S7N 5A9

ACKNOWLEDGEMENTS

I extend my sincerest gratitude to my supervisor, Dr. S. O. Kasap, for his leadership, patience and encouragement throughout the course of this research. I also thank: my mentor Dr. K. Koughia for his guidance, support and assistance in the interpretation of the experimental data, Dr. George Belev for his help in troubleshooting experimental setups, Dr. Robert Johanson for his invaluable time spent in explaining some key concepts and the University of Saskatchewan for its financial support. Finally, I would like to thank my family, friends and colleagues for their patience, support and encouragement.

ABSTRACT

Optical amplifiers are highly sought-after in optical communications to power boost light signals carrying information. Rare Earth doped glasses have been the medium of choice for optical amplification. It is, therefore, essential to understand the interaction of light with potential host glasses for rare-earths before they could be proposed as suitable candidates. In this research, we have optically characterized three different rare earth doped bulk glasses. The glass samples investigated were Neodymium doped Gallium Lanthanum Sulfide (GLS:Nd), Erbium doped Germanium Gallium Sulfide (GeGaS:Er) and Erbium doped Fluorochlorozirconate (FCZ:Er). The transmission spectra, $T(\lambda)$, was used in identifying the absorption transitions of rare earth ions from the ground level to the various excited levels and in obtaining the optical absorption coefficient, $\alpha(\lambda)$. This in turn was used in determining the Judd-Ofelt parameters, which were then used in obtaining radiative lifetimes of the energy levels of interest. Photoluminescence emission bands were also identified and their shapes were investigated. Finally, a comparison of the Judd-Ofelt lifetime with the experimental decay time was also done. From which, the major decay mechanism of the rare earth ions from the energy level under investigation was concluded.

TABLE OF CONTENTS

LIST OF FIGURES

LIST OF TABLES

LIST OF ABBREVIATIONS

ChGs	chalcogenide glasses
DSC	differential scanning calorimetry
EDFA	erbium doped fiber amplifier
Er	erbium
FCZ	fluorochlorozirconate
GeGaS	germanium gallium sulfide
GLS	gallium lanthanum sulfide
IR	infrared
JO	judd-ofelt
Nd	neodymium
NR	non-radiative
PL	photoluminescence
R	radiative
RE	rare earth
UV	ultraviolet

1. GLASS IN PHOTONICS

1.1 Introduction

The multitude of uses of laser light photons have lead to the term photonics to cover almost all processes that use laser light in science, technology and medicine, except simple conventional optics and illumination [1]. Figure 1.1 shows some of the applications of photonics.

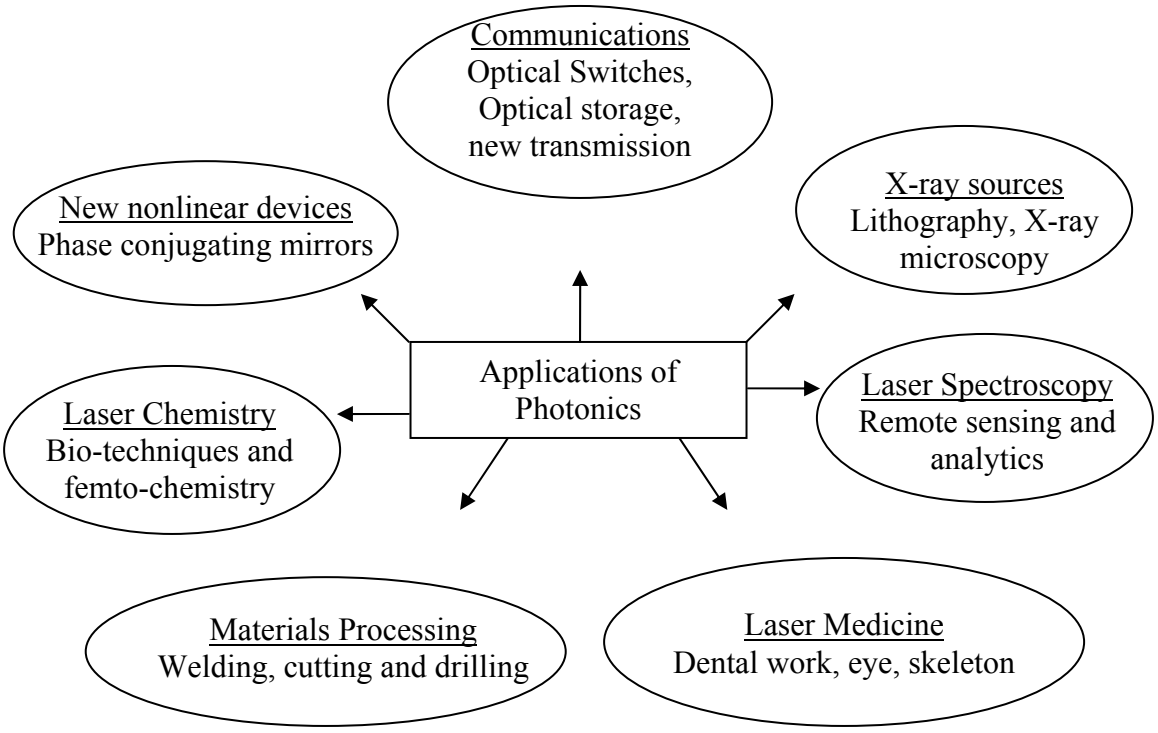

Figure 1.1: Some applications of Photonics [1].

The dream in photonics is to come up with a single chip that would integrate multiple optical technologies, such as amplification, modulation and guiding of light. Integrated photonics can be thought of as the optical counterpart of integrated chips in electronics.

Many of the optical components, such as optical fiber amplifiers, filters, switches, etc, are individually available in the market, but integrating them into one chip would lead to an increase in performance and efficiency and provide cost effective means to produce them.

The difficulty in producing integrated photonic chips is in finding a material that would be a suitable host for various optical devices, as each device requires a distinctive set of host properties for efficient operation [2]. Glasses have been seen as suitable materials for photonic integration due to their diverse attributes. Of the various components used in optical communication systems, optical amplifiers have played a fundamental role. They are used to power boost light signals that carry information in long distance fiber optic communications. It is the advent of optical amplifiers that has given hope for the integration of various communications media, such as computers, telephones, televisions, etc. Glasses doped with rare earth (RE) ions have been the medium of choice for optical amplification. The fundamental concepts involved in optical amplification and the optical properties of rare earth ions will be explained in chapters 2 and 3, respectively.

Although integrated optics is the dream, we're still striving to achieve very efficient optical components in the existing world of optical telecommunications. It is, therefore, imperative to understand the interaction of light with various new materials for us to make more efficient and high performance optical components/devices both for the existing technology and for integrated photonics. In our research, we have optically characterized rare earth doped bulk glass samples to better understand their interaction with light before they could be proposed as suitable candidates for optical amplification. An overview of the unique properties of glasses and their role in photonics is explained below.

1.2 Glass as a Photonics Material

Glasses have played a major role in the world of photonics and optoelectronics. They have applications as both passive (lenses, fibers, windows) and active devices (amplifiers, switches). They are extremely versatile and can be realized into various forms of bulk lenses, thin films and fibers. Unlike polycrystalline materials that have excessive optical losses due to light scattering from grain boundaries, glasses can be manufactured without grain boundaries, therefore, minimizing scattering. As well, the ability to vary the composition gives them an advantage to form various alloys for research in the field of photonics. Further, glasses are primarily known for their transparency ranges. Oxide, halide and chalcogenide glasses are transparent from the ultra violet to the mid-infrared wavelengths as can be seen in Figure 1.2.

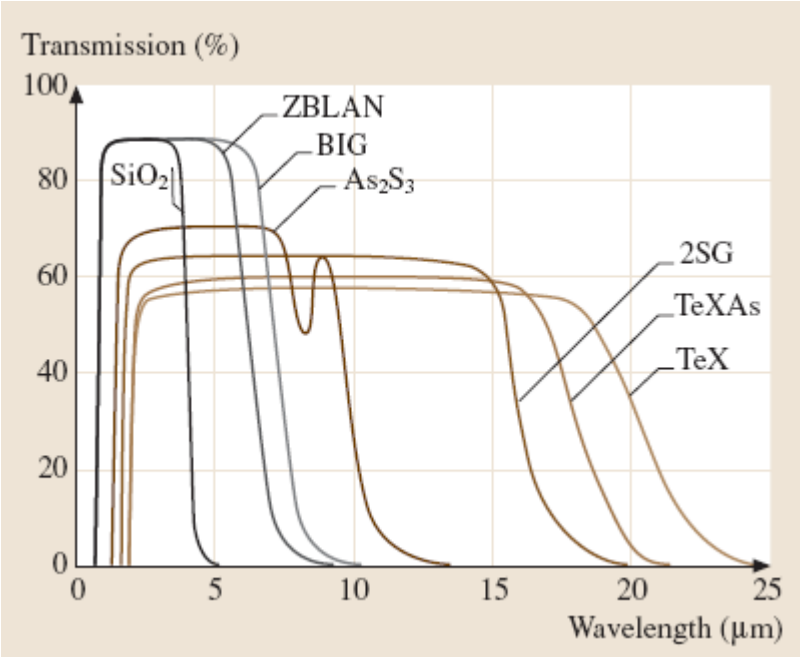

Figure 1.2: Some transmission plots for SiO_2, Chalcogenide and Fluoride glasses. 2SG is a selenide glass, TeXAs and TeX are tellurium-based chalcogenide glasses, and ZBLAN and BIG are heavy-metal fluoride glasses. (After [3])

Glass is formed by the rapid cooling of a viscous liquid. When a liquid is cooled very rapidly the atoms don't have enough time to orient themselves to form a periodic structure. As a result, unlike their crystalline counterpart, glasses do not have long range order and belong to amorphous solids or noncrystalline solids. Figure 1.3 shows the bonding structure for both crystalline and amorphous solids. One of the most crucial characteristics of glass is the presence of what is called a glass transition temperature (T_g). It is below this temperature that the material is an amorphous solid or glass [3]. Figure 1.4 illustrates what happens to a specific volume of glass as temperature changes.

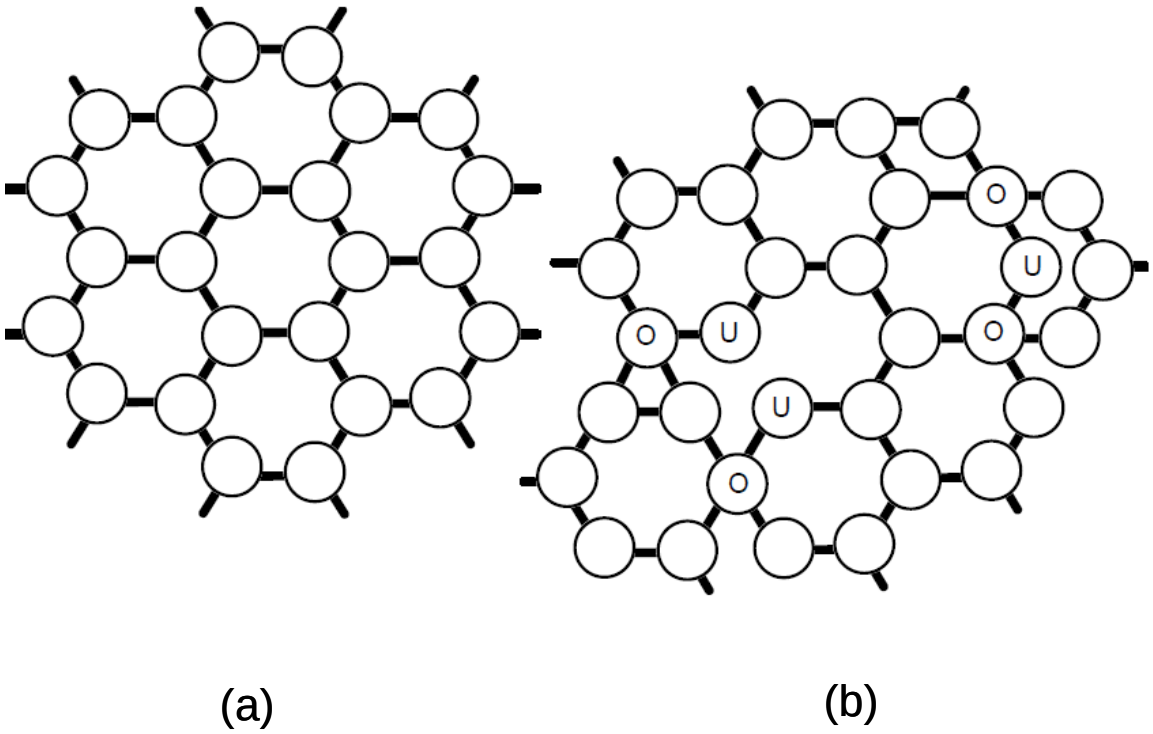

Figure 1.3: A two dimensional representation of (a) a crystalline solid and (b) an amorphous solid. In the amorphous solid, the atoms marked "O" are over-coordinated with more than the usual number of bonds with the adjacent atoms and the atoms marked "U" are under-coordinated with less than the usual number of bonds with the adjacent atoms. (After [4])

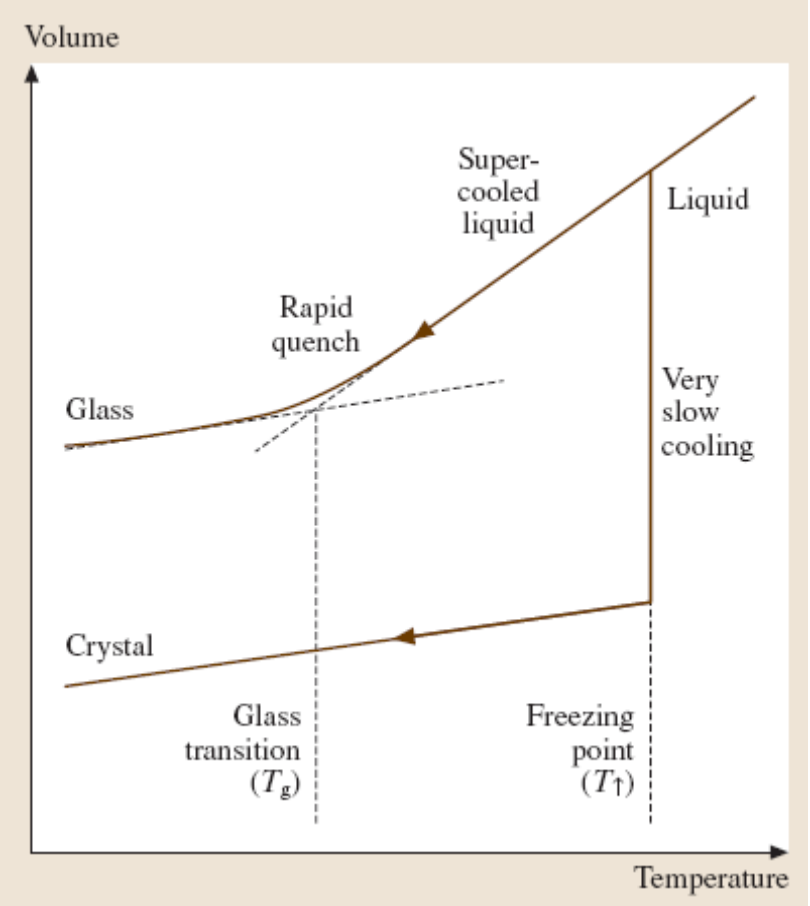

Figure 1.4: Change in specific volume of a glass with temperature. (After [3])

Finally, an important attribute of glasses is their unique ability to accommodate various forms of dopants, such as rare earth ions, metal nanoparticles, or transition metal ions [3]. The random network structure of glasses makes this possible. It is far easier for foreign atoms to find a space to reside inside a glass than a crystal. This feature makes glasses very vital in active photonics. Some glasses can incorporate high concentrations of active ions, which is essential for optical amplification. Of the various glass families, we'll be focusing on chalcogenide and heavy-metal glasses.

1.2.1 Chalcogenide Glasses

Chalcogenide glasses always contain one or more chalcogens, which are elements that belong to group VIB of the periodic table, along with elements from group IIIB, IVB and/or VB. Group VIB elements that are usually seen in many chalcogenide alloys are Sulphur (S), Selenium (Se) and Tellurium (Te). And, group IIIB, IVB and VB elements would be Gallium (Ga), Germanium (Ge), Arsenic (As), Phosphorous (P), Antimony (Sb) etc. GaLaS, GeGaS, GeGaSe, GeSeTe, As_2Se_3 are some examples of chalcogenide glasses (ChGs).

These glasses possess very low phonon energies (phonons are quanta of lattice vibrations), are highly transparent from the visible to the mid-infrared wavelengths, are optically highly non-linear; consequently, they can be useful for all-optical switching (AOL), and are quite sensitive to the absorption of electromagnetic radiation. As a result, under illumination they show a variety of photoinduced changes [5].

Chalcogenide glasses possess many semiconductor properties. Their electronic absorption edge is usually in the visible to near infrared range. As a result, they have high refractive indices that range from 2.2 for sulfide glasses to 3 for telluride glasses [3]. It is the high refractive indices of these glasses that make them suitable candidates for making confining waveguides – the higher the refractive index of the core, the less the amount of light that leaks out of the waveguide. As a result, greater is the efficiency of transmission.

Current optical amplifiers are too long and one of the important research goals is to reduce the size of these amplifiers for integrated photonics. Due to this need in size reduction, the accommodation of dopants (rare earth ions) by the host matrix goes down. As a result, we require host glasses that will accommodate greater concentrations of rare earth ions. Although binary chalcogenide glasses such as GeS_2 and As_2S_3 have limited solubility of RE ions, ternary or multi-component chalcogenide glasses can accommodate

larger concentrations of rare earth ions [6]. Addition of Ga, In, or P, or to a lesser extent, Sn to the binary chalcogenide alloys increases the solubility of rare earth ions to a great extent and reduces clustering [7]. This property along with their low phonon energies make these glasses excellent candidates for the realization of optical amplifiers for integrated optics. Figure 1.5 shows some bulk chalcogenide glass samples.

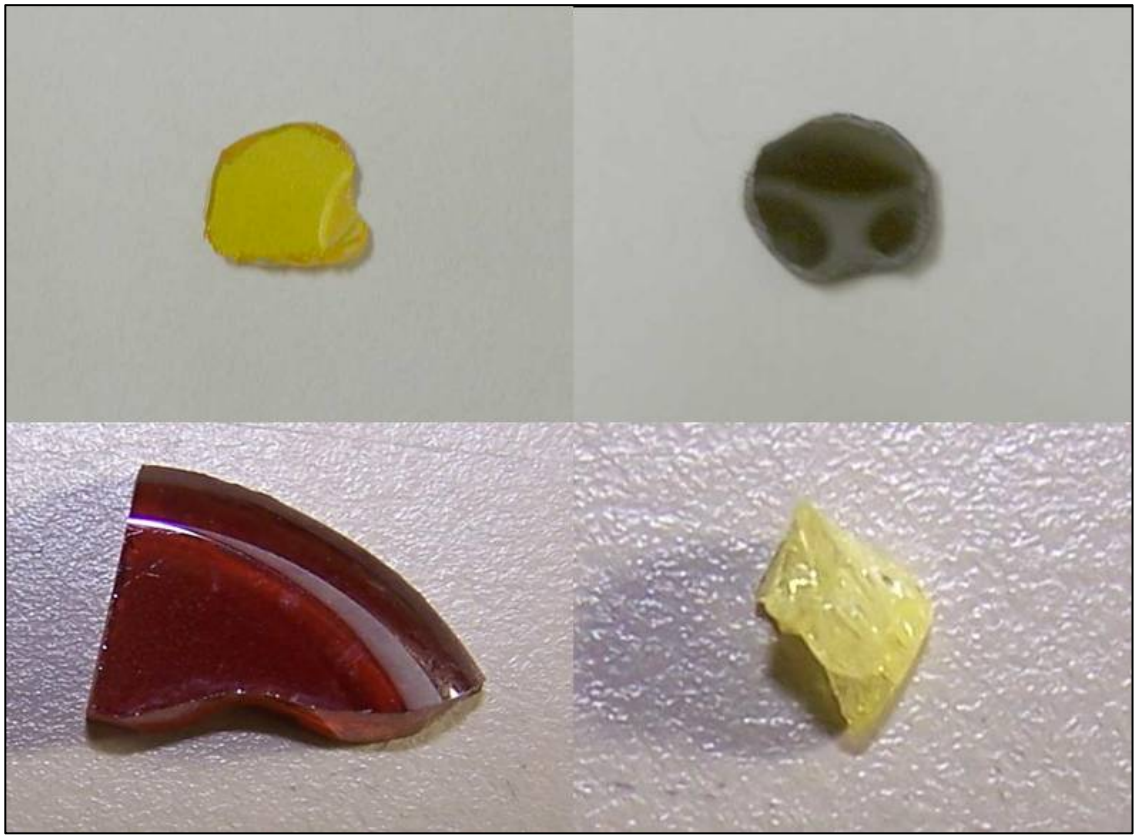

Figure 1.5: Some bulk chalcogenide glass samples. Top left: GeGaS, Top right: GeGaSe, Bottom left: GaLaS and Bottom right: GeGaS:CsBr.

1.2.2 Heavy-metal Glasses

Heavy-metal glasses such as ZBLAN have caught the attention of various researchers in the field of optics. The ZBLAN group, as originally developed, contains fluorides of zirconium, barium, lanthanum, aluminum and sodium. One of the exceptional properties of these glasses is their high transparency range, extending from the UV well into the mid-IR range [8]. They also possess a higher refractive index than most commercial glasses but lower than chalcogenide glasses, low material dispersion, low linear scattering and good chemical durability. Due to these properties, ZBLAN glasses are regarded as promising candidates for a wide range of applications such as laser windows, IR domes, infrared sensing, and infrared fiber optics [9].

It was found that the simultaneous addition of small amounts of the fluorides of lanthanum and aluminum increases the stability of these glasses [10]. As a result, fiber fabrication of these glasses was well under way, but due to the complexity in drawing long lengths of low-loss fibers, interest in using ZBLAN for telecommunications fiber faded. However, there has been a growing interest to use these glasses to make fiber lasers and amplifiers. ZBLAN glasses possess low phonon energies [11]. Consequently, when rare earth ions are embedded in these glasses they exhibit the greatest number of useful radiative transitions, which makes them excellent hosts for the realization of optical amplifiers. Figure 1.6 shows a bulk sample of fluorochlorozirconate (FCZ) glass, a member of the ZBLAN family.

Figure 1.6: Bulk sample of FCZ.

1.2.3 Phonon Energies in Glasses

Phonons are basically lattice vibrations. The weight of the constituent atoms of a glass and the strength and nature (ionic or covalent) of its bonds determine the characteristic phonon energies of the glass. The efficiency of a desired radiative transition depends strongly on the phonon energy. This is due to the fact that the rate of multi-phonon decay between two energy levels is exponentially dependant on the number of phonons required to bridge the energy gap. For optical amplification, depending on the amplification wavelength, it's good to have glass hosts with low phonon energies. For example, the transition of rare earth ions in the mid to far-infrared range can demonstrate high quantum efficiency in low phonon hosts such as chalcogenide and heavy metal glasses. On the other hand, if the same ions are embedded in high phonon energy hosts such as silicate or phosphate glasses, these transitions will be quenched by non-radiative

processes at room temperature [3]. Table 1-1 shows the phonon energies for different glass hosts.

Table 1-1: Phonon energies for different host glasses [3].

Glass Host	Phonon Energy (cm^{-1})
Chalcogenide (selenide)	350
Chalcogenide (sulfide)	450
Heavy-metal fluoride	500
Tellurite	700
Germanate	900
Silicate	1100
Phosphate	1200
Borate	1400

1.3 Research Objective

The optical properties of the rare earth ion-host combinations help determine the characteristics of luminescent devices. In particular, cross-sections and lifetimes are needed. Knowing the relevant information can lead to the accurate prediction of the performance of an amplifier. Optical spectroscopy is considered to be one of the most powerful tools to obtain the necessary information. The basis of optical spectroscopy is the absorption and emission processes. Therefore, in our research, we have focused on these processes to better understand our RE doped glass samples for use in optical amplification.

The main objectives of this project are to measure cross-sections and lifetimes and the steps involved are as follows,

- Cut and Polish bulk glass samples
- Measure transmission spectra and use it to obtain the absorption coefficient for the various absorption bands of the rare earth ion embedded in the matrix
- Use absorption coefficient and calculate the photoluminescence properties, i.e. Judd-Ofelt parameters, Judd-Ofelt lifetime and branching ratio for the bands of interest
- Measure decay time and compare it with the calculated Judd-Ofelt lifetime
- Measure emission spectra for wavelengths of interest and compare the shape with that of the spectra obtained via McCumber theory

Certain conclusions will then be made based on the above outcomes.

1.4 Thesis Outline

This thesis is divided into a total of six chapters. Following this introductory chapter, a brief overview of the amplification concepts and the operation of an erbium doped optical amplifier will be given in Chapter 2. A detailed explanation of the optical properties of rare earth ions in glasses can be found in Chapter 3. Chapter 4 will describe in detail the experimental setup and procedure followed to obtain the necessary results. The results obtained and the discussions of the outcomes are explained in detail in Chapter 5. Finally, Chapter 6 provides the conclusions of this work.

2. AMPLIFICATION CONCEPTS AND THE ERBIUM DOPED FIBER AMPLIFIER

2.1 Introduction

Before we try to understand the optical properties of rare earth doped glasses, it is essential to understand the background reason that calls for such a request. Optical amplification is an integral part of any optical network, whether it is long haul telecommunications or integrated optics. Just the way electrical amplifiers are used in the world of electronics; optical amplifiers are called for in the world of photonics. In this chapter, we discuss some of the background concepts that explain how optical amplification is achieved, as well the working of an optical amplifier, namely the Erbium Doped Fiber Amplifier (EDFA).

2.2 Luminescence

Luminescent materials are all around us, fluorescent lighting, television, computer screen, X-ray photography in hospitals, etc. Luminescent materials, called phosphors, can convert certain types of energies into electromagnetic radiation over and above thermal radiation [12]. The electromagnetic radiation emitted by luminescent materials may belong to the ultraviolet, visible or infrared regions of the electromagnetic spectrum. Very often, the emitted light is from impurities, defects or certain dopants, called luminescence centers or activators that are introduced into the host matrix such as glass.

There are various types of luminescence, i.e., luminescence can be achieved through excitation by different types of energy. Photoluminescence (PL) uses electromagnetic radiation for excitation to achieve luminescence, electroluminescence uses electric

voltage, triboluminecence uses mechanical energy, cathodoluminescence uses a beam of energetic electrons, chemi-luminescence uses chemical reaction as its excitation energy and X-ray luminescence uses X-rays and so on. Figure 2.1 shows the possible outcomes of exciting an ion in a host matrix.

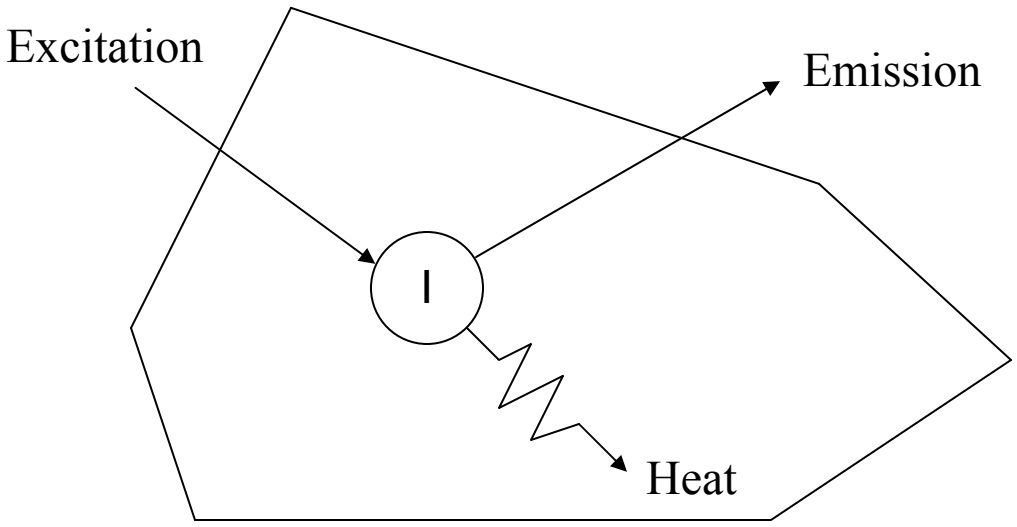

Figure 2.1: An ion, I, sitting in a host lattice (e.g. Glass). Excitation energy can cause either emission (radiative return to ground state) or heat (non-radiative return to the ground state [12].

2.2.1 Photoluminescence

Of the various luminescences explained above, in our research we have focused on photoluminescence. Photoluminescence is the process of exciting an active ion with electromagnetic energy (photon) and thereby obtaining luminescence. Figure 2.2 shows an energy level scheme of how photoluminescence is achieved. Basically, an incoming photon excites the ion from its ground state to a higher energy level. The excited ion then can either return to the ground state radiatively or non-radiatively. The radiative return

produces a photon and the non-radiative return produces a phonon (heat or lattice vibration). The process of exciting the ion directly is called activator excitation. However, it should be mentioned that the incoming photon doesn't necessarily have to excite the ion in the host matrix. Depending on its energy it could quite possibly excite the host matrix itself, which in turn transfers energy to the ion and thereby exciting it to a higher energy state.

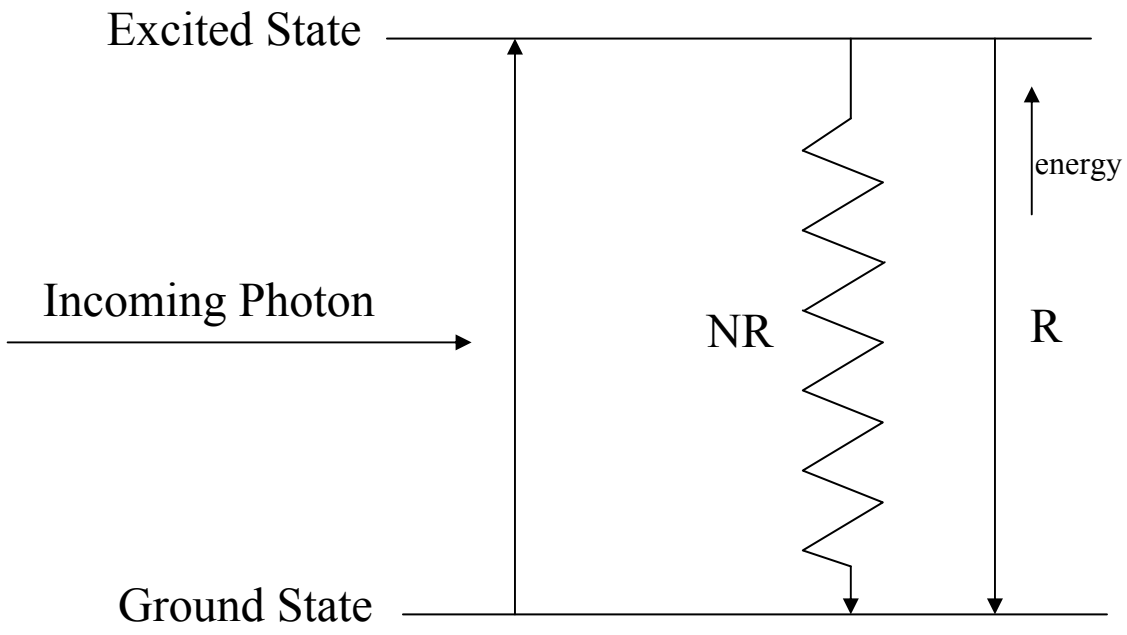

Figure 2.2: Energy level explanation of photoluminescence. R represents radiative return of the ion to the ground level and NR represents the non-radiative return of the ion to the ground level [12].

2.3 Absorption and Emission Processes

Photon amplification requires a good understanding of the absorption and emission processes. An electron in an atom at energy level E_1 can be excited to a higher energy level E_2 by absorbing a photon of energy $h\upsilon = E_2 - E_1$, where h is Planck's constant and υ is the photon frequency. The absorption process is shown in Figure 2.3. When an electron moves from a higher energy level to a lower energy level it can emit a photon. The electron can either spontaneously transit down to a lower energy level or can be provoked to do so by a photon. Hence the emission process has two possibilities.

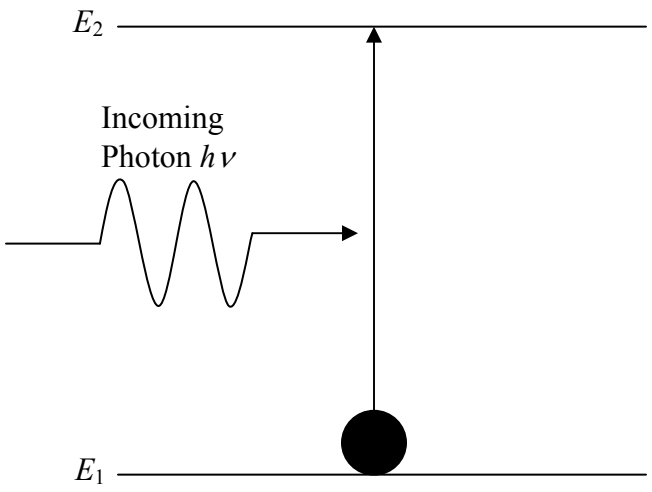

Figure 2.3: Absorption [13].

Spontaneous emission is the process whereby an electron from energy level E_2 transits down to energy level E_1 and emits a photon of energy $h\upsilon = E_2 - E_1$ in a random direction. For this to occur there shouldn't be any electrons in energy level E_1 as revealed in Figure 2.4. In classical physics, an electromagnetic radiation of frequency υ is released when a charge in an oscillatory motion accelerates and decelerates with a frequency υ. The

transition of the electron from E_2 to E_1, which leads to the emission process, can be seen as the electron oscillating with a frequency υ [13].

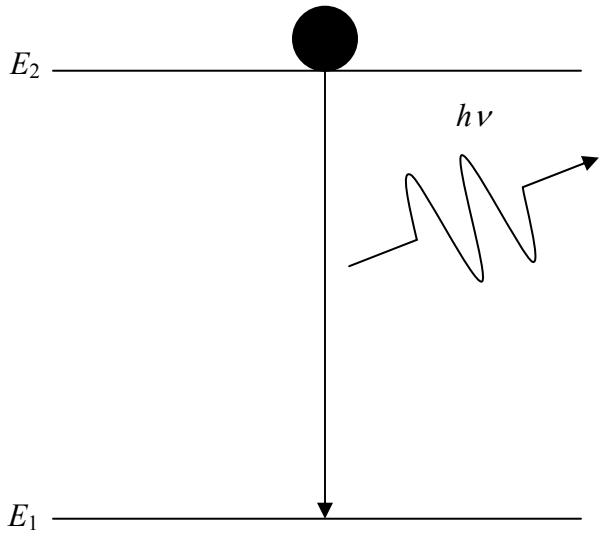

Figure 2.4: Spontaneous emission [13].

Stimulated emission is the process whereby an incoming photon of energy $h\nu = E_2 - E_1$ stimulates the entire emission process by provoking the electron to transit down from energy level E_2 to energy level E_1. The emitted photon has the same direction, polarization and energy as the incoming photon and hence in phase with it as shown in Figure 2.5. We can think of this as the electric field of the incoming photon coupling with the electron and thus driving it with the same frequency, $\nu = (E_2 - E_1)/h$ as the photon. As a result, electromagnetic radiation is emitted whose electric field is in phase with that of the inducing photon. Once the incoming photon has left the site, the electron can transit down to energy level E_1 since it has emitted a photon.

The absorption and emission processes explained for transitions of an electron in an atom could very well be applied to the atom itself or an ion. In which case, the energy levels will correspond to that of the atom or ion.

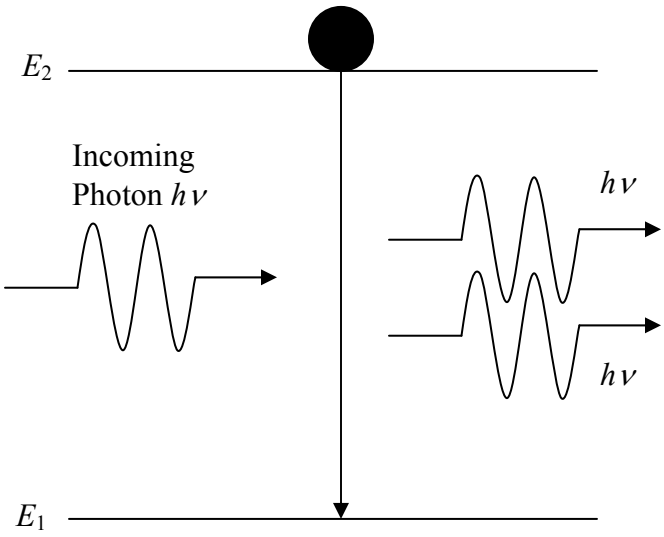

Figure 2.5: Stimulated emission [13].

2.4 Photon Amplification

Photon amplification is based on stimulated emission as there is only one incoming photon and two outgoing photons. In order to achieve photon amplification, the incoming photon should not be absorbed by an ion at energy level E_1. Therefore, when we have a collection of ions, we must ensure that most of these ions sit in energy level E_2. If not, the incoming photon will be absorbed by the atoms in E_1. The state in which there are more ions in energy level E_2 than in E_1 is called population inversion. It is not possible to achieve population inversion in a two level system as there is an equal probability for the incoming photon to get absorbed by an ion in energy level E_1 as for it to stimulate an ion in energy level E_2 to cause emission.

Let us consider a three level system with energy levels E_1, E_2 and E_3. Let us say that an external excitation source is used to excite ions from energy level E_1 to E_3. Energy level E_3 can be termed as the pump energy level and the process of moving ions from the ground energy level to the pump energy level is called pumping. This is shown in Figure 2.6. There are many pumping mechanisms that can be used, but we will mostly concern ourselves with optical pumping. In other words, we will use light as our pumping source to move ions to E_3.

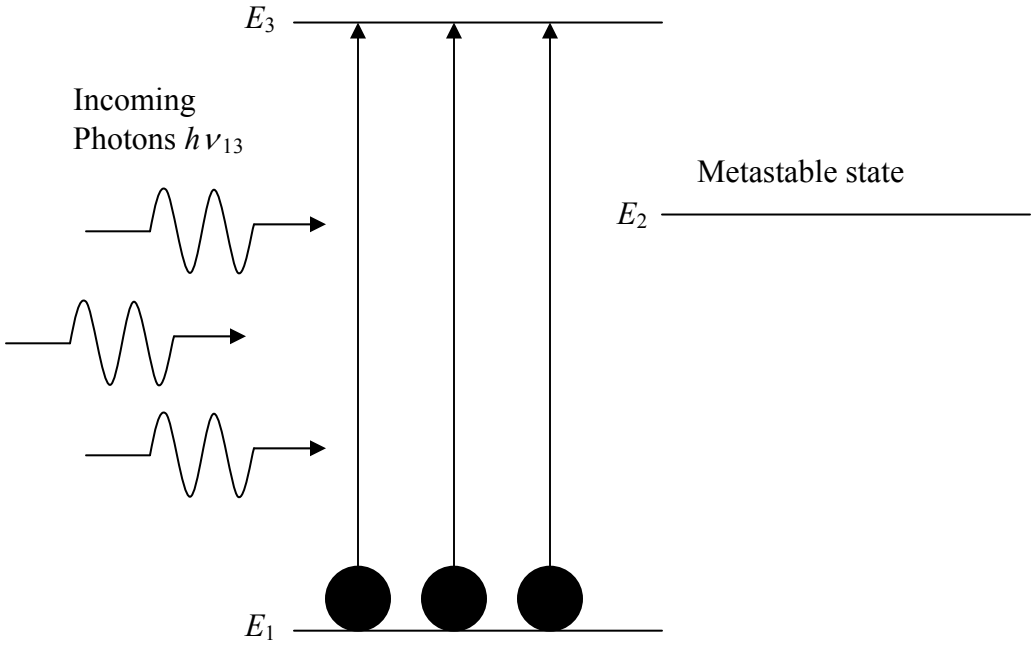

Figure 2.6: Incoming photons of energy $h\upsilon_{13}$ pump ions from ground state E_1 to pump energy level E_3 [13].

Ions rapidly decay down from energy level E_3 to energy level E_2 by emitting photons or lattice vibrations (phonons). E_2 happens to be a state that does not allow ions to rapidly and spontaneously decay down to a lower energy level. This state is called a long-lived or a metastable state. As ions cannot decay down rapidly to energy level E_1 they tend to accumulate in this metastable state. This causes a population inversion between E_2 and E_1

as pumping keeps carrying more and more ions to state E_3 and subsequently to E_2. This process is shown in Figure 2.7 and Figure 2.8.

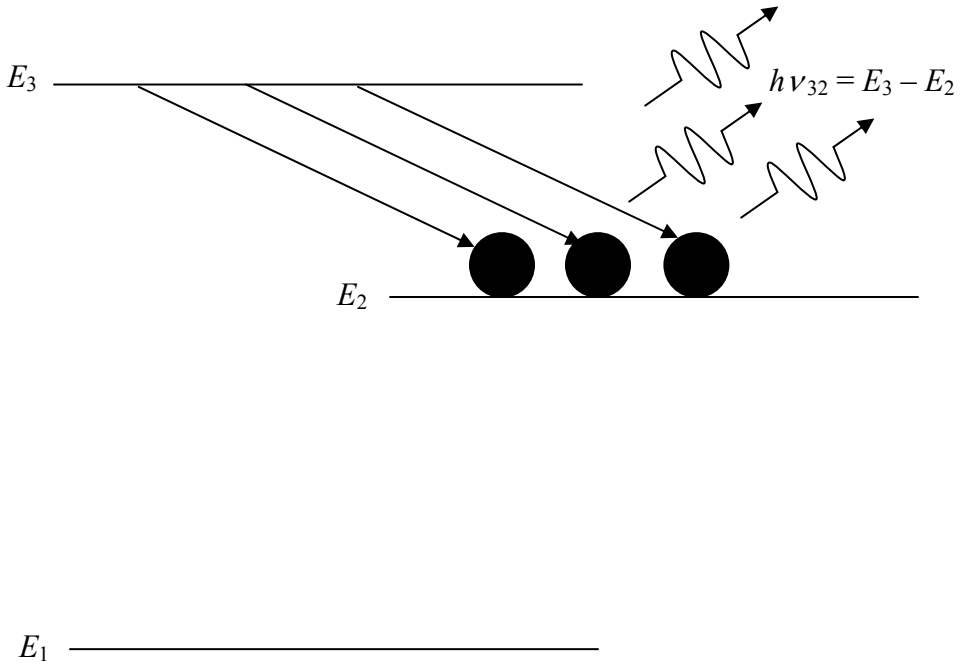

Figure 2.7: Ions rapidly decay from energy level E_3 down to energy level E_2 by emitting photons or phonons of energy $h\upsilon_{32}$ [13].

Now, suppose an incoming photon of energy $h\upsilon_{21} = E_2 - E_1$ stimulates an ion in E_2 to emit a photon that's in phase with it then this emitted photon goes on and causes another ion in E_2 to decay down to E_1 by emitting another photon that's in phase. Thus an avalanche effect is triggered, which leads to photon amplification. This can be seen in Figure 2.9. The photon amplification process explained here is the basis on which an optical amplifier operates.

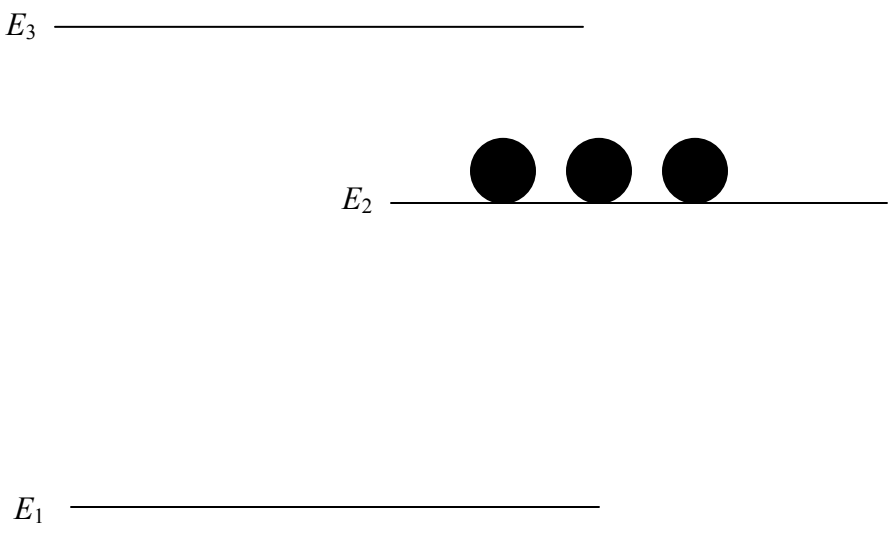

Figure 2.8: As E_2 is a long lived state, ions quickly populate this state and cause population inversion between E_2 and E_1 [13].

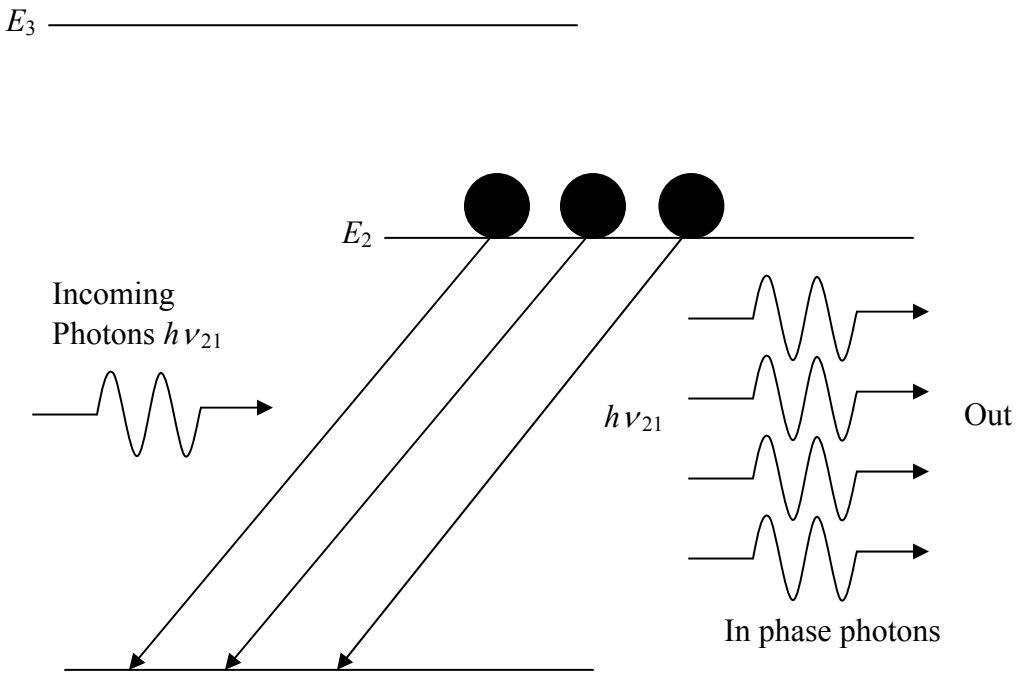

Figure 2.9: Photon Amplification [13].

2.5 Optical Fiber Amplifier

In long haul communications light is used as the medium of transportation. Over distance, the strength of the light signal attenuates. Therefore, it is necessary to regenerate the signal at various points of the telecommunication line. Instead of converting optical energy into electrical energy, amplifying the signal using an electrical amplifier and then converting it back to optical energy by a laser diode, it becomes faster to use an optical amplifier. The most common optical amplifier is the Erbium Doped Fiber Amplifier.

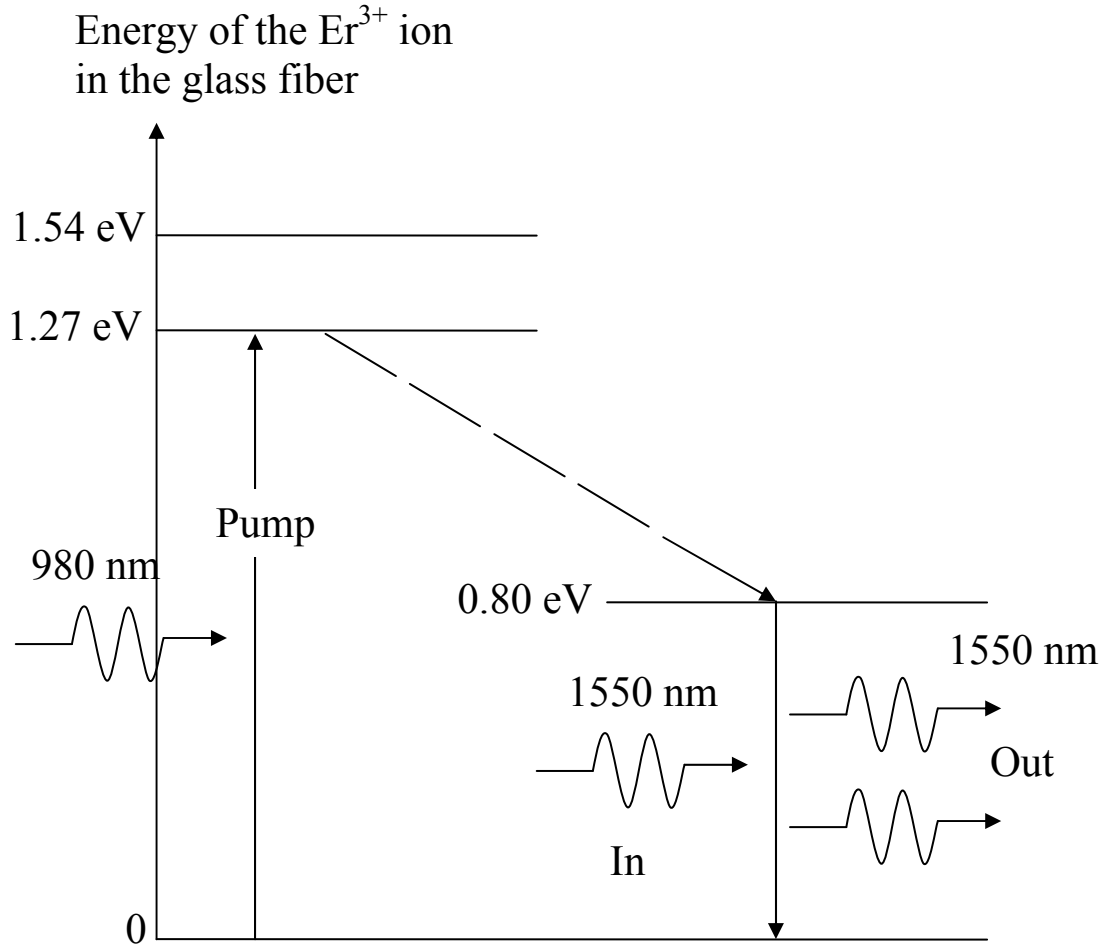

Figure 2.10: Er^{3+} ion energy levels in a glass host and light amplification by stimulated emission. The dashed arrow represents rapid non-radiative decay [13].

The core region of the EDFA is doped with Er^{3+} ions and the host fiber core is a glass that is based on SiO_3-GeO_2 along with some oxides such as Al_2O_3 [13]. The energy levels for Er^{3+} ion when embedded in a glass matrix is shown in Figure 2.10. E_1 represents the ground energy level or the lowest energy possible for the Er^{3+} ion. E_3 and E'_3 energy levels are at 1.27 eV and 1.54 eV, respectively, with respect to the ground energy level. They pose as two well-located levels for optical pumping of the Er^{3+} ions. A laser diode operating at 980 nm is usually used to pump the Er^{3+} ions up to the energy level E_3.

The ions rapidly decay from energy level E_3, non-radiatively, by emitting phonons or lattice vibrations to energy level E_2. This level is a long-lived state whose life time is approximately 10ms, which is quite long on the atomic scale. As a result, more and more Er^{3+} ions accumulate in this level, populating it and thereby causing a population inversion between E_2 and E_1. The most commonly used signal wavelength in telecommunications is 1550 nm, which corresponds to 0.80 eV. This is the same as $E_2 - E_1$. Thus, the incoming telecommunication signal causes stimulated transitions of Er^{3+} ions from E_2 to E_1 to occur. Er^{3+} ions that are left at E_1 can also absorb the incoming 1550 nm photons and transit up to E_2. Therefore, in order to achieve light amplification we need stimulated emission to exceed absorption. This is only possible by obtaining a population inversion between E_2 and E_1.

The optical gain due to stimulated emissions depends on the product of $N\sigma\tau$, where N is the concentration of active rare earth ions, σ is the emission cross section and τ is the lifetime of the lasing level [53]. Therefore, the focus of this research is to evaluate these parameters for the samples under investigation. For more on optical gain, the reader is referred to [14].

Now, let us consider a practical fiber communication line that incorporates an EDFA by splicing as shown in Figure 2.11. Pumping is achieved via a laser diode through a coupling fiber arrangement. As a result, only the pumping wavelength is coupled.

Unwanted noise can be seen in the amplified signal as a result of some of the Er^{3+} ions decaying spontaneously from E_2 to E_1. Moreover, it is very crucial for the EDFA to be pumped at all times. Otherwise, the 1550 nm photons will be absorbed by the Er^{3+} ions, which get excited from E_1 to E_2. Upon returning back to E_1, spontaneously, they will emit photons randomly and not along the axis of the fiber. This causes the EDFA to act as an attenuator rather than as an amplifier.

Figure 2.11 shows a schematic illustration of an EDFA along with a pump laser diode in a telecommunication line. Optical isolators, which are not shown in Figure 2.11, prevent the 980 nm pump light from flowing into the communication line; as well, they allow the 1550 nm optical signal to pass only in one direction. Further, the EDFA output power is monitored by a photodetector that's usually coupled to the line, which is also not shown in Figure 2.11.

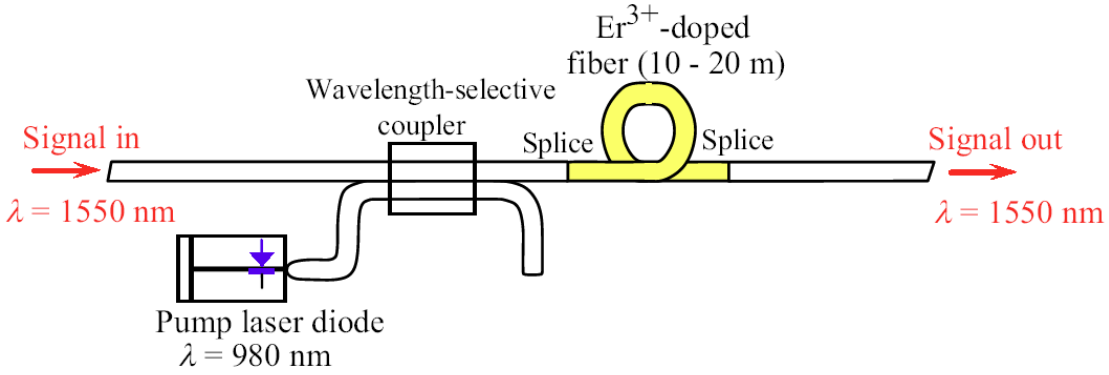

Figure 2.11: Schematic illustration of an EDFA along with a pump laser diode in a fiber communication line. (After [13])

Finally, it is important to mention that the energy levels E_1, E_2 and E_3 are not single levels; rather they are a collection of levels and are called manifolds. As a result, there is a range of stimulated transitions from E_2 to E_1 that lead to a wavelength range of about 1525 – 1565 nm that can be amplified [13]. The maximum gain achieved per unit optical

pumping power is classified as the gain efficiency of an EDFA. It is usually quoted in dB/mW.

3. OPTICAL PROPERTIES OF RARE EARTH IONS IN GLASSES

3.1 Introduction

Optical applications have used rare earths for a very long time. Of the various luminescent devices, the ones using glasses have been in the forefront of optical research for the reasons mentioned previously. Some of the unique properties of rare earths that distinguish them from other optically active ions are as follows,

- the wavelength ranges over which they absorb and emit are quite narrow
- the wavelengths corresponding to the absorption and emission transitions are relatively insensitive to the host material
- the transition intensities are weak
- the meta-stable states have long lifetimes and
- except in aqueous solutions, they tend to have high quantum efficiencies

These properties enable rare earths to perform excellently in many optical applications. Optical amplifiers, as mentioned earlier, provide gain. Therefore, they demand low scattering losses. Hence rare earth doped glasses, as opposed to crystals, are more suitable materials for optical amplification. This chapter outlines some of the optical properties of rare earths in glasses.

3.2 Electronic Structure and Energy Levels of Rare Earth Ions

Two groups of 14 elements each constitute the rare earths. These two groups are termed lanthanides and actinides. The lanthanides start with cerium (Ce), which has an atomic

number (Z) of 58 and end with lutetium (Lu) that has an atomic number of 71. These elements are characterized by the incomplete filling of the 4*f* shell. The actinides on the other hand are characterized by the filling of the 5*f* shell and lie one level below the lanthanides in the periodic table. This group starts with thorium, which has an atomic number of 90, and ends with lawrencium that has an atomic number of 103. Of the two groups, the lanthanides are given greater importance to be used in optical devices, such as amplifiers and lasers. This is because, unlike the actinides, they possess stable isotopes except for promethium (Pm) [15]. The name rare earth is actually misleading. In fact, except for promethium, most of the lanthanides are not so rare and the ones with even atomic numbers are in abundance. Figure 3.1 shows the location of the lanthanides in the periodic table.

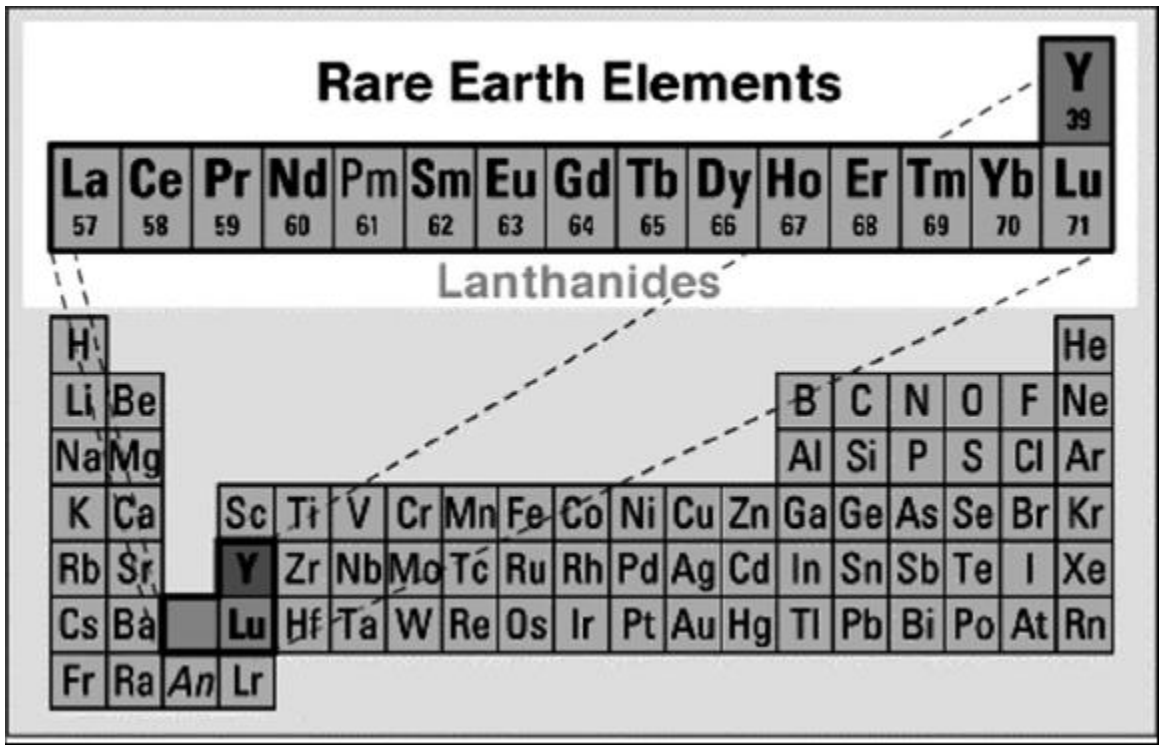

Figure 3.1: Position of the lanthanide series in the periodic table. (After [16])

An atom consists of a nucleus that is surrounded by shells (*K*, *L*, *M*, *N*) and subshells (*s*, *p*, *d*, *f*) that are filled gradually with electrons as we move along the periodic table. The maximum possible number of electrons that can be added to the shells and subshells of an atom are fixed and are shown in Table 3-1. The ordering of the shells and subshells and the rules followed for the insertion of electrons into the shells are explained elsewhere [17] and are not covered here.

Table 3-1: Maximum possible number of electrons in the shells and subshells of an atom. (After [18])

		Subshell			
		$\ell = 0$	1	2	3
n	Shell	s	p	d	f
1	K	2			
2	L	2	6		
3	M	2	6	10	
4	N	2	6	10	14

The optical properties of rare earths are based on their unique atomic structure. Usually, the radius of each successive subshell increases as we go through the periodic table. However, in the case of rare earths the subshells start to contract. When the 5*s* and 5*p* subshells are filled, the next subshell that gets added is the 4*f* subshell and electrons get inserted into this subshell. The radius of the 4*f* subshell, past $Z = 57$, starts decreasing instead of the usual increase that we see for other elements. The theoretical explanation for this, based on the atomic structure of the lanthanides, was given by M. Mayer in 1941 [19]. The average radius of the 4*f* subshell decreases as we move along the lanthanide series [20]. This is called lanthanide contraction and it's about 10% as we progress through the lanthanide series from start to finish. It is this shielding of the 4*f* electrons by the 5*s* and 5*p* subshells that brings about the rich optical transitions in rare earths.

Table 3-2: Occupation of outer electronic shells for rare earth elements. (After [21])

57	**La**	$4s^2$	$4p^2$	$4d^{10}$	**-**	$5s^2$	$5p^6$	**$5d^1$**	$6s^2$
58	**Ce**	$4s^2$	$4p^2$	$4d^{10}$	**$4f^1$**	$5s^2$	$5p^6$	**$5d^1$**	$6s^2$
59	**Pr**	$4s^2$	$4p^2$	$4d^{10}$	**$4f^3$**	$5s^2$	$5p^6$	**-**	$6s^2$
60	**Nd**	$4s^2$	$4p^2$	$4d^{10}$	**$4f^4$**	$5s^2$	$5p^6$	**-**	$6s^2$
…									
68	**Er**	$4s^2$	$4p^2$	$4d^{10}$	**$4f^{12}$**	$5s^2$	$5p^6$	**-**	$6s^2$
…									
70	**Yb**	$4s^2$	$4p^2$	$4d^{10}$	**$4f^{14}$**	$5s^2$	$5p^6$	**-**	$6s^2$
71	**Lu**	$4s^2$	$4p^2$	$4d^{10}$	**$4f^{14}$**	$5s^2$	$5p^6$	**$5d^1$**	$6s^2$

Rare earths are most common in their ionic form, in particular the trivalent form $(Ln)^{3+}$. The atomic form of neutral lanthanide elements is $(Xe)4f^N6s^2$ or $(Xe)4f^{N-1}5d6s^2$, where (Xe) represents Xenon core. $4f^N$ pertains to the ground electronic configuration and $4f^{N-1}5d$ corresponds to the first excited configuration. In the trivalent form, rare earths loose two 6*s* electrons and one 4*f* or 5*d* electron. It is also important to mention that most rare earths can also be stabilized in their divalent forms in appropriate hosts. However, in this research, we have concentrated only on trivalent ions.

Crystal field theory combined with the powerful techniques of tensor calculus had set the stage for detailed investigation of rare earth spectra in the nineteen fifties. In the early sixties, a complete set of energy level assignments for all the trivalent rare earth ions in anhydrous trichlorides was generated by the John Hopkins group under the direction of Dieke [22]. The approximate energy extent of the two lowest, 4*f* and 5*d*, configurations for the tripositive rare earths are shown in Figure 3.2 [22] and the energy levels of the low-lying $4f^N$ states of the trivalent rare earth ions in $LaCl_3$ are shown in Figure 3.3 [23], where the semi-circles represent fluorescing levels. These energy level assignments formed the basis for the exuberant work on rare earths over the last four or five decades.

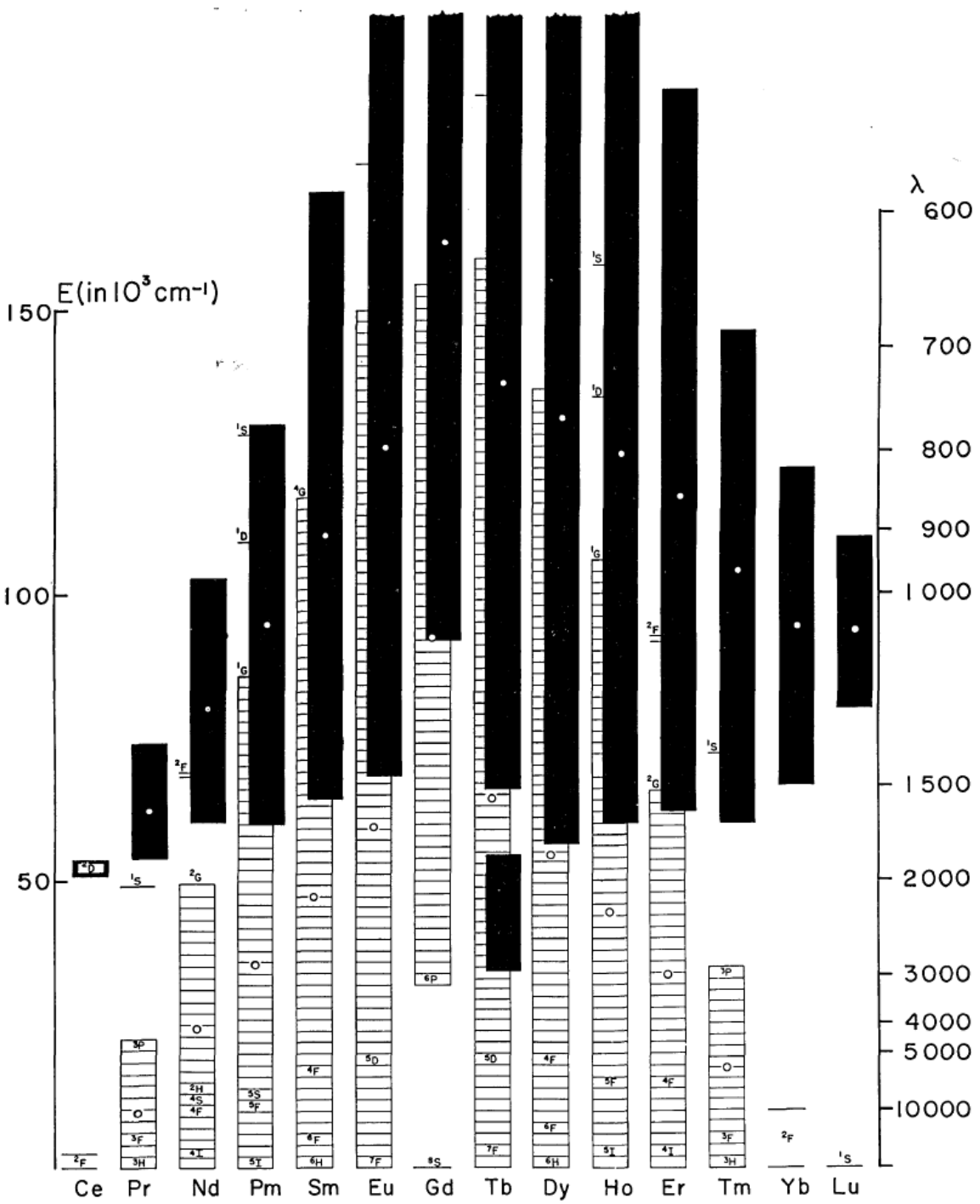

Figure 3.2: Approximate extent of the two lowest configurations of the trivalent rare earths. White represents the $4f^N$ configuration and Black represents the $4f^{N-1}5d$ configuration. (After [22])

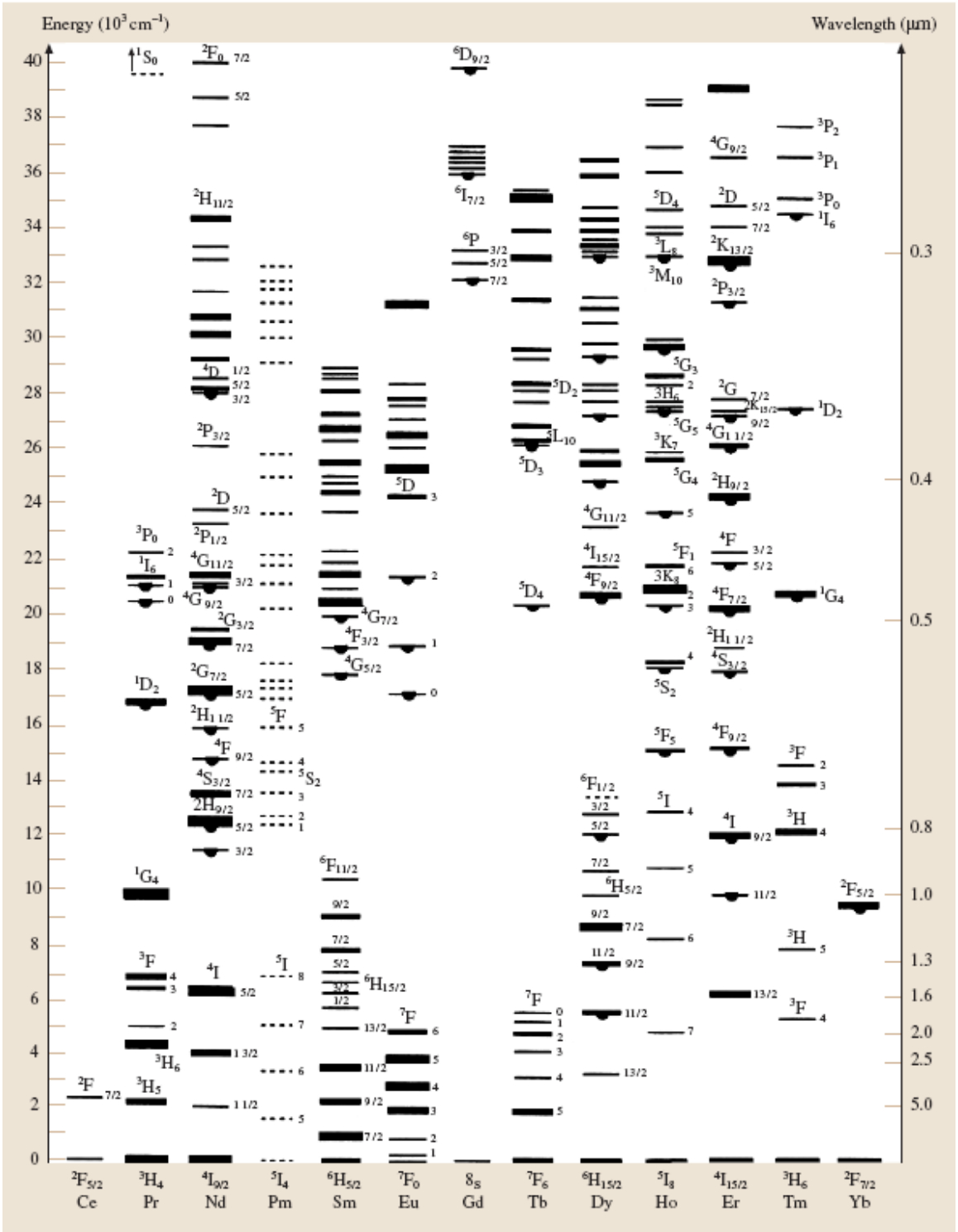

Figure 3.3: Energy levels of the $4f^N$ states of the trivalent ions in $LaCl_3$. (After [23])

The transitions between the energy levels of the $4f^N$ configuration give rise to the optical line spectra of rare earths. The Coulomb interaction amongst the electrons, the spin-orbit coupling and the crystalline electric field yield the positions of these levels. The Coulomb interaction and the spin orbit coupling exist naturally in a free ion (or atom). However, the crystal field interaction or the Stark effect occurs only when the ion is surrounded by an external electric field that originates in a crystalline or glass host.

The splitting of the $4f^N$ configuration is shown schematically in Figure 3.4. The terms ^{2S+1}L are yielded due to the electrostatic interaction with separations of the order of 10^4 cm^{-1}. These terms are then split by the spin-orbit interaction into J states with splittings of the order of 10^3 cm^{-1}. Finally, the crystalline Stark field removes the J degeneracy partially or fully giving rise to a Stark manifold, which usually extends over several hundred cm^{-1}.

Since the centers of gravity of the J states don't show much variation with hosts, Figure 3.3 can be used as a good guide to the location of the J states of the trivalent rare earth ions. However, there is a considerable variation with the order and separation of the levels within a J manifold from one host to another. It is also worth mentioning that the overall Stark splitting is small on the energy scale in Figure 3.3. The thicknesses of the levels show the depth of Stark splitting.

Now, let us consider the naming of the energy levels. The vector sum of the overall angular momenta $L = \sum l_i$ and overall spin $S = \sum s_i$ gives the total angular momentum J in a multi-electron atom, where L is an integer and S is an integer or half-integer. By referring to the collection of quantum states giving J, L, S as a term, one could obtain a set of values for J, L and S. The number of these states is the term's multiplicity, which is equal to $2J+1$ and the number of spin configurations is $2S+1$, which is referred to as the spin multiplicity. This summation rule for angular momenta is called the Russell-Saunders coupling or the L-S coupling. As per convention, the symbol used to denote the

possible states in a multi-electron atom is, $^{2S+1}L_J$, where L = 0, 1, 2, 3, 4… relates to the letters S, P, D, F, G… respectively. For example, the ground state of Er^{3+} has the notation $^4I_{15/2}$ from which one could then obtain the (J, L, S) term as (15/2, 6, 3/2). The term's multiplicity for this sate is $2J + 1 = 16$ and the spin multiplicity is $2S + 1 = 4$.

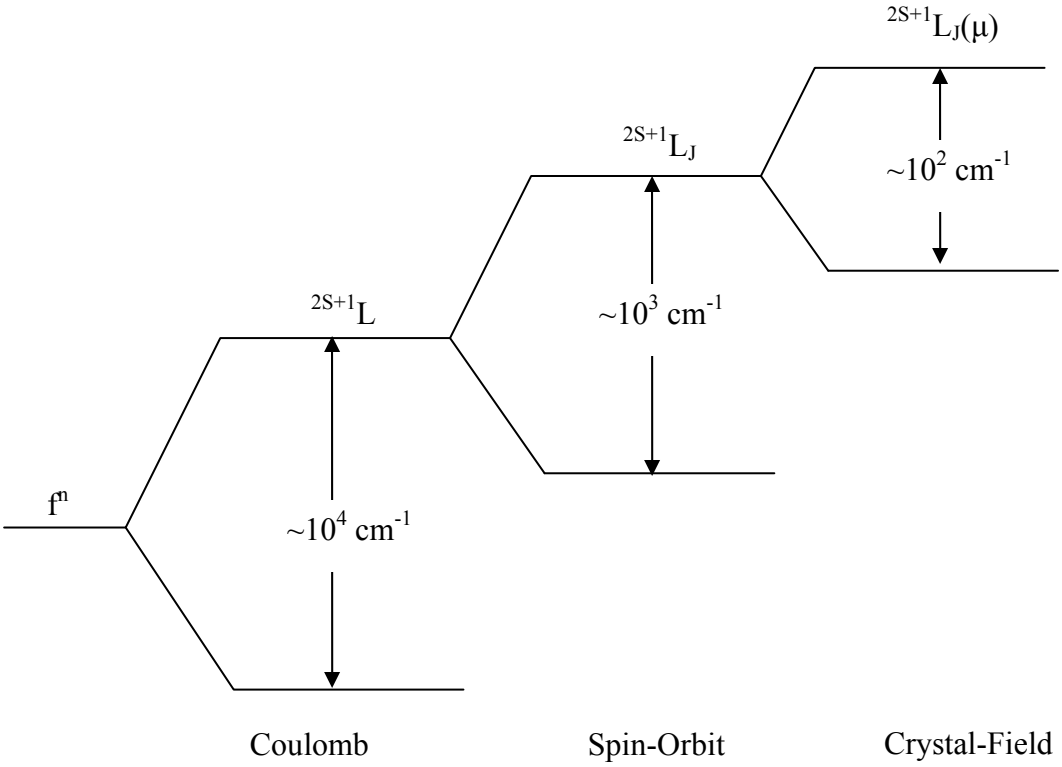

Figure 3.4: Schematic illustration of the splitting of energy levels in rare earth ions due to Coulomb, spin-orbit and crystal-field interactions. (After [24])

3.3 Excitation and Decay in Rare Earths

The two most basic decay processes in rare earths are radiative and non-radiative decay. Transitions between the J levels of different terms give rise to the optical region of the spectrum. Due to the crystalline Stark splitting, transitions between the radiatively

coupled levels in crystals may exhibit hundreds of sharp spectral lines. However, in glasses, the spectral lines are broadened and overlap forming continuous bands. The inhomogeneous broadening is due to the variations in the local crystal field. The presence or absence of emission lines and their intensities may be of great help in relaxation studies.

The separations within a given *J* manifold are within the range of phonon energies. So, the relaxation between levels in a given *J* manifold is rapid. The thermal equilibration among Stark levels is fast. Therefore, in most cases, the *J* manifold can be treated as one level when considering the slower radiative and non-radiative decay rates to other *J* manifolds. However, the radiative and non-radiative transition probabilities from individual Stark levels are not equal. So, under certain circumstances, it is imperative to consider Boltzmann population and transition probabilities from individual Stark levels.

A simplified energy level diagram of the radiative and non-radiative decay schemes for a rare earth ion is shown in Figure 3.5. Let us consider a photoluminescence experiment. Optical radiation is absorbed by the ions in the ground state 0, exciting them to one or more of the upper levels, 3, 4, 5. If the upper levels are closely spaced as in our example in Figure 3.5, relaxation occurs mostly by non-radiative decay to level 3 shown by the zigzag line transitions. If the energy gap is large, as is the case from level 3 to terminal levels 2, 1, 0, relaxation is more probable via radiative decay shown by the straight lines. Levels 2, 1 and 0 are closely spaced in this example. As a result, transition from level 2 to levels 1 and 0 will occur mostly through non-radiative decay.

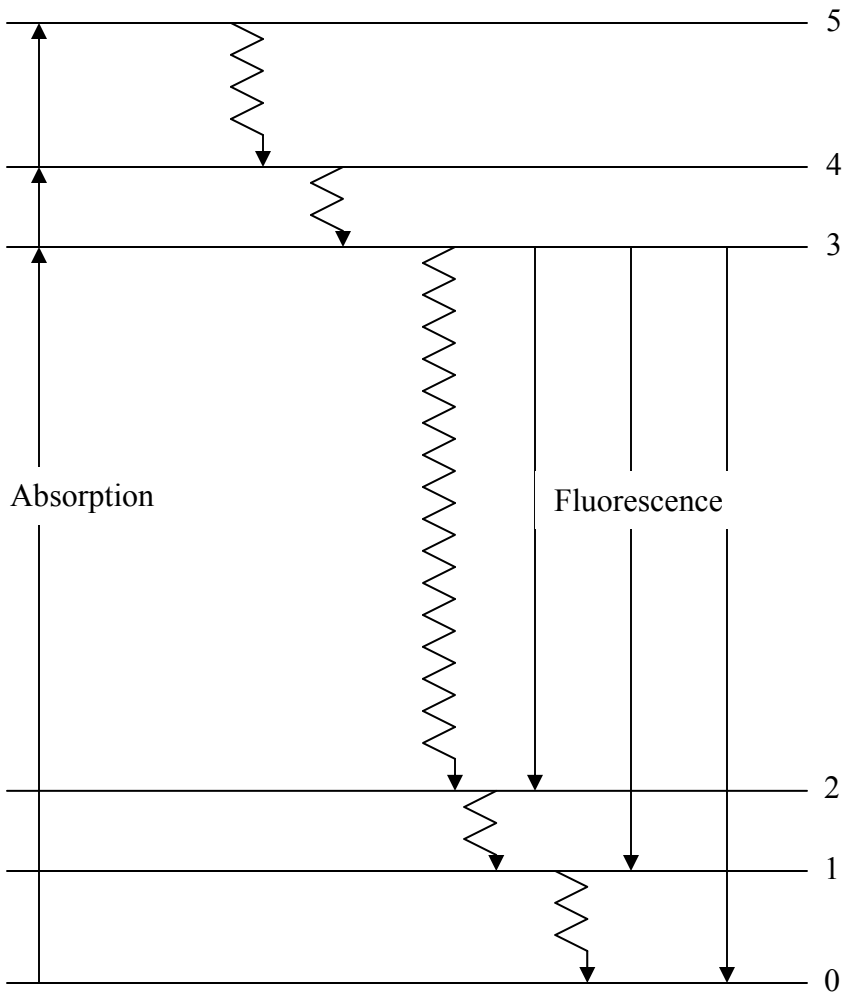

Figure 3.5: Schematic energy level diagram showing the radiative (straight line) and non-radiative (zigzag line) decay schemes for a rare earth ion. After [24]

Combinations of probabilities for radiative and non-radiative processes govern the rate of relaxation of an excited *J* state. For an excited state *a*, the lifetime τ_a is given by

$$\frac{1}{\tau_a} = \sum_b A_{ab}^{\mathrm{R}} + \sum_b A_{ab}^{\mathrm{NR}} \qquad 3.1$$

where the summations are for transitions terminating on all final states, *b*. Both purely electronic and phonon assisted transitions are included in the radiative probability A^{R}. And, relaxation due to multiphonon emission and effective energy transfer arising from ion-ion interactions are included in the non-radiative probability A^{NR}. Based on the host involved and the specific rare earth energy levels, the relative probabilities for radiative or non-radiative decay between given levels may vary quite a bit. They could range any where from comparable values to the two extremes, $A_{ab}^{R} \langle\langle A_{ab}^{NR}$ or $A_{ab}^{R} \rangle\rangle A_{ab}^{NR}$. It is beyond our present capabilities to obtain radiative or non-radiative decay rates through meaningful ab-initio calculations. Therefore, experiment and phenomenological treatment are used to obtain these quantities. As we will see later, measurements of excited state lifetimes, experimentally, is not much of a problem.

3.4 Radiative Relaxation

Radiative relaxation of rare earth ions from excited states gives rise to two important properties that help characterize rare earth doped glasses for use as luminescent devices. These are, excited states lifetimes and rare earth ion cross sections. Relevant theories are brought forth in this section to explain these properties.

3.4.1 Judd-Ofelt Analysis

The probabilities of radiative transitions and appropriate radiative lifetimes of excited states, which are useful for various optical applications, can be calculated from Judd [25] –Ofelt [26] (JO) analysis. Optical transitions between electronic states are electric-dipole, magnetic-dipole and electric-quadrupole in nature. However, electric-dipole transitions are the most predominant and contributions from magnetic-dipole and electric-quadrupole are generally small or negligible [24]. As a result, mostly, only the electri-dipole transitions are considered in the complete analysis.

In Judd-Ofelt theory, the probability of spontaneous emission A corresponding to the initial state SLJ and the final state $S'L'J'$ of an electric-dipole transition of the rare earth ion is given to be,

$$A^{\mathrm{ED}}(SLJ, S'L'J') = \frac{64\pi^4 \bar{\upsilon}^3 e^2}{3(2J+1)hc^3} n\chi_{\mathrm{ED}} S_{\mathrm{ED}}(SLJ, S'L'J') \qquad 3.2$$

where e is the electron charge, S, L and J as mentioned earlier are the spin, angular momentum and total angular momentum, respectively, of the initial state used in Russel-Saunders coupling, $\bar{\upsilon}$ is the average frequency of the transition, n is the refractive index, $\chi_{\mathrm{ED}} = (n^2+2)^2/9$ is a so-called local field correction factor and S_{ED} is the electric-dipole line strength that can be calculated using:

$$S_{\mathrm{ED}}(SLJ, S'L'J') = \sum_{t=2,4,6} \Omega_t \left| < f_\gamma^N S'L'J' \left| U^{(t)} \right| f_\gamma^N SLJ > \right|^2 \qquad 3.3$$

where $\Omega_{t=2,4,6}$ are the coefficients reflecting the influence of host material, and $U^{(t)}$ are reduced tensor operator components that are virtually independent of the host material [27]. These reduced tensor operator components are calculated using the so-called intermediate coupling approximation and can be found in many references [28, 29, 30, 31, 32, 33].

The calculated values of S_{ED} from the theory above are compared with the values derived from experimental data using:

$$S_{\mathrm{EXP}} = \frac{3hcn}{8\pi^3 e^2 < \lambda >} \frac{2J+1}{\chi_{\mathrm{ED}}} \int_{\mathrm{Band}} \frac{\alpha(\lambda)}{\rho} d\lambda \qquad 3.4$$

Where $<\lambda>$ is the mean wavelength of the transition, c is the speed of light, e is the elementary electronic charge, h is Plank's constant, $\alpha(\lambda)$ is absorption coefficient, ρ is rare earth ion density, n is the refractive index and $\chi_{ED} = (n^2+2)^2/9$ is the local field correction factor [27]. Minimizing the discrepancy between experimental and calculated values of line strengths, S_{EXP} and S_{ED}, is the key idea of Judd-Ofelt analysis [27]. This is done by the appropriate choice of coefficients Ω_t that are used to characterize the optical transition and compare different materials.

Although we mentioned that the magnetic-dipole transitions are generally neglected in the complete analysis, they are quite important in certain transitions such as, between $^4I_{15/2}$ and $^4I_{13/2}$ in Er^{3+} ion [34]. It is also worth mentioning that of all the JO parameters Ω_2 is of prime importance. This is because it is the most sensitive to the local structure and material composition and is correlated with the degree of covalence [27]: Ω_2 is very small for ionic materials such as fluorides and quite large for covalent materials such as silicates.

After obtaining the JO parameters (Ω_t coefficients), the probabilities of radiative transitions and appropriate radiative lifetimes ($\tau = 1/A$) of excited states can be found. It is also important to know that the reduced matrix elements $U^{(t)}$ are slightly different for emission and absorption. Therefore, when using absorption spectral data to calculate JO parameters, the absorption values for $U^{(t)}$ should be used and the emission values for $U^{(t)}$ are to be used when calculating the spontaneous emission probability A.

There is another factor that has an important influence on the performance of a device. It is called the branching ratio. Suppose we have three energy levels a, b and c with decreasing energies. The branching ratio, β_{ab} for a transition a to b is defined as the

fraction of all spontaneous decay processes that occur through that channel [15] and is given as,

$$\beta_{a,b} = \frac{A_{a,b}}{\sum_{c} A_{a,c}} \qquad 3.5$$

where a is an excited state and b and c are two final states. The denominator is the summation of the probabilities for transitions terminating on both final states. The branching ratio has a significant effect on the efficiency of an amplifier [15].

3.4.2 McCumber Theory

Cross sections describe the interaction of rare earth ion with light as a function of the wavelength or frequency of the light. In an ideal world, all cross sections pertinent to the operation of a device should be measured directly. However, in the investigation of rare earth transitions, it is possible to measure only the absolute values of one of the cross sections; either the absorption or emission cross section spectra. Usually, it's the absorption cross sections that are measured for bulk samples because they are easy to obtain using commercial spectrophotometers provided the ion concentration is known.

Let us consider the absorption of radiation by impurities in a material system. For example, rare earth ions in a glass host. If N is the number of ions per unit volume, and $\alpha(\nu)$ is the absorption coefficient for ion excitations from a manifold centered around energy E_1 to a manifold centered around energy E_2 then the absorption cross section $\sigma_a(\nu)$ is related to the absorption coefficient $\alpha(\nu)$ in a simple way,

$$\sigma_a(\nu) = \frac{\alpha(\nu)}{N} \qquad 3.6$$

The absorption cross section varies quite a bit from one absorption band to another.

Once the absorption cross section is determined, the emission cross section can be obtained from McCumber's theory. This theory provides a simple expression, which relates the absorption and emission cross sections derived for a two level system through detailed balance and the applications of Einstein's relations as,

$$\sigma_a(\nu) = \sigma_e(\nu)\exp\left(\frac{\varepsilon - h\nu}{kT}\right) \qquad 3.7$$

where, $h\nu$ is the photon energy, k is the Boltzmann's constant, T is the absolute temperature and ε is the net free energy required to excite a single ion from the lower energy level to the higher energy level. The only assumption that the McCumber theory requires is that the time needed to establish thermal equilibrium within each manifold be short in comparison with the lifetime of that manifold.

The absorption and emission spectra are equal only at one frequency $\nu = \varepsilon / h$. At lower frequencies (longer wavelengths) the emission cross section is larger, whereas at higher frequencies (shorter wavelengths) the absorption cross section is larger. The major disadvantage of McCumber theory is that ε can be calculated only if the positions of all the Stark levels are known for both the manifolds. For most of our analysis, we have considered only the shape of the cross section spectrum, which makes the analysis much simpler. In this case an arbitrary scale factor can be used instead of evaluating ε.

3.5 Non-Radiative Relaxation

The decay of a rare earth ion from an excited state without the emission of a photon leads to non-radiative relaxation. If the radiative and non-radiative relaxations of an excited level are comparable then the efficiency of luminescent processes beginning from that level is degraded. The two main mechanisms that lead to non-radiative decay are multiphonon emissions and ion-ion interactions.

3.5.1 Multiphonon Relaxation

The emission of multiple phonons can lead to non-radiative relaxation between the *J* states. This emission is sufficient to conserve the energy of the transition. The interaction of the rare earth ion with the fluctuating crystalline electric field (vibrations of the host lattice) gives rise to these multiphonon emissions [35]. Kiel came up with the initial work of predicting multiphonon emissions in crystals [15]. However, this involved complicated mathematical computations. Riseberg and Moos used Kiel's theory as the basis to come up with a lesser mathematical solution by making some assumptions, which formed the fundamental work in predicting phonon emission rates [36].

Phonon relaxation in glasses might have some physical differences in comparison to phonon relaxation in crystals. Firstly, the structure of glasses is more complicated in contrast with the ordered structure of crystals, which may cause differences in vibrations. Secondly, phonons tend to have higher frequencies in glasses, which lead to faster relaxation. Thirdly, depending on the site occupancy of the rare earth ion in glass, the symmetries and strengths of the ligand field interaction with the rare earth ion may vary. As a result, phonon relaxation in glasses must be non-exponential in nature. However, the predicted exponential dependence of the relaxation rate on energy gap, as seen in crystals, and the measured decay rates in glasses have been shown to be the same [37,

38]. Therefore, the theory of multiphonon emission for crystals may well be applicable for glasses [37, 38].

The multiphonon emission rate W_{MP} is given as [39]

$$W_{MP} = W_0 \prod_i (n_i + 1) p_i \tag{3.8}$$

where p_i is the number of phonons emitted with energy $h\omega_i$, W_0 is the spontaneous emission rate at 0 K and n_i is the Bose-Einstein occupation probability,

$$n_i = \left[\exp\left(\frac{h\omega_i}{kT} \right) - 1 \right] \tag{3.9}$$

From the above expression we see that the multiphonon emission rate is temperature dependent. The minimum number of phonons that are required to bridge two successive energy levels is given as,

$$\sum p_i = \frac{2\pi \Delta E}{h\omega_i} \tag{3.10}$$

where ΔE is the energy difference between the two successive energy levels. Thus, lower phonon energy requires more phonons to bridge the energy gap. The relation between the energy gap and the multiphonon emission rate is given by the following expression,

$$W_{MP} = R^0 \exp(-\delta \Delta E) \tag{3.11}$$

where δ depends on the electron phonon coupling constant and on the phonon energy and R^0 is the phonon transition probability extrapolated to an energy gap of zero [39]. This relation suggests that if the energy gap between successive energy levels is large then higher radiative transition probabilities are possible. In this research, we have not done a detailed analysis of the multiphonon emission processes. However, the above explanation is quite crucial in that it gives a good understanding of the multiphonon emission processes that partly contribute to non-radiative decay.

3.5.2 Ion-Ion Interactions

When the ion (erbium) concentration in a given host is high, undesirable effects occur, which weaken the performance of an amplifier [40]. These effects could be linked to ion-ion interactions. Such effects are predominant in short length fibers or waveguide amplifiers, which are usually only a few centimeters in length. However, such effects could also be found in long length fibers where the ions are confined to the core region, which has a high density of the ions. It is shown that the overall amplifier performance is more efficient for low concentrations of erbium [41]. It is imperative to know the composition of the host glass when analyzing the strength and nature of the interaction effects. These interaction effects become extremely important in the development of waveguide amplifiers for integrated optics.

Energy transfer between rare earth ions is due to ion-ion interaction effects. It is not valid to assume that each ion acts independently of its neighbor once the local concentration of rare earth ions becomes high. At this point, it is imperative to consider the possibility of energy transfer between ions and its consequences [42]. Energy transfer leads to the depletion of the upper state of an amplifying transition, which could potentially have a negative impact on the performance of an amplifier [43]. There are various ion-ion energy transfer mechanisms, which are explained below in detail.

The simplest form of energy transfer is the transfer of energy from an excited ion to a nearby ion in the ground state, without any energy being gained or lost by the two-ion system as a whole. This case of energy transfer may be referred to as resonant energy transfer and is shown in Figure 3.6. Non-resonant energy transfers are also possible. In which case, a photon or a phonon makes up for the difference in energies between the initial and final ionic states.

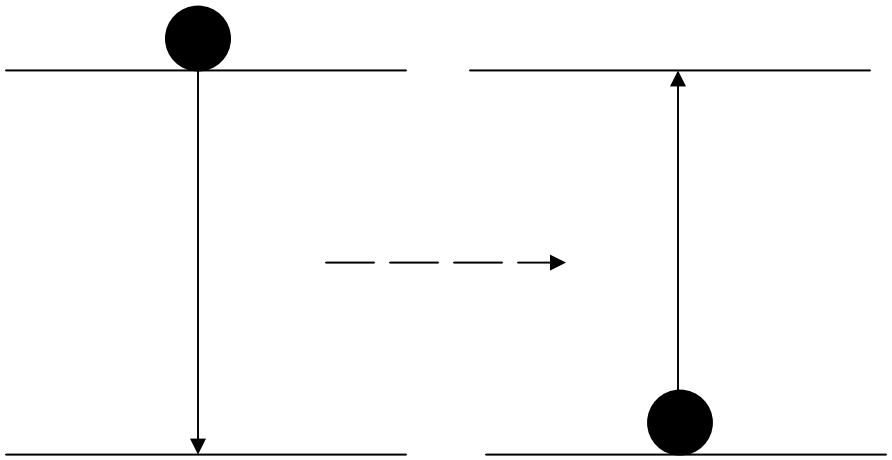

Figure 3.6: Resonant energy transfer. (After [43])

Energy transfer can also be seen between excited state ions. This is shown in Figure 3.7. Here, two ions have been excited previously by some means to a higher energy state. They transfer energy amongst themselves, resulting in the promotion of one of the ions to an even higher energy level. This process is known as up-conversion or stepwise up-conversion. This is the most prevalent up-conversion mechanism in the case of Er^{3+} ions. The excited state is $^4I_{13/2}$, which has a lifetime that is approximately 10ms. This is enough time for closely spaced ions to interact. The decay of one of the ions to ground level gives rise to population depletion in the $^4I_{13/2}$ state, which reduces the overall lifetime of this state. This mechanism has been demonstrated in the works of different authors [44, 45].

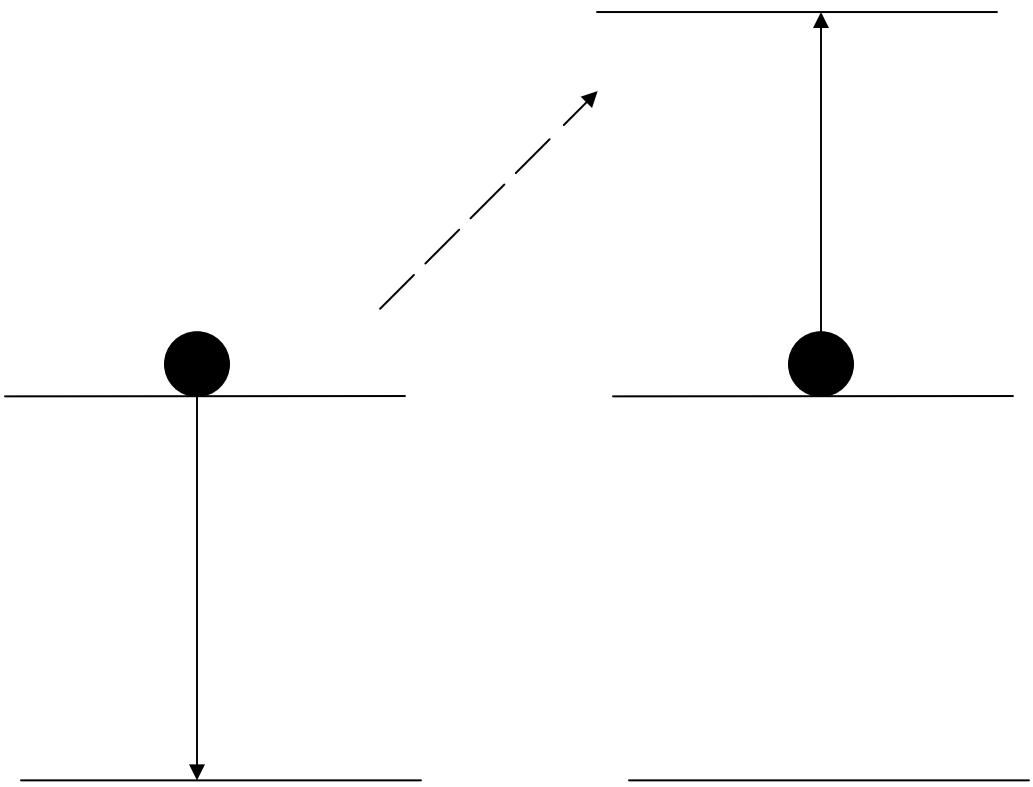

Figure 3.7: Up-Conversion or Stepwise Up-Conversion. (After [43])

Cooperative up-conversion is another process, which involves two or more closely coupled ions. The closeness of these ions makes them act as a single molecule. Cooperative luminescence processes, involving two ions, can be defined as the emission (or absorption) of one photon by the simultaneous involvement of both the ions. As an example, let's consider Figure 3.8. Here, two excited ions in the same excited state decay simultaneously to the ground state. As a result, a single photon with energy twice that of the single-ion excited state is emitted.

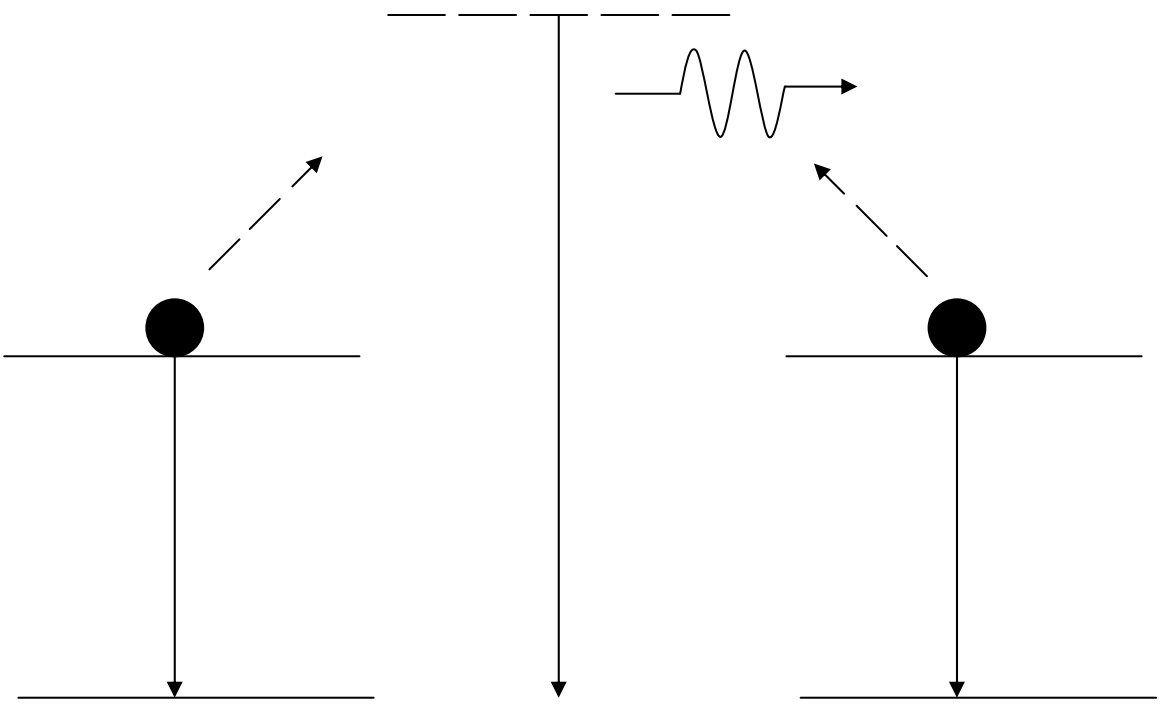

Figure 3.8: Cooperative Luminescence. (After [43])

Figure 3.9 illustrates cooperative energy transfer with simultaneous photon absorption.

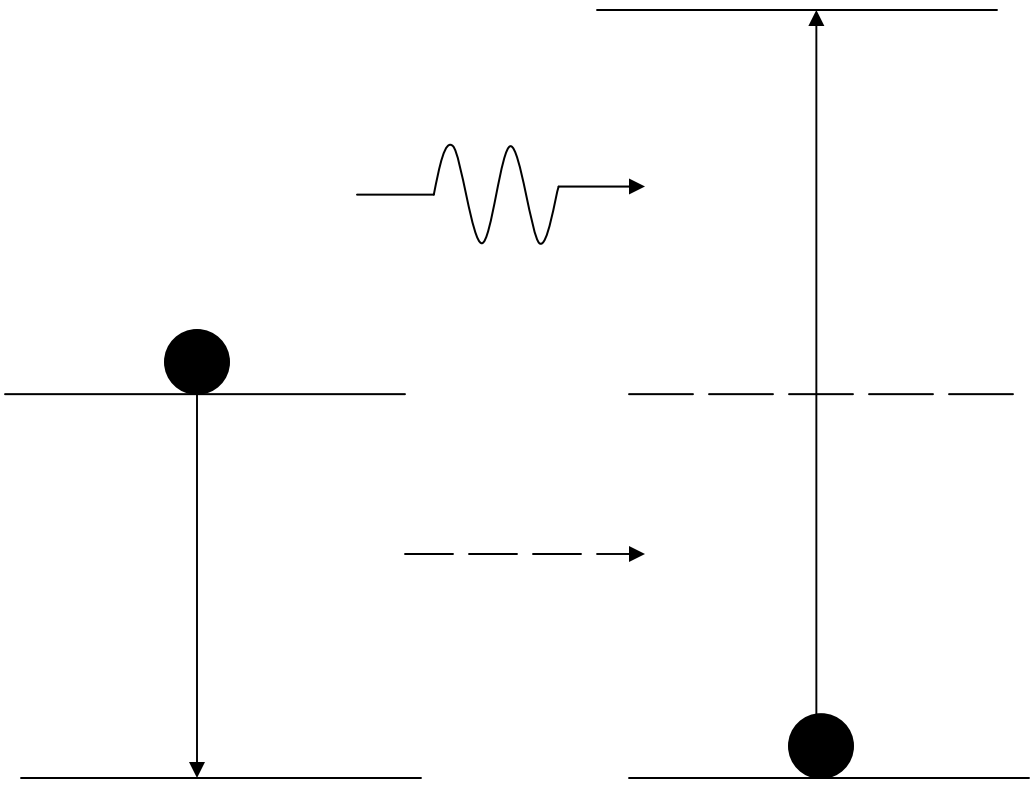

Figure 3.9: Cooperative energy transfer with simultaneous photon absorption. (After [43])

Figure 3.10 explains another energy transfer mechanism termed cross-relaxation. In this process, an excited state ion transfers part of its acquired excitation energy to a neighboring ion. Neodymium energy levels are used as an example to demonstrate the cross-relaxation mechanism. Let's say we excite one of the ions of a pair, by some means, to the meta-stable $^4F_{3/2}$ level. This ion interacts with the near by neighbor (second ion of the pair) in the ground state, thereby transferring part of its energy to this ion. This results in both ions moving to the intermediate $^4I_{15/2}$ state. Due to the fact the energy gaps between the lower lying states are small; both ions rapidly decay down to the ground state non-radiatively. As a result, provided the energy transfer rate is high, the original excitation is converted into heat in a short time when compared to the radiative lifetime.

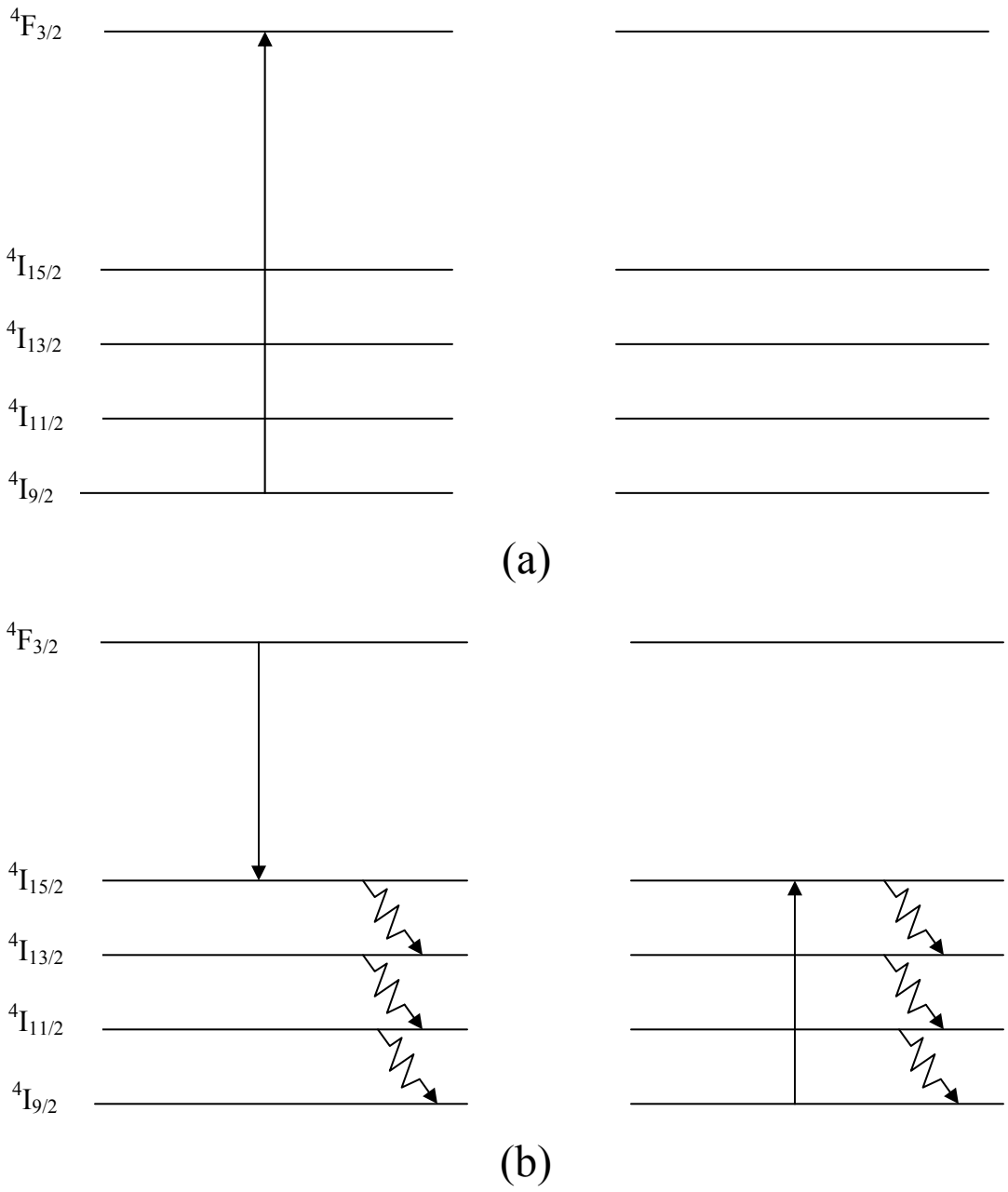

Figure 3.10: Cross-Relaxation process. (a) One of the ions being excited by some means to $^4F_{3/2}$ level. (b) Excited ion transfers energy to neighboring ion in the ground state, exciting it to $^4I_{15/2}$ level. Later, both ions relax to the ground state non-radiatively. (After [15])

4. SAMPLE PREPARATION AND EXPERIMENTAL PROCEDURE

4.1 Introduction

This chapter starts off with the general procedure involved in preparing bulk samples along with the procedure used to cut and polish the samples to arrive at the finished product that can be used to obtain experimental data. It then goes on to explain the methods used to obtain transmission spectra for bulk samples and the operation of the spectrometer. Finally, the procedure involved in obtaining steady state photoluminescence and decay or lifetime photoluminescence data is also explained along with the experimental setup developed to obtain these measurements.

4.2 Bulk Sample Preparation

The samples used in our research were either prepared in our own laboratory or provided to us by our colleagues from other well known laboratories around the world. The general procedure involved in preparing bulk samples is explained here.

Appropriate amounts of the constituent materials are mixed in a silica ampoule. Excess air inside the ampoule is pumped out using a diffusion pump at an ampoule sealing station and the sample inside the ampoule is sealed in vacuum. The vacuum-sealed ampoule is then placed in a rocking furnace, like the one shown in Figure 4.1, where it is heated to the desired temperature for long hours. The melt is subsequently quenched in cold water for glass formation. Once the melt is solidified, the ampoule is wrapped in a protective cloth and cracked open using a hammer. The solidified melt breaks along its

natural stress lines into smaller pieces, which can then be ground and polished for spectroscopic measurements.

Figure 4.1: Rocking Furnace

4.3 Cutting and Polishing Bulk Samples

The bulk samples need to be cut to desired sizes and polished before we could obtain the transmission spectrum. This section explains in detail the procedure involved in cutting and polishing bulk samples.

4.3.1 Cutting

We take a nice big chunk of the solidified melt, after cracking open the ampoule, and run it through a cutter to obtain approximately a $1\text{mm} \times 1\text{mm}$ bulk sample. The cutter used is an IMPTECH EUROPE PRECISION CUTTER, which uses a diamond blade for cutting and is shown in Figure 4.2.

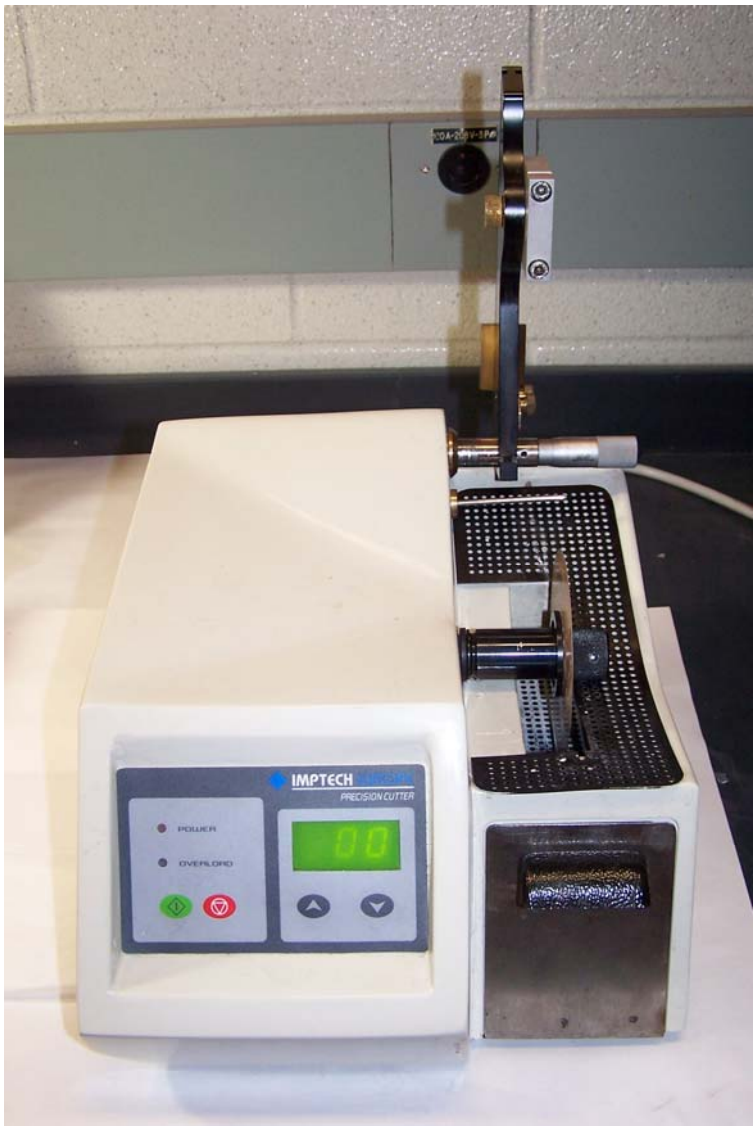

Figure 4.2: IMPTECH EUROPE PRECISION CUTTER.

The procedure involved in cutting a chunk of the solidified glass is as follows,

- The sample is placed in the sample holder that is attached to a screw gage, which is used to adjust the handle so that the sample can be cut at the desired location.
- The handle is then lowered gently, such that the sample touches the diamond saw.
- The spinning speed of the diamond saw is usually kept low. This prevents any cracks from developing during the cutting process, which in turn reduces the risk of sample shattering.
- Some samples can be extremely hygroscopic. Therefore, the lubrication agent used is 100% ethanol.

4.3.2 Grinding and Polishing

After the sample is cut to its desired dimensions, it is then ground and polished. Grinding is done to obtain parallel surfaces on both sides of the sample. The procedure involved in grinding the bulk sample is as follows,

- A glass plate is used for the ground process like the one shown in Figure 4.3.
- We use 600 micron silicon carbide powder for coarse grinding and 1000 micron for fine grinding. The silicon carbide powder is mixed with 100% ethanol on the glass plate.
- The sample is then ground by placing it on top of the mix and slowly making circular motions. This will ensure the sample to have a flat surface on the side it's being ground.
- The sample is now placed on a sample holder. This is done by first placing the sample holder on a Thermolyne HP 2305B heater, which is shown in Figure 4.4. Once the holder is hot enough, a small amount of bee wax is placed on top of it to melt. After which, the sample is placed on the sample holder with the flat surface down. The holder is then partly immersed in a trough that contains water without

the sample coming in contact with the water. This solidifies the bee wax, thereby holding the sample firmly in place.

- The sample is once again ground like before. This ensures that the sample has parallel surfaces on both sides.

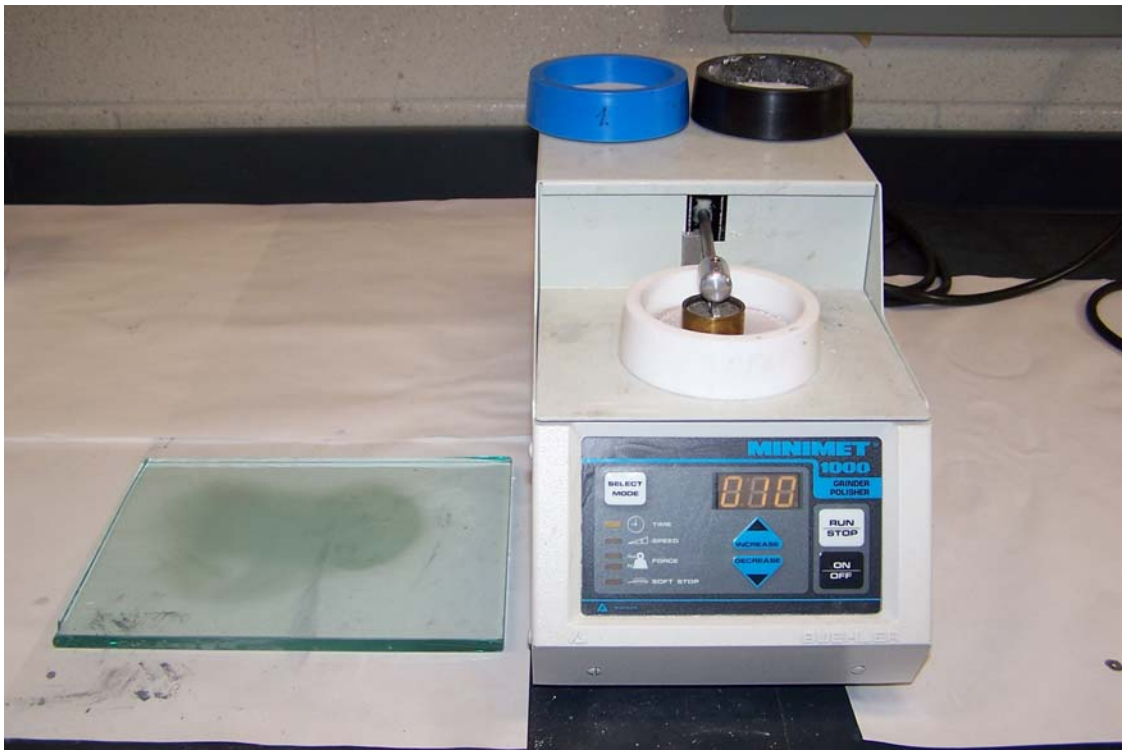

Figure 4.3: Left: Glass plate used for grinding. Right: MINIMET 1000 – Polisher.

Upon the completion of grinding, the next step is to polish both surfaces of the bulk sample. Polishing the sample allows maximum transmission of light through the sample by reducing any scattering at the surface due to imperfections. Polishing is performed using a MINIMET 1000 polisher, which is shown in Figure 4.3.

Figure 4.4: Left to Right: Bee Wax, Thermolyne, HP 2305 B Heater, Sample Holder.

Polishing involves a three stage process, which is as follows,

Stage – 1:

- The blue bowl that can be seen on top of the polishing machine in Figure 4.3 is placed in position, in the slot provided, under the handle of the polisher. Inside the bowl there is a glass plate to which a rough polishing cloth is glued to.
- A few drops of Ehanol+Glykol are added to the surface of the polishing cloth to act as a lubricant.
- The sample holder, with the sample firmly adhered by the bee wax, is then securely held in position by the handle of the polisher.

- The force used by the handle is set to zero along with the soft stop function turned ON.
- With the appropriate time to polish and speed of the handle set, the polisher is started. At the end of this stage, the sample should look a little shiny as opposed to the dull finish that is seen after grinding.

Figure 4.5: Some of the materials used for polishing. Left to Right: 100% Ehanol, Silicon Carbide powder, 3 micron alumina powder, 0.05 micron alumina powder and Ethanol+Glykol mixture.

Stage – 2:

- The black bowl that can be seen on top of the polishing machine in Figure 4.3 is placed in position, in the slot provided, under the handle of the polisher. Inside the bowl there is a glass plate to which a smooth polishing cloth is glued to.
- In order to enhance polishing, 3 micron alumina powder is sprinkled evenly on the surface of the polishing cloth. As well, just as in stage – 1, a few drops of Ehanol+Glykol are added to the surface of the polishing cloth to act as a lubricant.
- The sample holder, with the sample firmly adhered by the bee wax, is then securely held in position by the handle of the polisher.
- Again, just as in stage – 1, the force used by the handle is set to zero along with the soft stop function turned ON.
- The time to polish and the speed of the handle are set. However, both these parameters are higher in comparison to stage – 1. The polisher is then started. At the end of this stage, the sample should have a clear glass like look to it.

Stage – 3:

- The white bowl, which is placed in position as shown in Figure 4.3 is used in this stage. Again, as in stage – 2, a smooth polishing cloth is glued to the surface of the glass plate.
- To further enhance polishing, 0.05 micron alumina powder is sprinkled evenly on the surface of the polishing cloth. Once again, as in the previous two stages, a few drops of Ehanol+Glykol are added to the surface of the polishing cloth to act as a lubricant.
- The sample holder, with the sample firmly adhered by the bee wax, is then securely held in position by the handle of the polisher.

- Again, as in the previous two stages, the force used by the handle is set to zero along with the soft stop function turned ON.
- The time set for polishing is the lowest for this stage and the speed of the handle is the highest. The polisher is now started. Upon completion of this stage, the sample should look very glossy.

After stage – 3, the sample holder is placed on the heater for the bee wax to melt. At which point, the sample if flipped and the entire polishing procedure is repeated for the other side of the sample. After the sample is polished on both sides, diethyl-ether is used to remove bee wax residues off the sample.

4.4 Transmission Spectrum Measurements

The transmission spectrum of bulk samples can be obtained using a spectrometer.

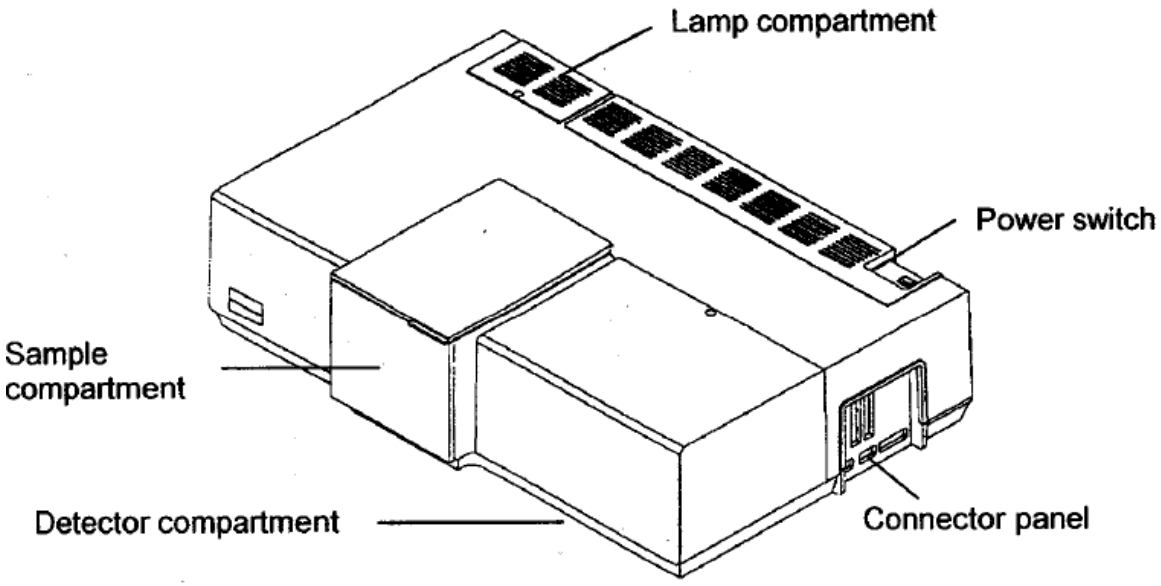

Figure 4.6: Lambda 900 spectrometer's features (from Lambda 800/900's manual).

Figure 4.6 shows the lambda 900 spectrometer that has been used to obtain transmission spectra of the polished bulk samples. It features an all-reflecting, double-monochromator optical system. For durability, the components have been coated with silica. The specifications of the spectrometer are shown in Table 4-1.

A schematic diagram illustrating the operation of the spectrometer is shown in Figure 4.7. The full operating wavelength range of the spectrometer, from 185 nm to 3300 nm, is covered by two radiation sources, the deuterium lamp and the halogen lamp. The visible to near infrared region, i.e. from 300 nm to 3300 nm, is covered by the halogen lamp and the wavelengths from 185 nm to 350 nm are covered by the deuterium lamp. A monochromator passes monochromatic light to the sample and two photodetectors measure the transmittance at different wavelengths.

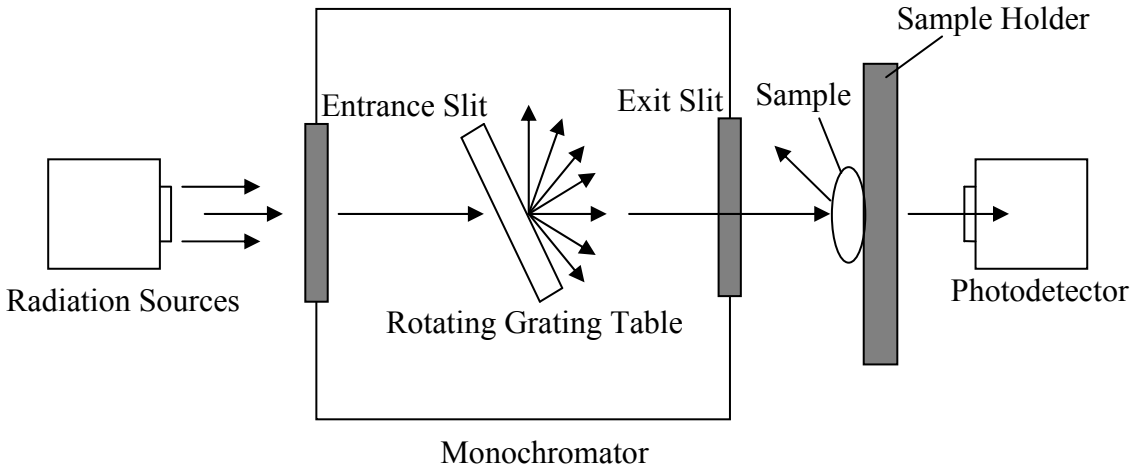

Figure 4.7: Schematic illustration of the operation of a spectrometer.

Table 4-1: Spectrometer's operating specifications (from Lambda 800/900's manual).

Optics

Beam center height	90 mm above baseplate
Beam cross-section	Slit / Width (approx.) / Height (approx.) 0.05 nm 0.04 mm x 11.7 mm 0.1 nm 0.09 mm x 11.7 mm 0.5 nm 0.45 mm x 11.7 mm 1 nm 0.89 mm x 11.7 mm 2 nm 1.00 mm x 11.7 mm 5 nm 4.44 mm x 11.7 mm measured at the focal point of the sample beam and the reference beam in the sample compartment at a wavelength of 500 nm.
Beam separation in sample compartment	126 mm
Optical pathlength in sample compartment	200 mm
Grating (Monochromator)	Holographic gratings with 1440 lines/mm UV/Vis 360 lines/mm NIR
Radiation sources	Pre-aligned deuterium and halogen lamps
Detector	A photomultiplier for the UV/Vis range A Peltier-cooled PbS for the NIR range

Abscissa

Wavelength range	185 to 3300 nm UV/Vis/NIR, 900 nm UV/VIS with N_2 purging down to 175 nm
Wavelength accuracy	±0.8 nm UV/Vis ±0.32 nm NIR

Wavelength reproducibility	<0.02 nm UV/Vis range, <0.08 nm NIR range, (0.008 nm UV/Vis range, standard deviation for 10 measurements) (0.04 nm NIR range, standard deviation for 10 measurements)
Spectral bandwidth	0.05 nm to 5.00 nm in 0.01 nm increments UV/Vis range 0.2 nm to 20 nm in 0.04 nm increments NIR range
Integration time	0.04 s to 10 s in 0.04 s increments

Ordinate

Photometric range	Transmission 0% to 200% (display range) Absorbance –6.000 to 6.000 (display range) 1 to 9999 (concentration units)
Photometric accuracy	Absorbance ±0.003; Transmission ± 0.08% at Absorbance = 1 Absorbance ±0.002; Transmission ±0.05% at Absorbance = 0.5 (measured with NIST (NBS) 930 filters)
Stray radiation	Absorbance > 2 (at 200 nm with Potassium Chloride (KCl) solution) Transmission < 0.00008% (at 220 nm, 340 nm and 370 nm; according to ASTM E-387; 1% attenuator in the reference beam) Transmission < 0.002% (measured at 1690 nm with Chloroform ($CHCl_3$); 4 cm pathlength)
Baseline flatness	Absorbance ±0.001 (corrected; 200 nm to 3000 nm, 4 nm slit, Energy 1 NIR, 2 s integration time)

Noise level	Absorbance < 0.00007 at 1500 nm and absorbance = 0 Absorbance < 0.000050 RMS, at 500 nm; absorbance = 0; 2 s integration time Absorbance < 0.000300 RMS, at 500 nm; absorbance = 2; 2 s integration time Absorbance < 0.000100 RMS, at 190 nm absorbance = 0; 2 s integration time
Absorbance Zero Stability (drift)	Absorbance < 0.0002 per hour (after warm up at 500 nm, absorbance = 0, 2 nm slit, 2 s integration time)

The monochromator uses reflection gratings along with entrance and exit slits to pass monochromatic light to the sample. The light that gets transmitted through the sample is captured by a photomultiplier that operates in the ultraviolet and visible region and a lead sulfide detector that operates in the near infrared region to obtain the transmittance of the monochromatic light through the sample. It should be noted that all transmittance values provided by the spectrometer are in relative terms. That is, it shows the percentage of light, 0% to 100%, that gets transmitted through the sample with respect to another unobstructed and parallel reference beam. It is imperative to point out that apart from deducing the extent of transmission by the host glass, the transmission spectrum is useful in inferring the absorption of light by rare earths, embedded in the bulk sample, at different wavelengths.

Sometimes, we'll need to obtain absorption curves for rare earths at various temperatures. As a result, the experimental setup shown in Figure 4.8, which involves a cryostat, was established to perform transmission experiments at various temperatures. A halogen lamp is used as the light source. Light from the halogen lamp is converged onto the sample through a lens. Light passes through the sample, which sits in the sample chamber of the cryostat, and is converged onto a monochromator through a second lens. The

monochromator has a photodetector attached to it, which converts the monochromatic light into electrical signal that is then read by a computer. We then obtain a reference beam, which is done by repeating the above procedure without the sample. The comparison of the transmitted light through the sample and the reference beam gives the absorption of light by the sample at wavelengths of interest.

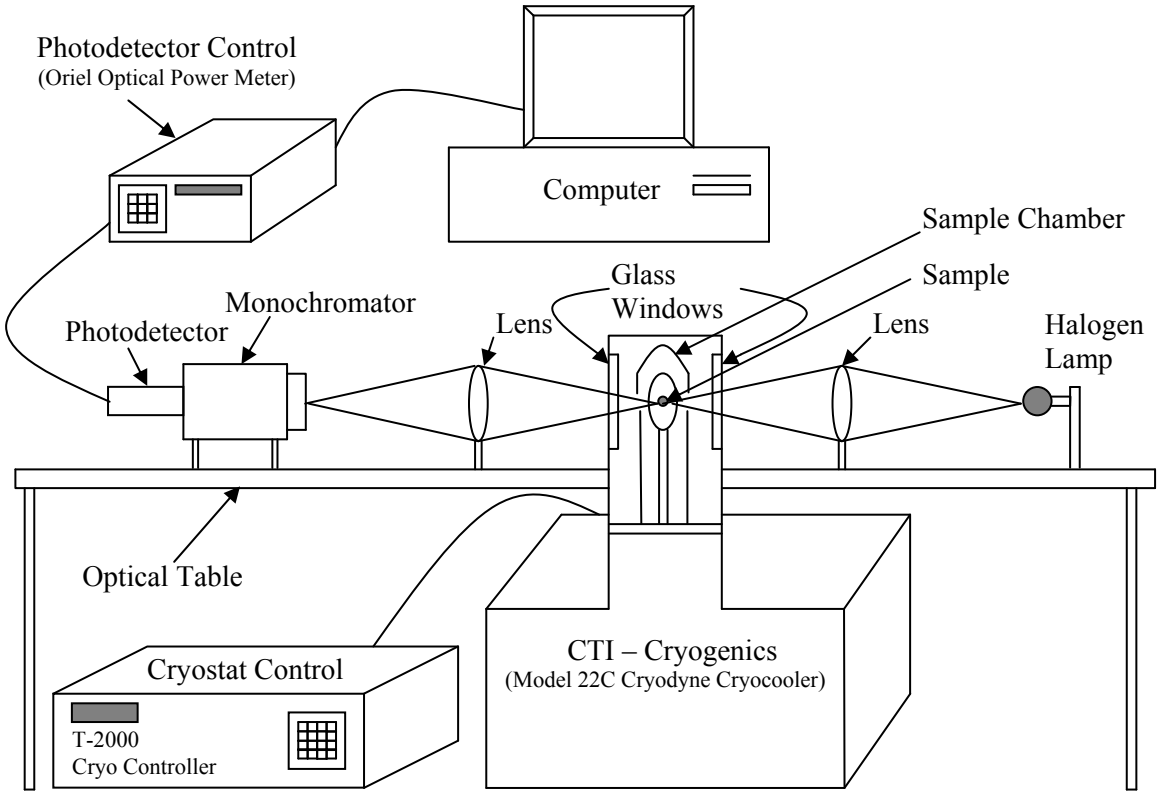

Figure 4.8: Schematic illustration of the experimental setup that involves a cryostat to obtain transmission spectra at various temperatures.

The cryostat used is, a 22C CRYODYNE CRYOCOOLER. This consists of two main parts, the cold head that comprises the sample chamber and a compressor unit. Figure 4.9 shows the different parts used in the cryostat assembly. The temperature range that can be achieved in the sample chamber is 300 K to 12 K. The monochromator used is, an

ORIEL cornerstone 1/8 m monochromator and the photodetector connected to it is, an ORIEL cooled InGaAs photodiode.

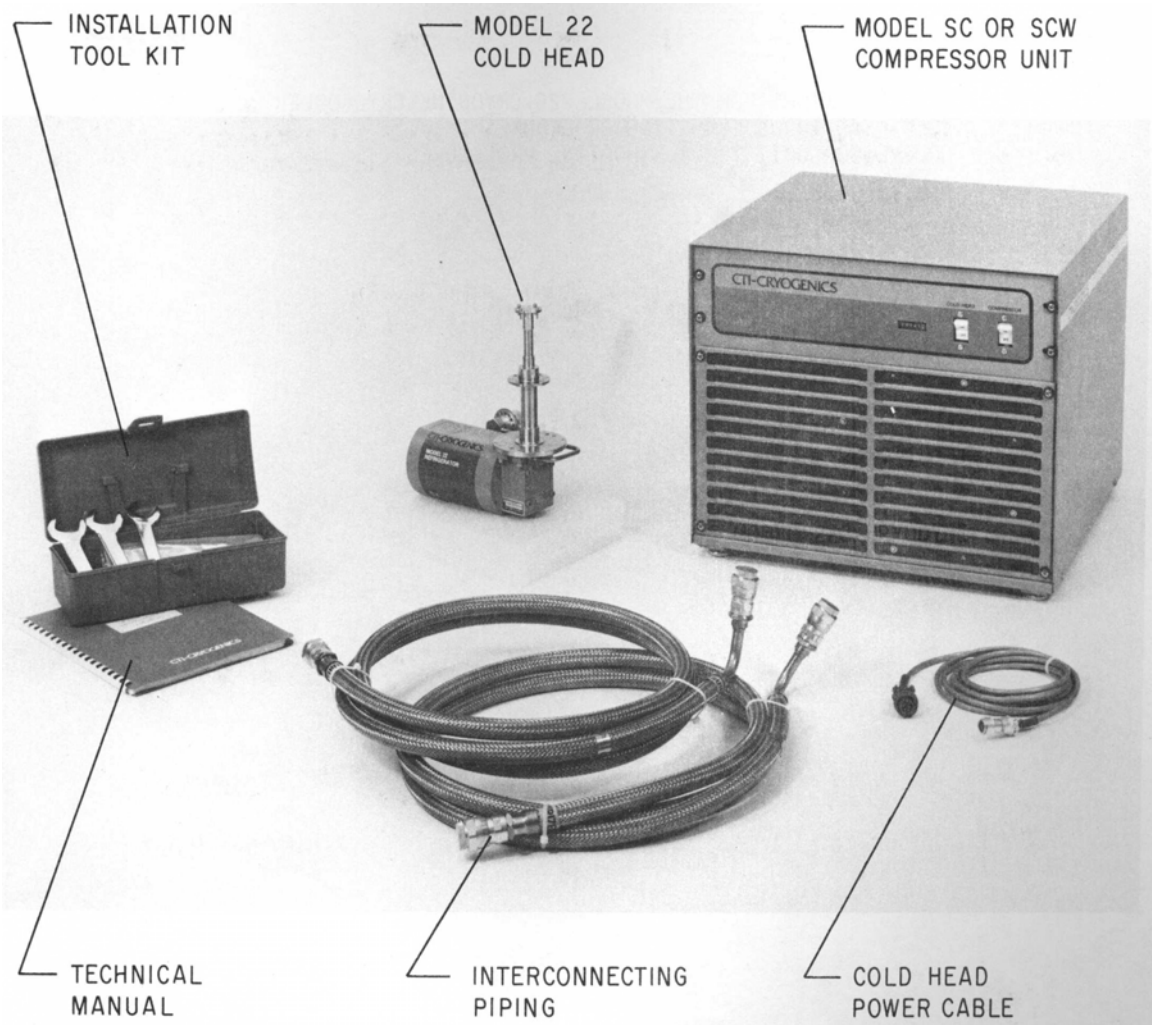

Figure 4.9: The different parts used in assembling the cryostat unit (from 22C CRYODYNE CRYOCOOLER'S manual).

4.5 Photoluminescence Measurements

There are two kinds of photoluminescence experiments that have been conducted in this research. One is, steady state photoluminescence, which deduces the emission spectra as a function of wavelength and the other is, decay photoluminescence or lifetime photoluminescence, which deduces the lifetime of ions in the excited states. In this section, we discuss the experimental setups established to perform these measurements. As well, at the end, a small section is devoted to the description of the procedure involved in obtaining powdered samples for some of the PL experiments.

4.5.1 Steady State Photoluminescence Measurements

In steady state photoluminescence experiments, we excite the sample with a laser source as shown in Figure 4.10. The operation wavelengths of the lasers used are 532 nm (green) and 808 nm (red). We have also used an ultraviolet lamp that operates at 360 nm as the excitation source for some of our experiments. Light from the source is projected onto the sample that sits in the sample chamber of the cryostat and the luminescence from the sample is converged onto a monochromator through a lens. The monochromatic light is then converted into an electrical signal by a photodetector that's attached to the monochromator. This signal is subsequently read by a computer, whereby we obtain the emission spectra as a function of wavelength.

Once again, as with the transmission experiments, it is necessary to vary the temperature of the sample for some PL measurements and hence the need for a cryostat. The cryostat and the monochromator/photodetector assembly used in the steady state photoluminescence experimental setup are the same as that mentioned in the previous section.

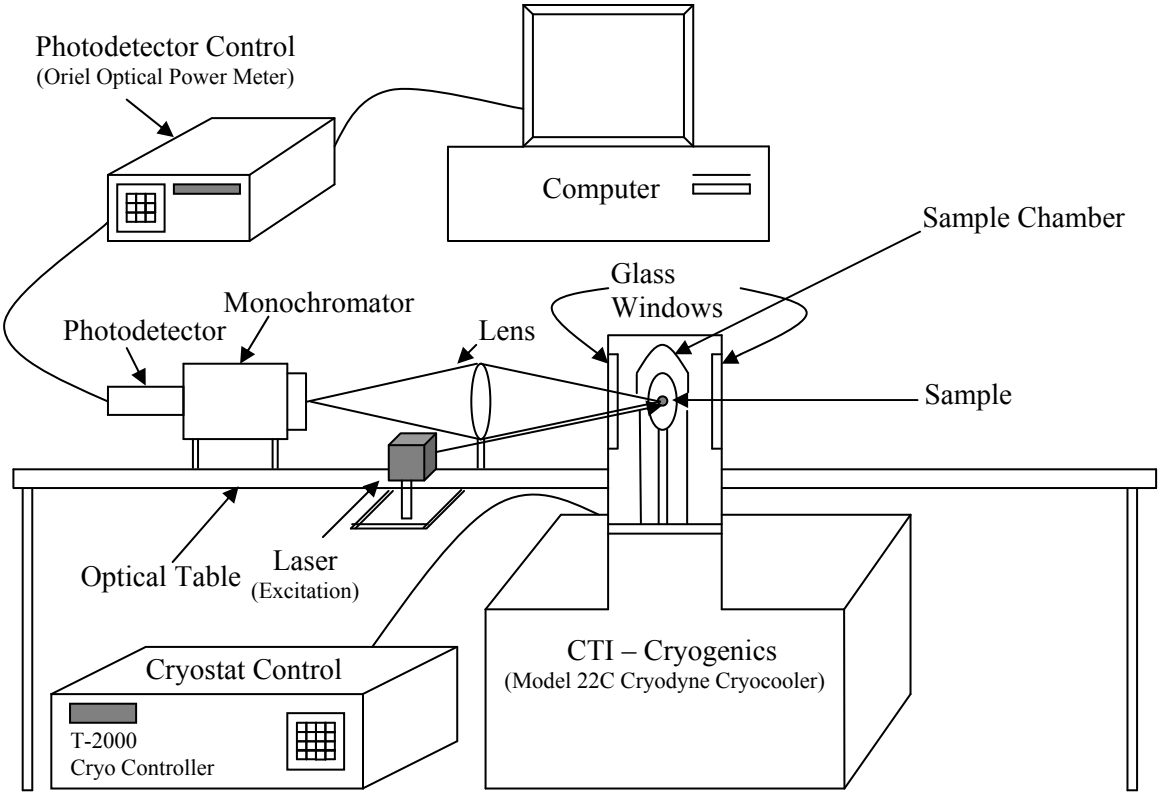

Figure 4.10: Schematic illustration of the steady state photoluminescence experimental setup.

4.5.2 Decay Photoluminescence or Lifetime Photoluminescence Measurements

The photoluminescence lifetimes of the rare earth ions, Neodymium and Erbium, in different glass hosts were measured using the experimental setup shown in Figure 4.11.

Light from an 808 nm laser source or 360 nm ultraviolet lamp is directed towards a mechanical chopper that modulates it into a square wave. The modulated beam is used to excite the rare earth ions in the sample being measured, producing the appropriate emission. This signal passes through a silicon filter, which removes any residual pump light. A germanium detector picks up the light signal and converts it into an electrical

signal which is then sent to a computer through a periscope. The exponential decay of the light signal seen after the chopper shuts off the pump beam is saved on the computer. This gives the lifetime of the rare earth ions in their excited states.

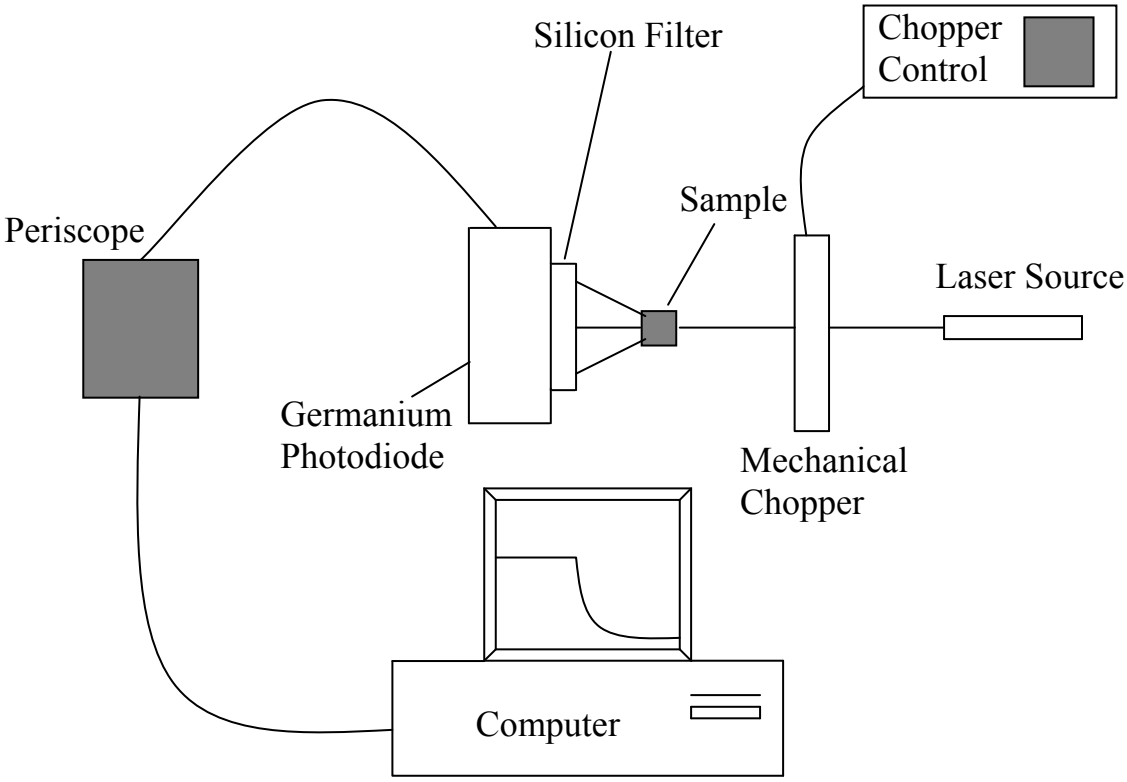

Figure 4.11: Schematic illustration of the experimental setup for measurement of PL lifetimes.

4.5.3 Sample Crushing

Some of the bulk samples were powdered by mechanical crushing using a mortar and pestle before performing steady state and lifetime measurements. Sequential sifting with sieves of different mesh sizes was then carried out to separate the powders based on their average size $\langle L \rangle$. $\langle L \rangle$ is estimated as one-half of the sum of two consecutive mesh sizes

for powdered samples and for bulk samples, it is estimated as the cubic root of their volume. A scotch tape with one sticky surface, which is transparent in the spectral range of interest and that shows no PL on its own, was used to collect the powder particles.

5. RESULTS AND DISCUSSION

5.1 Introduction

The sections in this chapter are distinguished based on the material that is being characterized. The materials investigated in this research are, Neodymium doped Gallium Lanthanum Sulfide glass, Erbium doped Germanium Gallium Sulfide glass, and Erbium doped Fluorochlorozirconate glass. Each section outlines the results obtained for the material under investigation and discusses the findings from the results.

5.2 Neodymium Doped Gallium Lanthanum Sulfide (GLS:Nd) Glass

The exact composition of the Neodymium doped Gallium Lanthanum Sulfide glass under investigation is, $(65Ga_2S_3):(31.5La_2S_3):(3La_2O_3):(0.5Nd_2S_3)$. This sample was manufactured from prepared batches of high purity (6N) powders by Professor Dan Hewak at the University of Southampton [46]. The sample was cut and polished, as explained in chapter 4, and used in obtaining the results detailed below.

The optical transmittance of $(65Ga_2S_3):(31.5La_2S_3):(3La_2O_3):(0.5Nd_2S_3)$ glass at room temperature is shown in Figure 5.1a and the optical absorption lines of Nd^{3+} ions are shown in Figure 5.1b. The optical absorption coefficient, which is used as the measure of absorption, is obtained from the transmittance curve via the following equation,

$$\alpha(\lambda) = \frac{1}{d} \ln \frac{T_0(\lambda)}{T(\lambda)} \qquad 5.1$$

where, $\alpha(\lambda)$ is the optical absorption coefficient, $T_0(\lambda)$ is the approximation of the transmittance of light through the sample if it hadn't been doped with Nd^{3+} ions, $T(\lambda)$ is the transmittance of light through the sample in the presence Nd^{3+} ions and d is the thickness of the bulk sample.

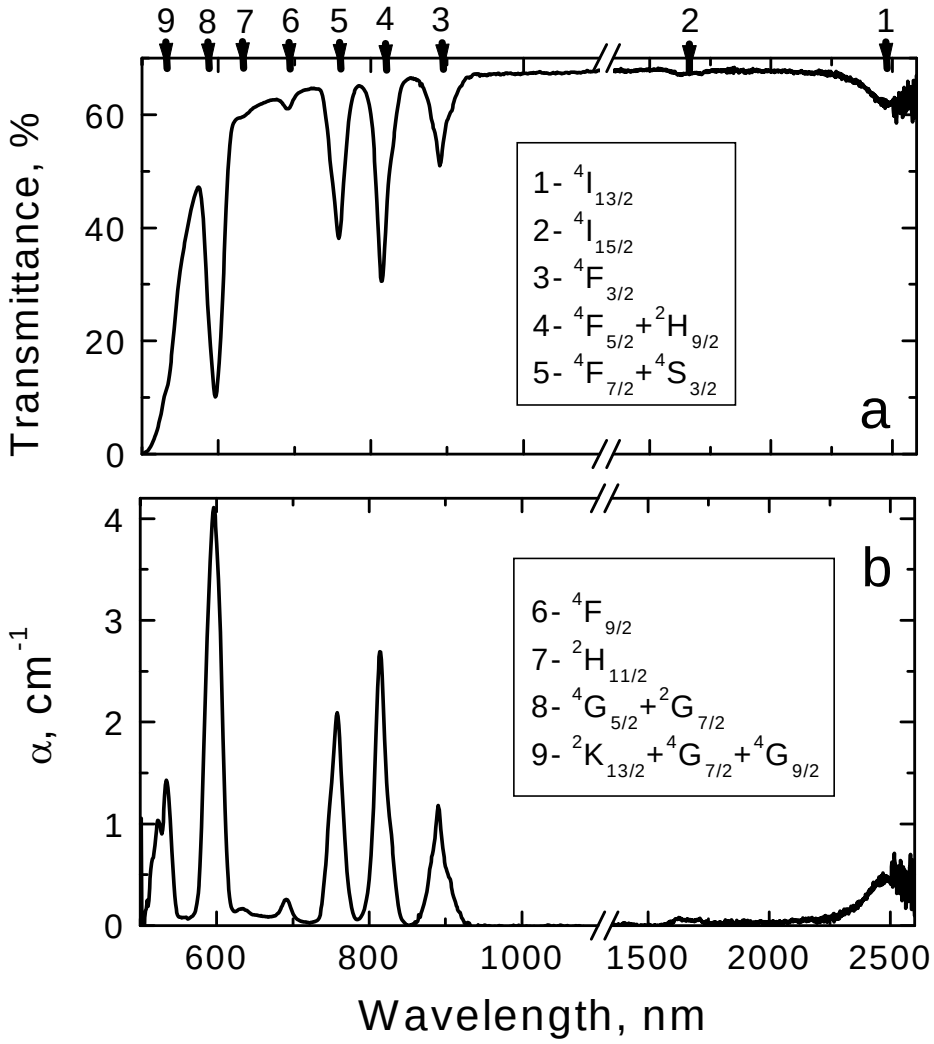

Figure 5.1: (a) Optical Transmittance and (b) Optical absorption lines of Nd^{3+} ions in $(65Ga_2S_3):(31.5La_2S_3):(3La_2O_3):(0.5Nd_2S_3)$ glass. The inset shows the tentative interpretation of the absorption lines from the ground state to the appropriate excited levels. (After [47])

The ion concentration in this sample is estimated, from the composition of starting ingredients, to be $N_i = 8.9\times10^{19}$ cm^{-3}. Data from Figure 5.1b is used to perform Judd-Ofelt analysis to obtain the Ω parameters, $\Omega_2 = 6.9\times10^{-20}$ cm^2, $\Omega_4 = 2.9\times10^{-20}$ cm^2 and $\Omega_6 = 1.7\times10^{-20}$ cm^2. A smaller Ω_2 parameter has been associated with the nature of the chemical bonds being more ionic than covalent and low Ω_4 and Ω_6 values may be attributed to the rigidity of the host matrix [54]. Therefore, it can be concluded that the glass is covalent in nature with a relatively "flexible" host matrix.

The procedure to obtain the Ω_λ (λ = 2, 4, 6) parameters and the radiative lifetime is as follows,

The electric-dipole line strengths, S^k_{EXP} (k = 1, 2, 3 …N), are calculated for N absorption bands using equation 3.4 and the areas under the absorption coefficient bands calculated from Figure 5.1b. These values are compared with the theoretically calculated electric-dipole line strengths, S^k_{CAL}, which are obtained by summing the products of the Ω_λ parameters with the appropriate reduced tensor operators, U_λ, which can be found in literature. The sum $\sum_k (S^k{}_{EXP} - S^k{}_{CAL})^2$ is numerically minimized by choosing the appropriate Ω_λ parameters. The initial Ω_λ values for the minimization process are chosen randomly in analogy with the published data for similar glasses and rare earths.

Using the established Ω_λ parameters and the appropriate reduced tensor operators, U_λ, the line strength for the emission energy level of interest is calculated. This in turn is used in equation 3.2 to calculate the probability of spontaneous emission, A. The inverse of A gives the radiative lifetime (Judd-Ofelt lifetime), τ_{JO}, of the emitting level.

The lifetime of a level can be defined as the inverse of the probability per unit time of the exit of an ion from that excited level. For a group of excited ions in a given level, the population then drops exponentially with a time constant equal to the lifetime. The radiative lifetime (Judd-Ofelt lifetime) of the $^4F_{3/2}$ manifold is estimated to be, τ_{JO} = 87

μs. The Judd-Ofelt lifetime includes the radiative escapes to the $^4I_{15/2}$, $^4I_{13/2}$, $^4I_{11/2}$ and $^4I_{9/2}$ manifolds. The branching ratios, β, from the $^4F_{3/2}$ manifold to the $^4I_{15/2}$, $^4I_{13/2}$, $^4I_{11/2}$ and $^4I_{9/2}$ manifolds are also calculated and are 0.546, 0.384, 0.068 and 0.002 respectively.

Figure 5.2 shows the experimental investigation of PL decays, after the interruption of illumination, measured at 897, 1100 and 1350 nm corresponding to $^4F_{3/2} \rightarrow {}^4I_{9/2}$, $^4F_{3/2} \rightarrow {}^4I_{11/2}$ and $^4F_{3/2} \rightarrow {}^4I_{13/2}$ transitions that reveal characteristic decay times, $\tau_{D,}$ of 86, 91 and 89 μs, respectively. The solid cyan line is a guide to the eye corresponding to the exponential decay with a characteristic time, τ_D = 95 μs. The closeness of τ_D and τ_{JO} concludes that the dominant relaxation mechanism from the $^4F_{3/2}$ excited manifold of Nd^{3+} ions in GLS glass is by radiative emission. The excitation source that was used for all decay experiments is a 532 nm laser diode.

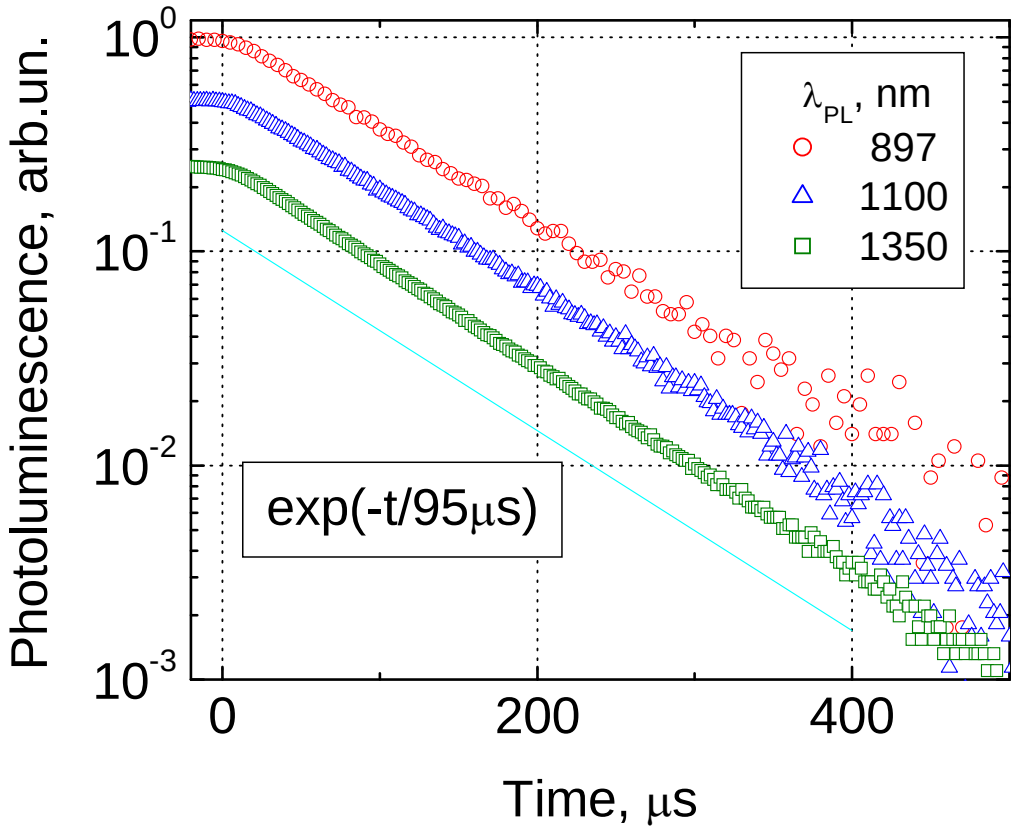

Figure 5.2: Photoluminescence decays measured at 897, 1100 and 1350 nm corresponding to the $^4F_{3/2} \rightarrow {}^4I_{9/2}$, $^4F_{3/2} \rightarrow {}^4I_{11/2}$ and $^4F_{3/2} \rightarrow {}^4I_{13/2}$ transitions, respectively. The solid cyan line is a guide to the eye corresponding to the exponential decay with a characteristic time of 95 μs. (After [47])

Further analysis has mainly been focused on the 850 – 950 nm spectral range, which relates to the $^4I_{9/2} \leftrightarrow {}^4F_{3/2}$ optical transitions, as both absorption and emission spectra overlap in this range. Figure 5.3 determines the Stark components in optical absorption (a-c) and photoluminescence (d-e) corresponding to the $^4I_{9/2} \leftrightarrow {}^4F_{3/2}$ transitions of Nd^{3+} ions. Red lines with symbols represent experimental data, cyan lines represent individual Gaussians and blue lines represent the sum of all Gaussians. The transitions between the $^4I_{9/2}$ and $^4F_{3/2}$ manifolds at the given temperature are shown in the insets.

The degeneracy of the energy level of momentum J can be represented as $J + 1/2$ [48]. From which, it is deduced that the $^4I_{9/2}$ manifold consists of five Stark levels and the $^4F_{3/2}$ manifold consists of only two Stark levels. Ten optical transitions forming overlapping bands can be observed if the degeneracy of these levels is completely lifted. In laser crystal hosts these transitions form well separated lines [49], whereas in glass hosts they are highly intermingled forming overlapping bands. Temperature measurements may help simplify the interpretation of optical spectra [50]. It is well known that level populations follow Boltzmann distribution [51]. Therefore, the population of the highest level of the $^4I_{9/2}$ manifold is negligible at 12 K. As a result, only two optical transitions are possible as shown in the inset of Figure 5.3a. These transitions are from the lowest level of the $^4I_{9/2}$ to both levels of the $^4F_{3/2}$ manifold. The absorption band, at 12 K, is approximated as the sum of two Gaussians centered at 11, 218 and at 11, 351 cm^{-1}, which can be attributed to the two Stark levels in the $^4F_{3/2}$ manifold.

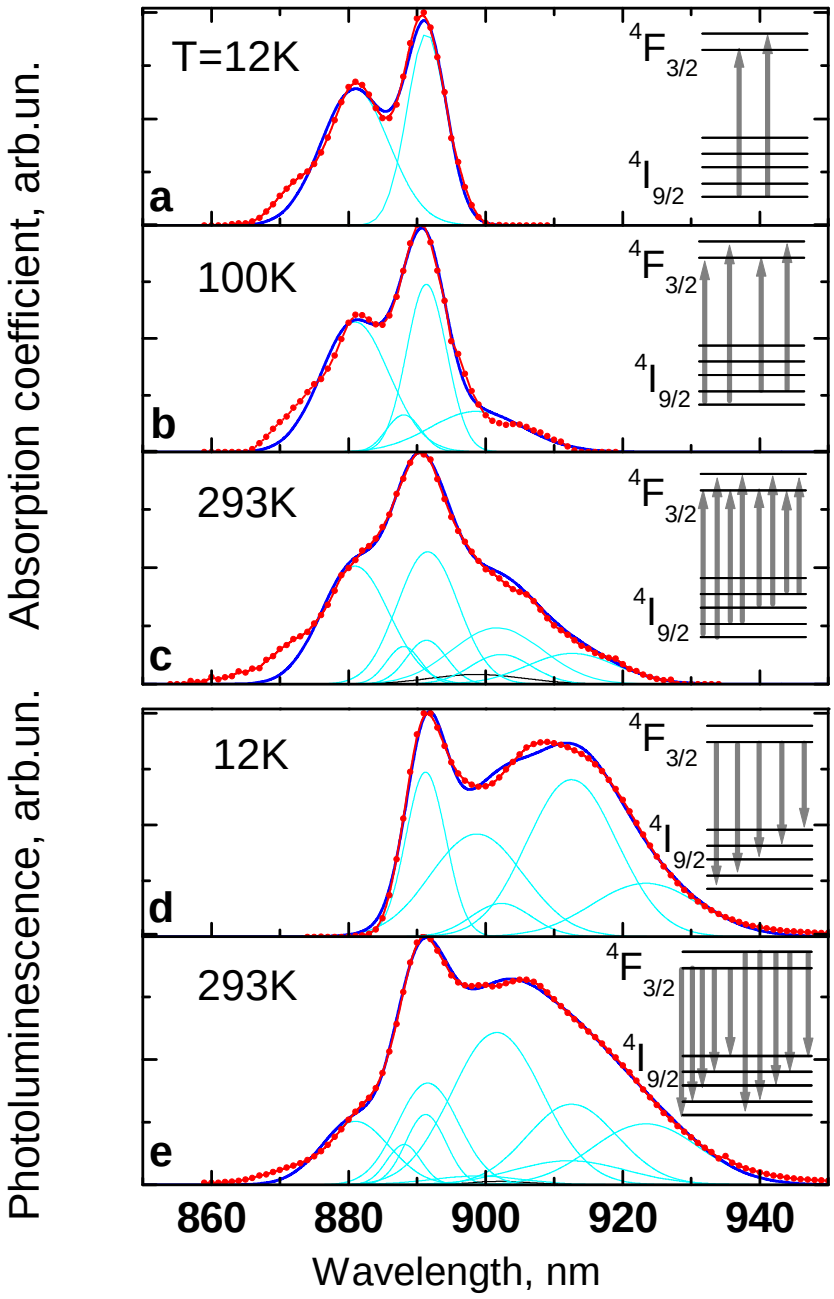

Figure 5.3: Determination of Stark components in optical absorption (a-c) and photoluminescence (d-e) corresponding to the $^4I_{9/2} \leftrightarrow {}^4F_{3/2}$ transitions of Nd^{3+} ions. Red lines with symbols represent experimental data, cyan lines represent individual Gaussians and blue lines represent the sum of all Gaussians. The transitions between the $^4I_{9/2}$ and $^4F_{3/2}$ manifolds at the given temperature are shown in the insets. (After [47])

As temperature increases, more and more of the upper levels of the $^4I_{9/2}$ manifold get populated. So, as seen in the inset of Figure 5.3b, at 100 K, the population of the second level of the $^4I_{9/2}$ manifold and the associated transitions are taken into consideration. Now, a sum of four Gaussians may be used to approximate the overall optical band. Two of which use the same half-widths and positions defined previously at 12 K and only the two new ones are subject to optimization. From which, the separation between the lowest and the second Stark level of the $^4I_{9/2}$ manifold may be deduced to be 91 cm^{-1}. In a similar fashion, as seen in the inset of Figure 5.3c, at 293 K, eight optical transitions are taken into considerations. Amongst which, four are new. The four new Gaussians help in determining the positions of the third and fourth Stark levels of the $^4I_{9/2}$ manifold as 135 and 260 cm^{-1}, respectively. It is not possible to resolve the position of the fifth level of the $^4I_{9/2}$ manifold from absorption spectra. This necessitates the investigation of the photoluminescence spectra.

As seen in the inset of Figure 5.3d, at 12 K, all PL transitions start from the lowest level of the $^4F_{3/2}$ manifold and end in the various levels of the $^4I_{9/2}$ manifold. From which, the position of the fifth Stark level of the $^4I_{9/2}$ manifold is obtained as 388 cm^{-1}. All Stark levels are now determined. From Figure 5.3e, it can be seen that all ten PL transitions are possible. The PL transitions can indeed be de-convoluted into the sum of Gaussians with previously defined positions and the validity of the model is checked. In conclusion, the positions of the five Stark levels of the $^4I_{9/2}$ manifold maybe identified as, $E_1 = 0$, $E_2 = 91$, $E_3 = 135$, $E_4 = 260$ and $E_5 = 388$ cm^{-1} and the positions of the two Stark levels of the excited $^4F_{3/2}$ manifold maybe identified as $E_6 = 11,218$ and $E_7 = 11,351$ cm^{-1} [47].

The net thermo-dynamical free energy required to move one Nd^{3+} ion from the ground ($^4I_{9/2}$) state to the excited ($^4F_{3/2}$) state can be calculated from the energy positions of these Stark levels [52].

$$\varepsilon = -k_B T \log\left(\frac{\sum_{k=6}^{7} \exp\left(-\frac{E_k}{k_B T}\right)}{\sum_{k=1}^{5} \exp\left(-\frac{E_k}{k_B T}\right)}\right); \qquad \varepsilon = 1.40\,\text{eV or}\,11325\,\text{cm}^{-1} \tag{5.2}$$

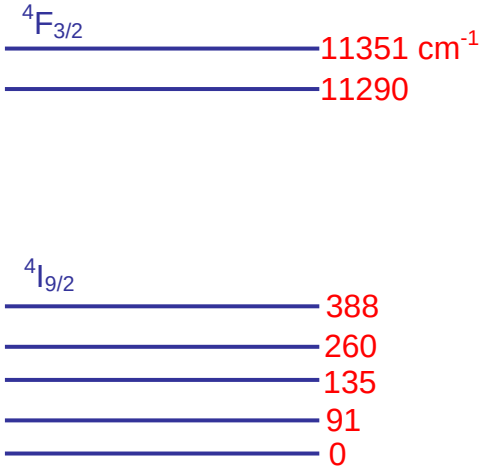

Figure 5.4: Energy positions of the five Stark levels of the $^4I_{9/2}$ manifold and the two Stark levels of the excited $^4F_{3/2}$ manifold.

The value, ε, can now be used to calculate the emission cross-section through McCumber theory [51],

$$\sigma_e(\nu) = \sigma_a(\nu) \exp\left(\frac{\varepsilon - h\nu}{k_B T}\right) \tag{5.3}$$

where $\sigma_e(\nu)$ and $\sigma_a(\nu)$ are emission and absorption cross-sections, respectively, $h\upsilon$ is photon energy and $k_B T$ = 203 cm^{-1} at room temperature. Figure 5.5 shows the calculated results. The PL spectrum is normalized using the calculated values of $\sigma_e(\nu)$ and thus

obtaining the absolute values for the emission cross-section with the maximum value at $\sim 2.3\times10^{-20}$ cm^2 [47]. From Figure 5.5, it can be seen that there's a good agreement between the experimentally measured PL(υ) and the predictions of McCumber theory.

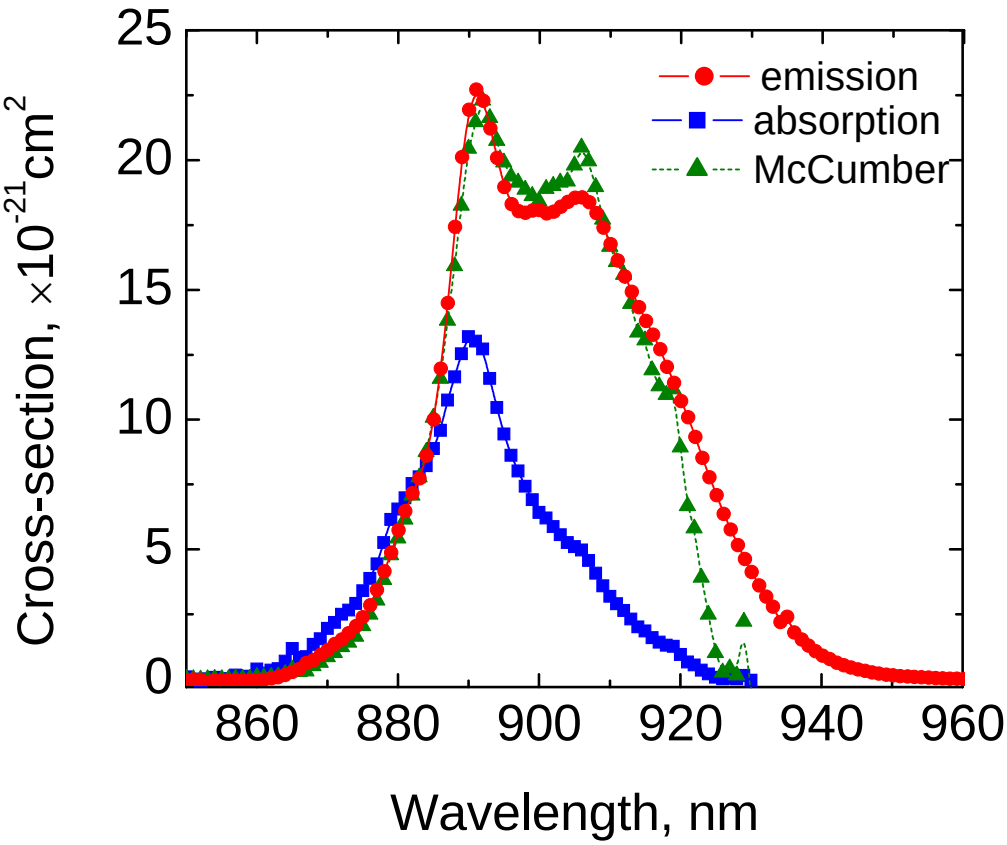

Figure 5.5: Experimental absorption and emission cross-section spectra of the $^4I_{9/2} \leftrightarrow {}^4F_{3/2}$ transitions of Nd^{3+} ions compared with the predictions of McCumber theory. (After [47])

5.3 Erbium Doped Germanium Gallium Sulfide (GeGaS:Er) Glass

The composition of the glass used is, $Ge_{28}Ga_{6.2}S_{65.3}:Er_{0.5}$. This sample was prepared in our own laboratory by Dr. Martin Munzar as outlined in chapter 4. The sample was cut and polished and used in obtaining the results detailed below.

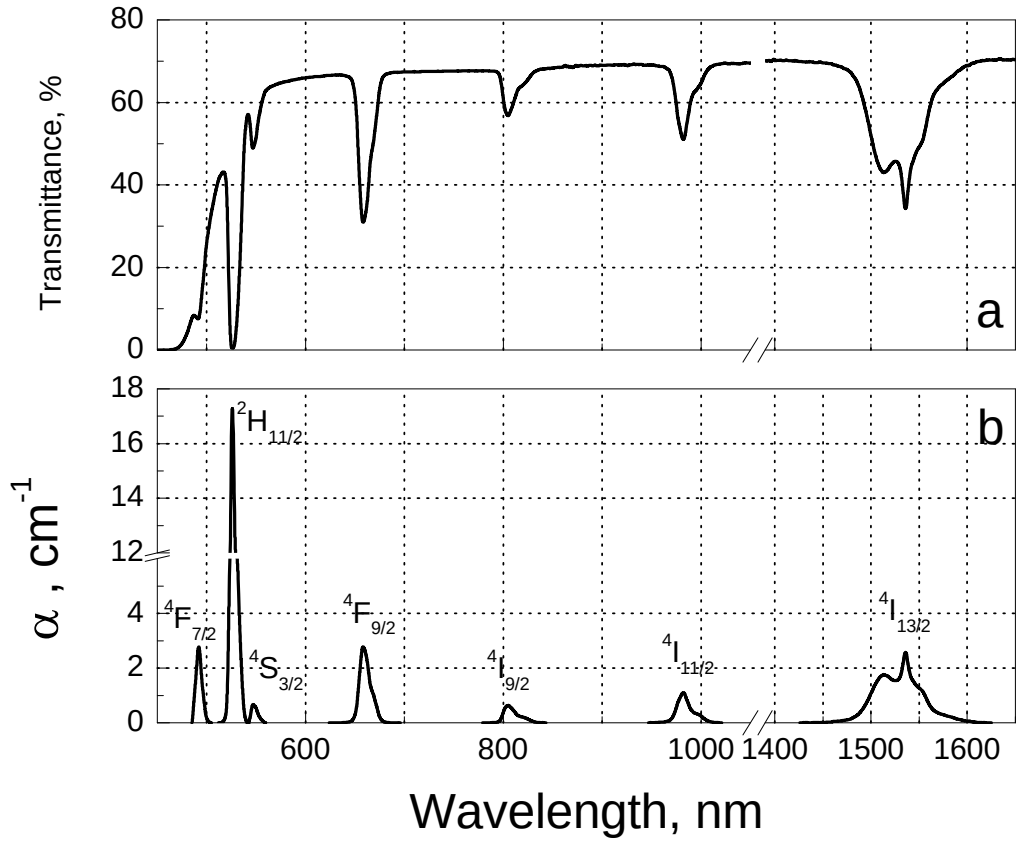

Figure 5.6: (a) Optical Transmittance and (b) Optical absorption lines of Er^{3+} ions in $Ge_{28}Ga_{6.2}S_{65.3}:Er_{0.5}$ glass. The tentative interpretation of the absorption lines from ground level to the appropriate excited level is also shown in (b). (After [53])

The optical transmittance of $Ge_{28}Ga_{6.2}S_{65.3}:Er_{0.5}$ at room temperature is shown in Figure 5.6a and the optical absorption lines of Er^{3+} ions with their tentative interpretation, according to the names of the excited levels, is shown in Figure 5.6b. The absorption lines are strong and broad and are centered at approximately, 1540, 980, 805, 660, 547, 526 and 490 nm corresponding to optical transitions from the $^4I_{15/2}$ manifold to the $^4I_{13/2}$, $^4I_{11/2}$, $^4I_{9/2}$, $^4F_{9/2}$, $^4S_{3/2}$, $^2H_{11/2}$ and $^4F_{7/2}$ manifolds in Er^{3+} ions, respectively. The ion concentration in this sample is estimated to be $N_i = 2.1\times10^{20}$ cm^{-3}.

Data from Figure 5.6b is used to perform Judd-Ofelt analysis to obtain the Ω parameters, $\Omega_2 = (10.5\pm1)\times10^{-20}$ cm^2, $\Omega_4 = (3\pm0.3)\times10^{-20}$ cm^2 and $\Omega_6 = (1.6\pm0.2)\times10^{-20}$ cm^2. Based on the literature from [54], the values obtained here for the Ω parameters suggest that the glass under investigation is strongly covalently bonded with a relatively "flexible" host matrix.

Using the Judd-Ofelt parameters, the radiative lifetime (Judd-Ofelt lifetime) of the $^4I_{13/2}$ manifold to the ground level is estimated as, τ_{JO} = 2.5 ms. Since the telecommunications wavelength is 1550 nm, the analysis has been concentrated on the 1450 – 1650 nm spectral range. The branching ratio, β, for the $^4I_{13/2} \rightarrow {}^4I_{15/2}$ transition is estimated to be 1 as it should be because there are no energy levels between the $^4I_{13/2}$ and $^4I_{15/2}$ levels.

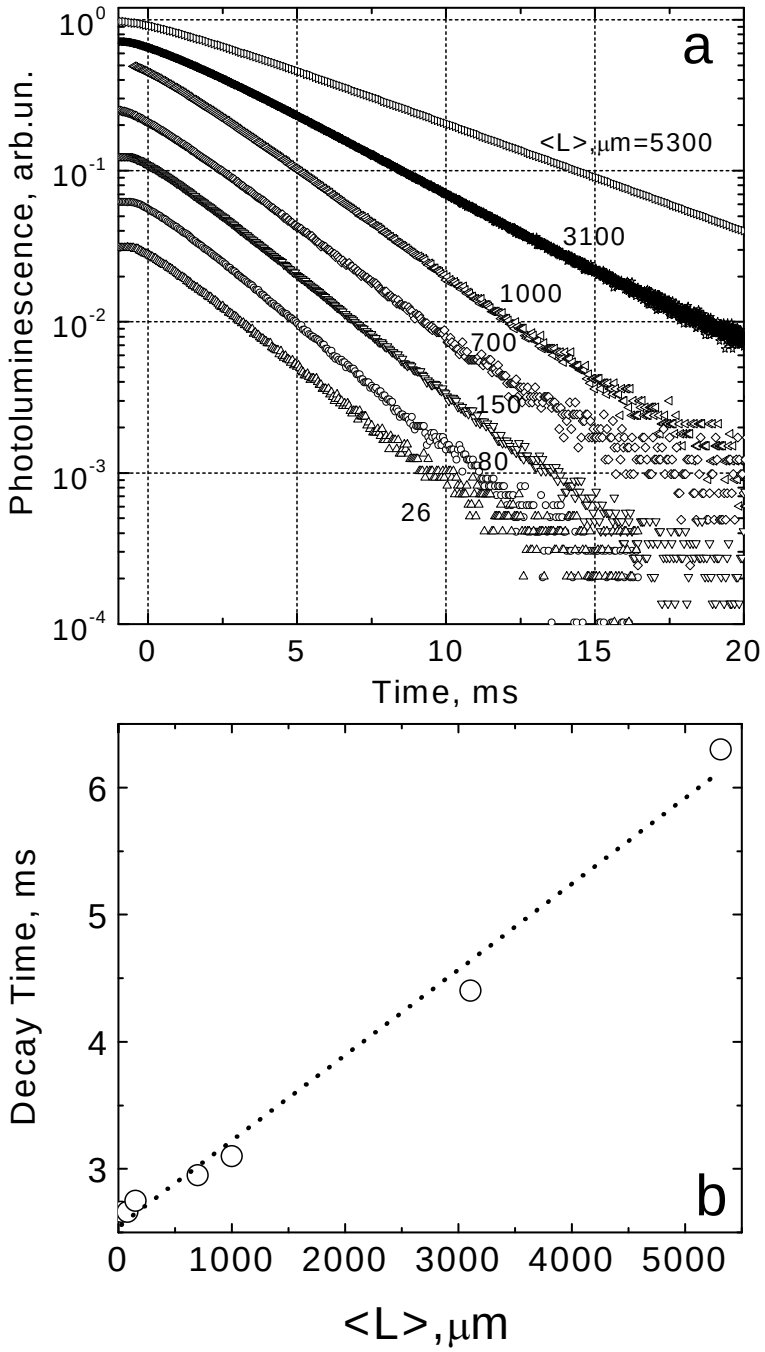

Figure 5.7: (a) PL decays after excitation ceases. (b) PL decay time versus average sample <*L*> size of powdered and bulk samples. The excitation source used is an 808 nm laser diode. (After [53])

The measurement of lifetime, in heavily doped materials, may be affected by the energy diffusion of Er^{3+} ions in the system. This diffusion could occur non-radiatively or radiatively. Non-radiative diffusion occurs mostly via ion – ion interactions as explained in chapter 3. This leads to the "self-quenching" of Er^{3+} ions. This process effectively reduces the measured PL lifetime [53]. Radiative diffusion is caused by "photon or radiation trapping." It's the successive acts of absorption-emission by different Er^{3+} ions that causes energy diffusion [53]. The large overlap of absorption and emission bands, which is common for $^4I_{13/2} \leftrightarrow {}^4I_{15/2}$ transitions, is mostly responsible for such trapping [53]. The PL decay time, obviously, increases due to photon trapping [55]. A substantial disagreement between the experimentally determined PL decay time (τ_D) and the real radiative lifetime (τ_{JO}) may arise due to the interplay of these two effects [56].

Figure 5.7 shows the PL decays for the 1550 nm emission for bulk and powdered GeGaS:Er samples. From which, it is clear that $\tau_D \geq \tau_{JO}$. This implies the dominance of radiation trapping. This effect may be suppressed in powdered or thin film materials. Mattarelli *et al*. [57] have shown that the lifetime measured on bulk samples is indeed substantially longer than that measured on powders by examining decay time of the 1.5 μm PL emission from bulk and powdered Er^{3+} doped tellurite samples. The importance of this effect can be seen in Figure 5.7. The dependence of the decay time τ_D on sample size is shown in Figure 5.7b. This dependence is almost linear and is approximated by a least-squares fit that gives the value of τ_D = 2.56 ms for infinitely fine powders, which is very close to the theoretically calculated τ_{JO} [53].

A few conclusions can be drawn based on this closeness of τ_D and τ_{JO}. Firstly, we can rule out self-quenching as a diffusion mechanism. Secondly, τ_D represents real radiative lifetime and thirdly, the radiative lifetime may very well be directly measured via PL decay experiment on fine powders of GeGaS:Er.

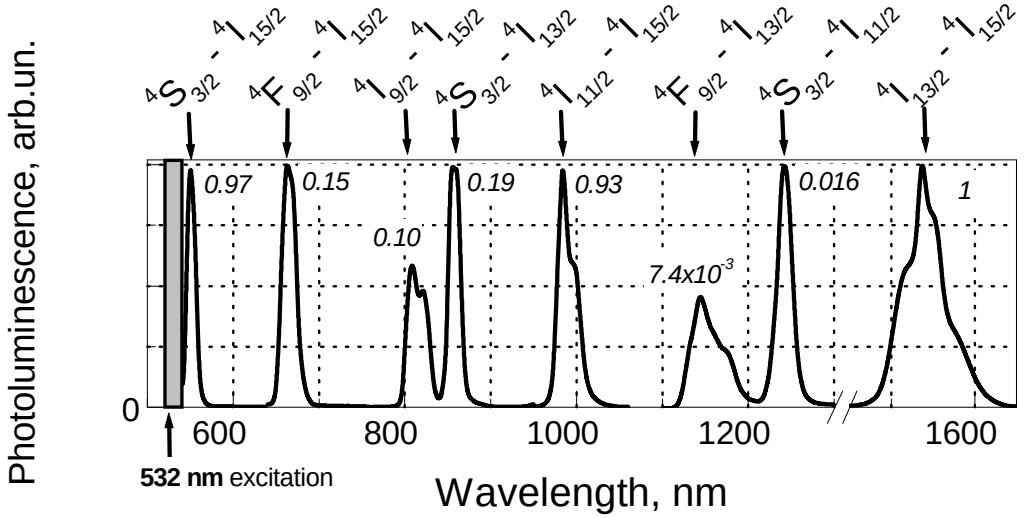

Figure 5.8: PL Spectra from 540 nm to 1650 nm under 532 nm laser excitation. The tentative interpretation of the emission transitions are shown at the top with arrows pointing to the respective bands.

Figure 5.8 shows the PL spectra for the GeGaS:Er bulk sample from 540 nm to 1650 nm under 532 nm laser excitation. The tentative interpretation of the emission transitions are shown at the top with arrows pointing to the respective bands. The numbers beside each band represent the peak intensity of that band, with all bands normalized with respect to the 1550 nm emission band. Of the PL bands observed, focus has been laid on the 1.5 μm emission band corresponding to the $^4I_{13/2} \rightarrow {}^4I_{15/2}$ transitions.

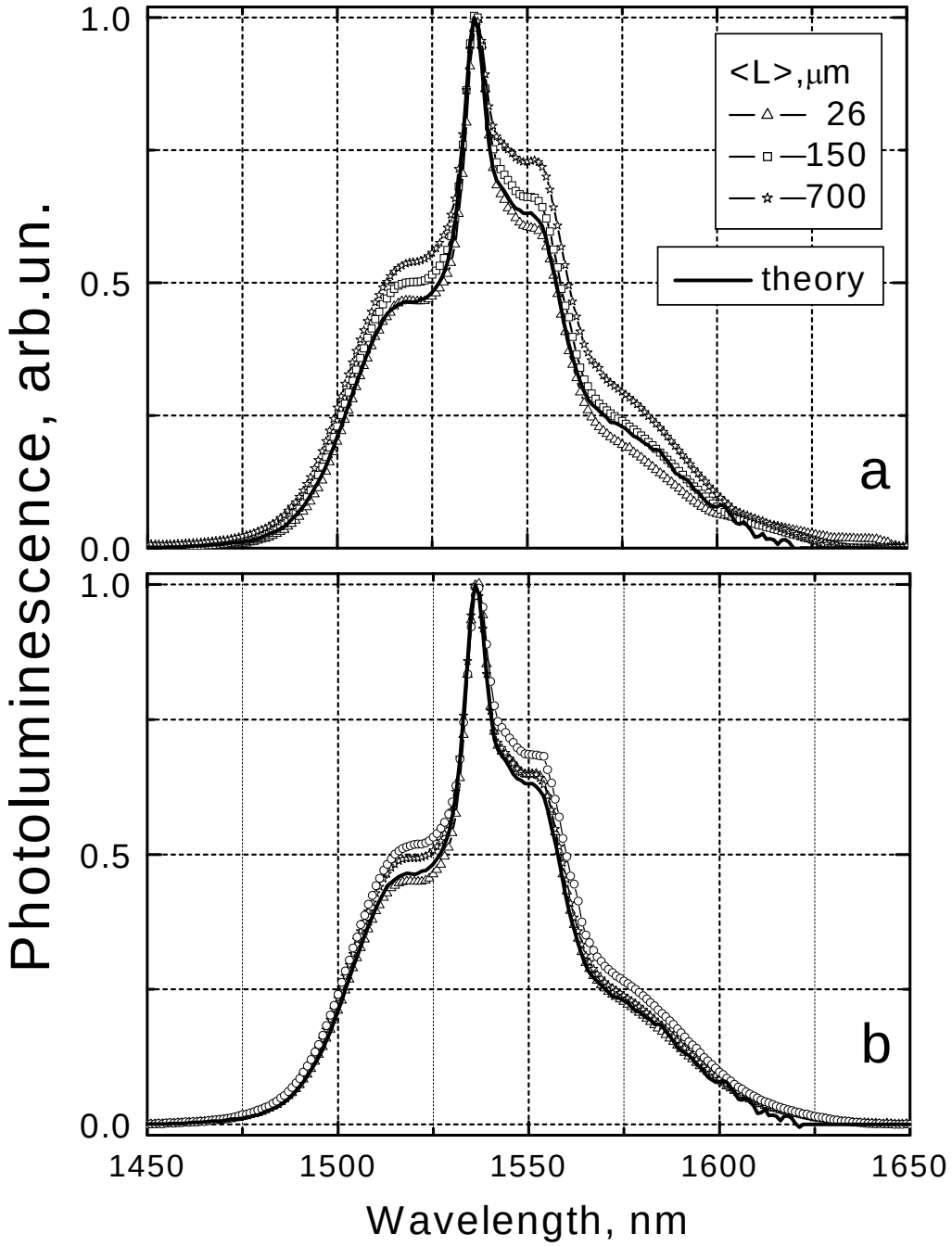

Figure 5.9: Measured PL spectra of various average particle sizes, <*L*>. Excitation source used is a laser diode operating at (a) 808 nm and (b) 532 nm. (After [53])

Figure 5.9 compares the PL spectra measured in samples of various average particle sizes, <*L*>, under different excitations. The emission spectrum is used in deriving the spectral shape of the emission cross section, but the shape of the spectrum may be significantly distorted due to radiation diffusion [57, 58, 59]. It has been reported by Mattarelli *et al*. [57] that the 1.5 μm emission spectrum in bulk Er^{3+} doped tellurite glasses is broader than that in powders. They have attributed this broadening to re-absorption, that is, photon trapping.

The excitation sources used in obtaining the PL spectra are laser diodes operating at 532 nm (optical absorption is strong and is by both Er^{3+} ions and the host matrix) and 808 nm (optical absorption is weak and is only by Er^{3+} ions). As <*L*> increases the spectra become broader and with 808 nm excitation the broadening is more pronounced. Under 532 nm excitation on powders with <*L*> = 26 μm, it can be seen that the measured PL spectrum and the predictions of McCumber theory are in nearly perfect agreement. From this, it can be concluded that the actual spectral shape of the emission cross section may be determined from the measured PL spectra using strongly absorbed excitation in fine powders.

5.4 Erbium Doped Fluorochlorozirconate (FCZ:Er) Glass

Erbium doped fluorochlorozirconate glasses were prepared at Victoria University by Dr. Andrew Edgar [60]. The samples were cut and polished as explained in chapter 4 and used in obtaining the results brought forward in this section.

Transmittance experiment was performed on FCZ glasses doped with 1% and 2% erbium and the outcomes are shown in Figure 5.10 and Figure 5.11, respectively. Since the absorption bands in FCZ:Er(1%) are not so pronounced, further experiments and analysis were concentrated on FCZ:Er(2%).

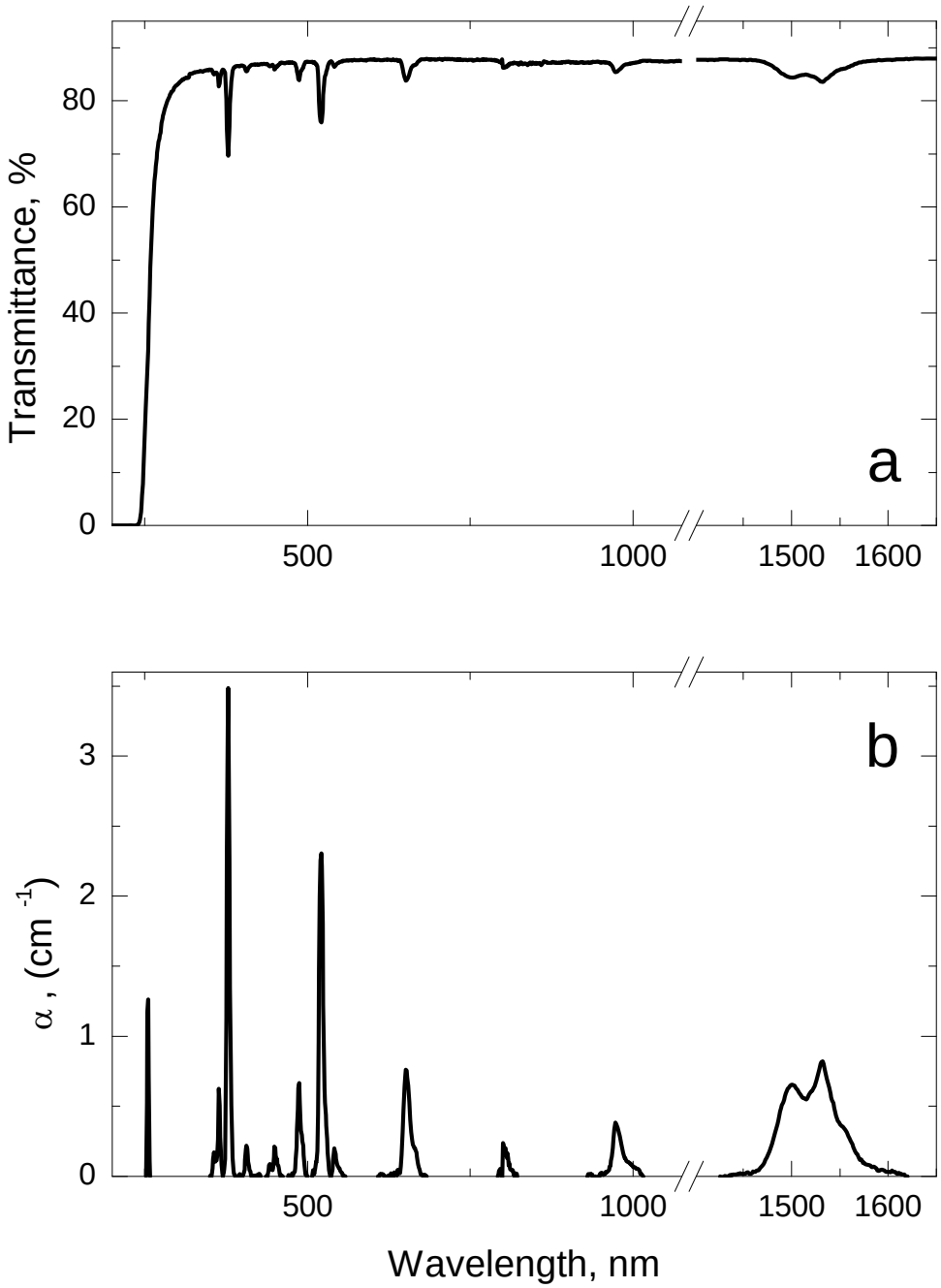

Figure 5.10: (a) Optical Transmittance and (b) Optical absorption lines of Er^{3+} ions in $53.39ZrF_4+2.94LaF_3+3.01AlF_3+0.49BaF_2+19.76NaF+0.50InF_3+18.89BaCl_2+1.02ErCl_3$ glass.

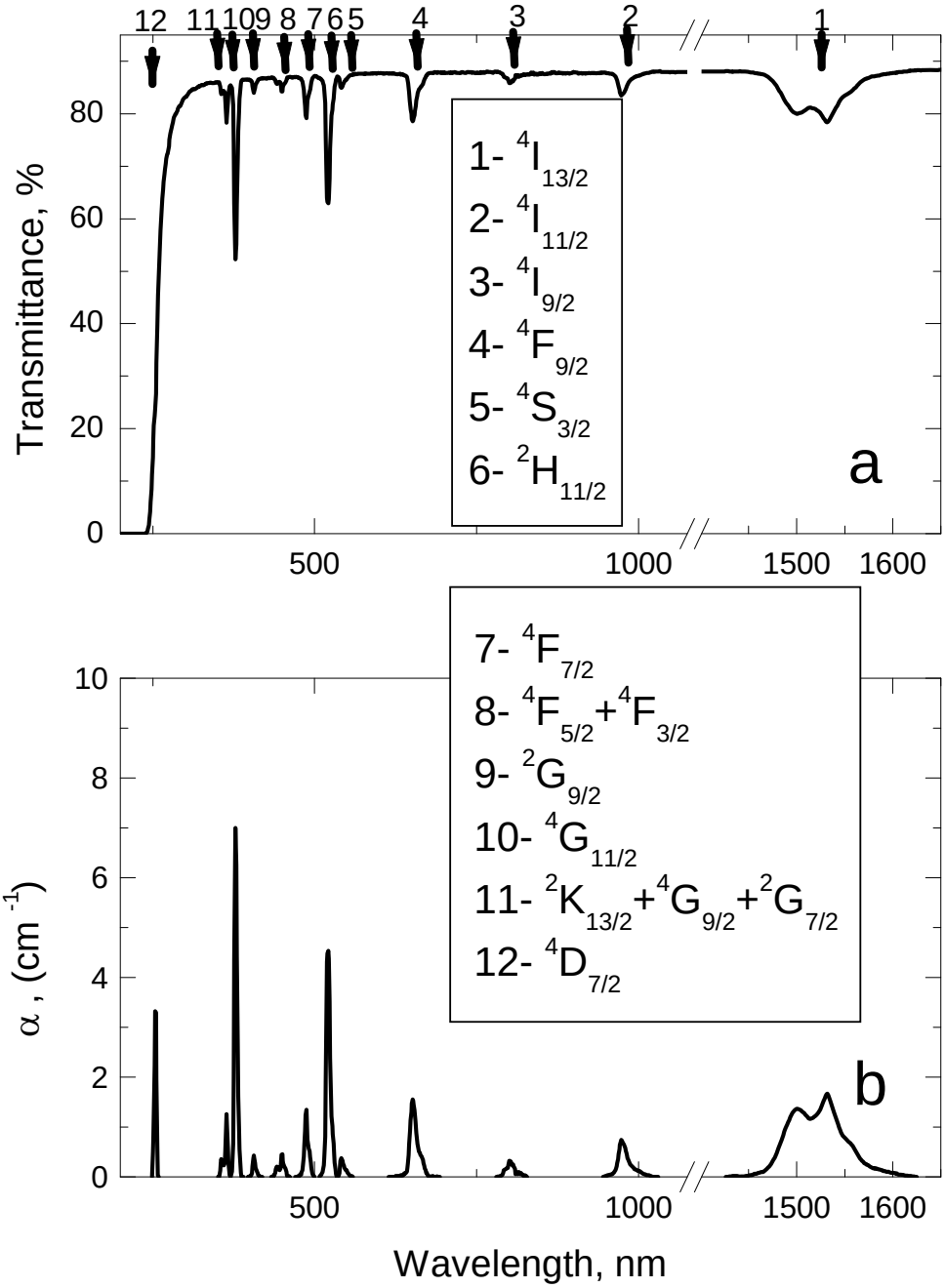

Figure 5.11: (a) Optical Transmittance and (b) Optical absorption lines of Er^{3+} ions in $53.22ZrF_4+3.06LaF_3+3.23AlF_3+19.68NaF+0.52InF_3+18.30BaCl_2+1.99ErCl_3$ glass. The inset shows the tentative interpretation of the absorption lines from the ground state to the appropriate excited levels.

The optical transmittance of $53.22ZrF_4+3.06LaF_3+3.23AlF_3+19.68NaF+0.52InF_3+18.30BaCl_2+1.99ErCl_3$ glass at room temperature is shown in Figure 5.11a and the optical absorption lines of Er^{3+} ions with their tentative interpretation, according to the names of the excited levels, is shown in Figure 5.11b. The absorption lines are broad and are centered at approximately, 1532, 973, 801, 651, 541, 521, 487, 450, 406, 378, 364, and 254 nm corresponding to optical transitions from the $^4I_{15/2}$ manifold to the $^4I_{13/2}$, $^4I_{11/2}$, $^4I_{9/2}$, $^4F_{9/2}$, $^4S_{3/2}$, $^2H_{11/2}$, $^4F_{7/2}$, $^4F_{5/2}$ $+^4F_{3/2}$, $^2G_{9/2}$, $^4G_{11/2}$, $^2K_{3/2}+^4G_{9/2}+^2G_{7/2}$ and $^4D_{7/2}$ manifolds in Er^{3+} ions, respectively. The ion concentration in this sample is estimated to be $N_i = 4.64\times10^{20}$ cm^{-3}.

Data from Figure 5.11b is used to perform Judd-Ofelt analysis to obtain the Ω parameters, $\Omega_2 = (0.6\pm0.1)\times10^{-20}$ cm^2, $\Omega_4 = (0.9\pm0.2)\times10^{-20}$ cm^2 and $\Omega_6 = (1.9\pm0.3)\times10^{-20}$ cm^2. Based on the low Ω parameters, it can be concluded that the glass under investigation is strongly ionic with a relatively rigid host matrix. The JO parameters are in turn used to estimate the radiative lifetime (Judd-Ofelt lifetime), τ_{JO} = 11±1 ms, of the $^4I_{13/2}$ manifold to the ground level. Once again, the analysis has been focused on the telecommunication wavelength, 1550 nm. The estimation for the branching ratio, β, for the $^4I_{13/2} \rightarrow {}^4I_{15/2}$ transition turns out to be 1.

Figure 5.12 shows the measured PL decay time (τ_D), after the interruption of illumination, at 1550 nm corresponding to the $^4I_{13/2} \rightarrow {}^4I_{15/2}$ transitions for different sample sizes. The excitation source used was an 808 nm laser diode. From Figure 5.12 it can be seen that there's no change in the PL decay time for changing sample sizes. This suggests in-efficient re-absorption of light. The dashed line is a guide to the eye corresponding to the exponential decay with a characteristic time, τ_D = 12 ms, which is in close agreement with the JO lifetime, τ_{JO} = 11±1 ms. This closeness of τ_D and τ_{JO} suggests that the dominant relaxation mechanism from the $^4I_{13/2}$ excited manifold of Er^{3+} ions in FCZ:Er(2%) glass is by radiative emission.

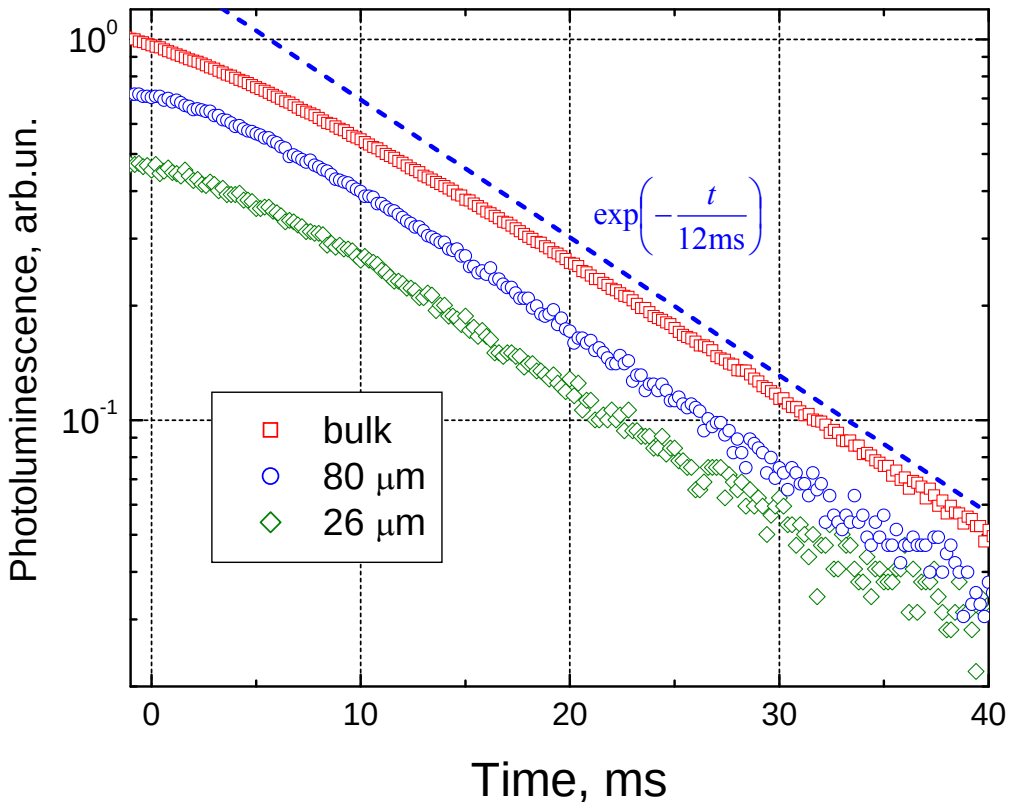

Figure 5.12: PL decay time, in bulk and powdered samples, at 1550 nm emission corresponding to the $^4I_{13/2} \rightarrow {}^4I_{15/2}$ transitions. Excitation source used is an 808 nm laser diode.

Figure 5.13 shows the PL spectra measured in samples of various average particle sizes, $\langle L \rangle$, in the presence of an 808 nm laser excitation. There is no visible change seen in the spectral shape with varying average particle sizes. This once again suggests in-efficient re-absorption of light, which could be attributed to the low absorption coefficient values. It is also worthwhile to note that the shape of the measured PL spectra and the predictions of McCumber theory are in close agreement. From which, it can be concluded that the actual spectral shape of the emission cross section may be determined from the measured PL spectra using even a weakly absorbed excitation in bulk samples.

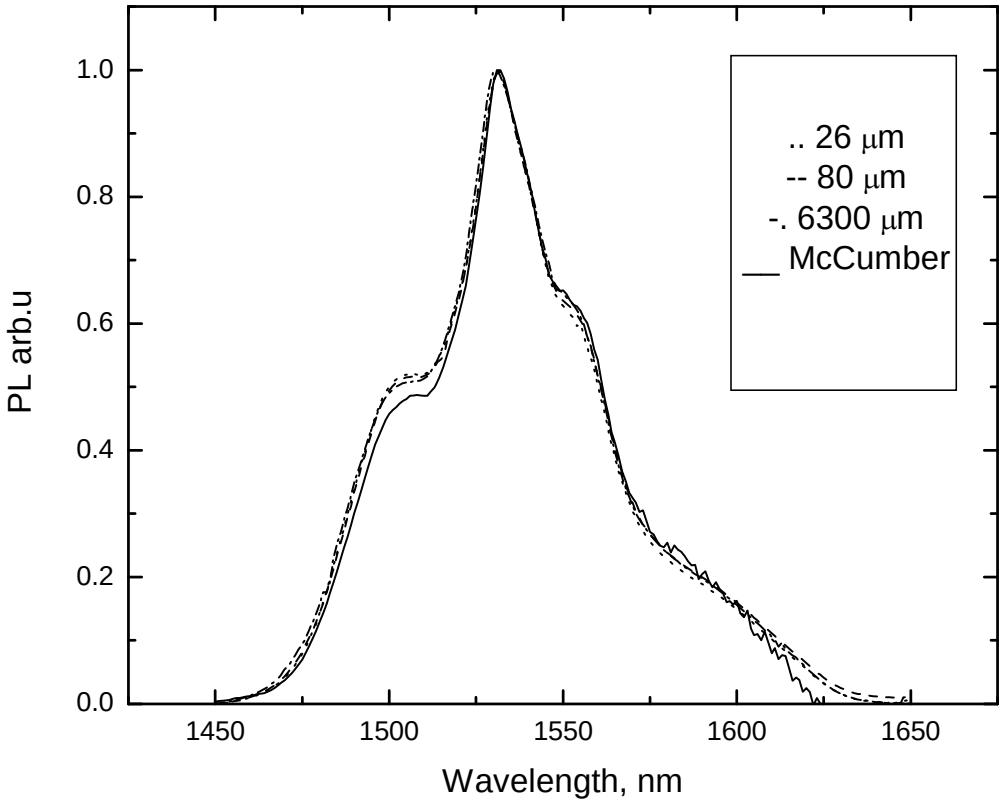

Figure 5.13: Measured PL spectra of various average particle sizes, <*L*>. The excitation source used is an 808 nm laser diode.

Figure 5.14 shows the PL spectrum from 400 – 1650 nm under UV excitation that's centered around 360 nm. All bands are normalized with respect to the 1550 nm emission band. The inset shows the tentative interpretation of the radiative returns. Bright green photoemission, with four peaks at 523, 528, 544 and 550 nm, with a peak intensity that is 60% of the peak intensity of the $^4I_{13/2} \rightarrow {}^4I_{15/2}$ transition is observed. As a result, this material could be suggested as a potential candidate for future applications that would require intense green emission at the above mentioned wavelengths.

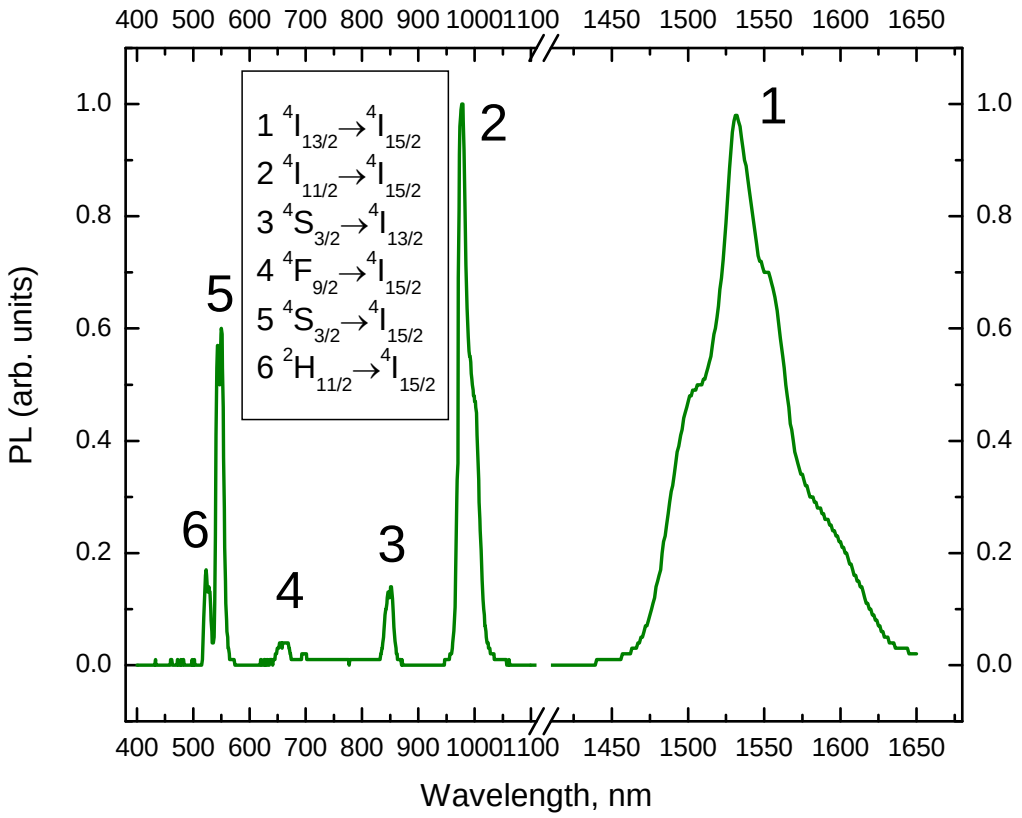

Figure 5.14: Measured PL spectrum of the bulk sample from 400 – 1650 nm. The excitation source used is a UV lamp that's centered around 360 nm. The inset shows the tentative interpretation of the radiative returns.

Introducing somewhat of an ordered structure (crystal like environment) could sometimes produce changes in the measured PL emission. So, annealing is to be performed to convert the glass to a glass ceramic (an amorphous structure with random crystalline incorporations). Before annealing is performed, it is imperative to know at which temperature it should be performed. For which, we turn to Differential Scanning Calorimetry (DSC) to investigate the thermal properties of the material. Figure 5.15, provided by Dr. Tonchev, shows the thermal changes in the sample with increasing temperature. From which, the glass transition temperature is observed to be at

approximately 216 ºC and two crystallization peaks, one at 243 ºC (weak) and the other at 315 ºC (strong), are also observed.

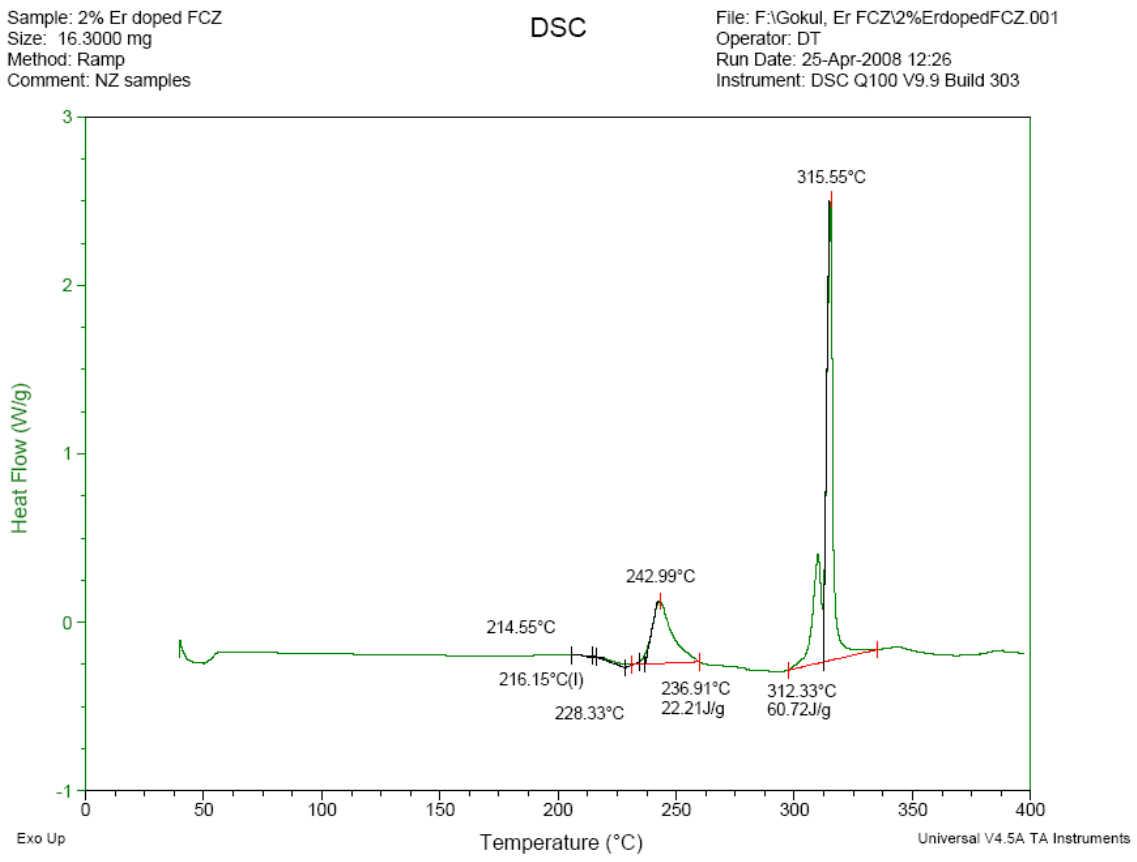

Figure 5.15: Differential Scanning Calorimetry result showing the thermal changes in the material with increasing temperature.

Based on the DSC observations, annealing was performed in nitrogen (inert atmosphere) at 250 ºC. Steady state PL measurements were then performed on the annealed sample using a UV lamp that's centered around 360 nm as the excitation source. Figure 5.16 compares the PL emission spectra, in the visible and near infrared regions, before and after nitrogen annealing. The spectral shapes and intensities don't show major changes. The slight changes may be attributed to the scattering of emitted light by the crystal

inclusions. This suggests that changing the order to some degree doesn't have any effect on the PL emission of the sample.

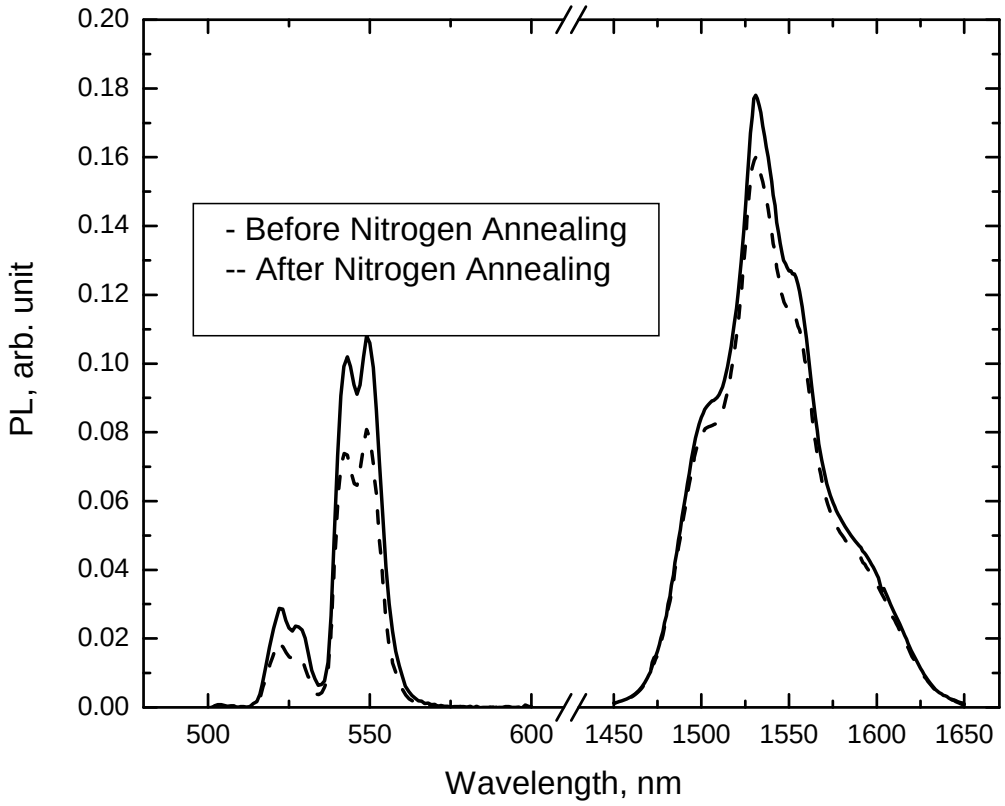

Figure 5.16: Comparison of the measured PL emission spectra, in the visible and near infrared regions, before and after nitrogen annealing. The excitation source used is a UV lamp that's centered around 360 nm.

Another piece of sample was annealed in hydrogen at 250 ºC. Introducing hydrogen in the melt during sample preparation changes the state of RE ions from trivalent to divalent. However, here, we have annealed the prepared sample in hydrogen to observe any changes in the state of the RE ions. Figure 5.17 compares the PL emission spectra, in the visible and near infrared regions, before and after hydrogen annealing. Once again,

there are no major changes in the spectral shapes and intensities. Therefore, it can be concluded that the state of the rare earth ions remain unchanged. As in the previous case, the minor changes may once again be attributed to the scattering of emitted light by the crystal inclusions. From which, it can be concluded that the erbium ions remain in their trivalent state.

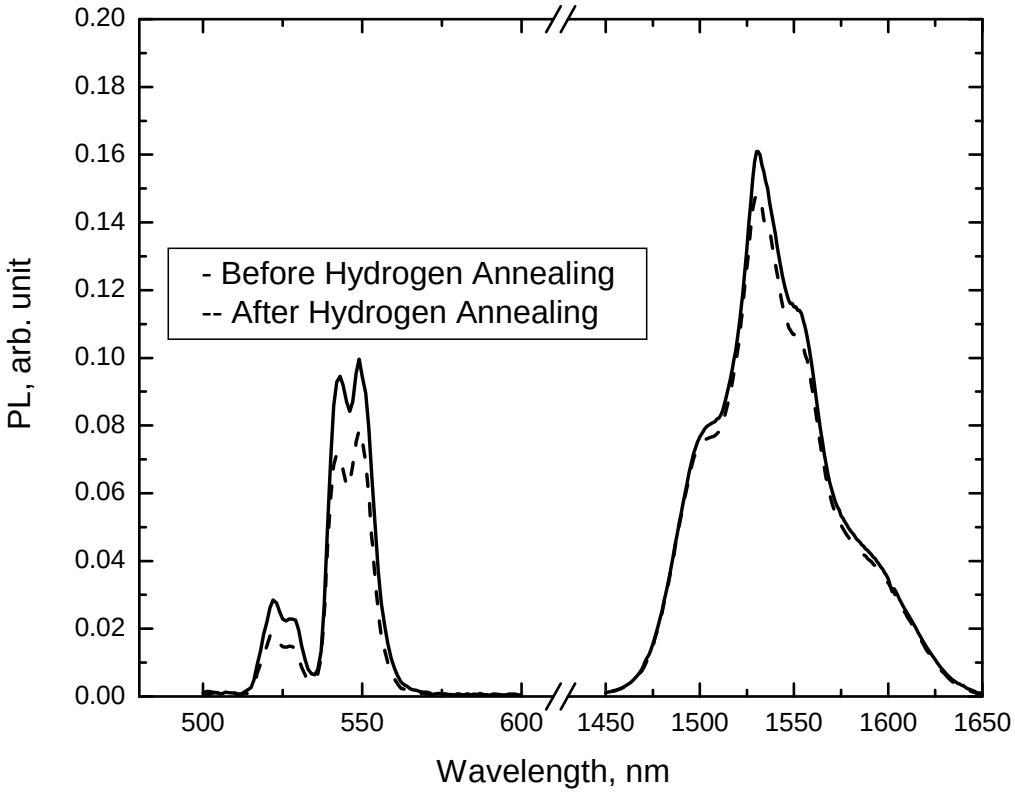

Figure 5.17: Comparison of the measured PL emission spectra, in the visible and near infrared regions, before and after hydrogen annealing. The excitation source used is a UV lamp that's centered around 360 nm.

6. CONCLUSIONS

Recently there has been a substantial renewed interest in the optical characterization of rare earth doped glasses due to their use as optical amplifiers in telecommunications and integrated optics. In this project, we have optically characterized various rare earth doped bulk glasses prepared either in our own laboratory or by our colleagues elsewhere in the world.

The transmission spectra, $T(\lambda)$, was used in identifying the absorption transitions of rare earth ions from the ground level to the various excited levels and in obtaining the optical absorption coefficient, $\alpha(\lambda)$. This in turn was used in determining the Judd-Ofelt parameters, which were then used in obtaining radiative lifetimes of the energy levels of interest. Photoluminescence emission bands were also identified and their shapes were investigated. Finally, a comparison of the JO lifetime with the experimental decay time was also done. From which, the major decay mechanism of the rare earth ions from the energy level under investigation was concluded.

Table 6-1: Summary of results for GLS:Nd glass.

Transmittance in the visible and near IR wavelengths	N_i (cm^{-3})	Ω_2 ($\times 10^{-20}$ cm^2)	Ω_4 ($\times 10^{-20}$ cm^2)	Ω_6 ($\times 10^{-20}$ cm^2)	τ_{JO} (μs) $^4F_{3/2}$	τ_D (μs) $^4F_{3/2}\rightarrow{}^4I_{9/2}$ $^4F_{3/2}\rightarrow{}^4I_{11/2}$ $^4F_{3/2}\rightarrow{}^4I_{13/2}$	β $^4F_{3/2}\rightarrow{}^4I_{9/2}$ $^4F_{3/2}\rightarrow{}^4I_{11/2}$ $^4F_{3/2}\rightarrow{}^4I_{13/2}$ $^4F_{3/2}\rightarrow{}^4I_{15/2}$
~ 65 - 70 % (Sample thickness, d = 2 mm and refractive index, n = 2.23)	8.9×10^{19}	6.9	2.9	1.7	87	86 91 89	0.546 0.384 0.068 0.002

Table 6-1 summarizes the results obtained for GLS:Nd glass. A reasonably high transmission in the visible and near infrared wavelengths is observed, which is definitely a positive feature for optical amplifiers and other optical components. From the JO parameters, it can be concluded that the glass is covalent in nature with a rather "flexible" host matrix. Finally, the closeness of the JO lifetime and the decay times for the $^4F_{3/2}$ excited level suggests that the dominant relaxation mechanism of Nd^{3+} ions from this level is by radiative emission. This along with the values of the lifetimes itself (reasonably large on atomic scale) at 897, 1100 and 1350 nm corresponding to $^4F_{3/2} \rightarrow {}^4I_{9/2}$, $^4F_{3/2} \rightarrow {}^4I_{11/2}$ and $^4F_{3/2} \rightarrow {}^4I_{13/2}$ transitions suggest that this glass could be a potential candidate for optical amplification at these wavelengths.

Table 6-2: Summary of results for GeGaS:Er glass.

Transmittance in the visible and near IR wavelengths	N_i (cm^{-3})	Ω_2 ($\times 10^{-20}$ cm^2)	Ω_4 ($\times 10^{-20}$ cm^2)	Ω_6 ($\times 10^{-20}$ cm^2)	τ_{JO} (ms) $^4I_{13/2}$	τ_D (ms) $^4I_{13/2} \rightarrow {}^4I_{15/2}$ Powdered Sample	β $^4I_{13/2} \rightarrow {}^4I_{15/2}$
~ 65 - 70 % (Sample thickness, d = 2.78 mm and refractive index, n = 1.94)	2.1×10^{20}	10.5±1	3±0.3	1.6±0.2	2.5	2.56	1

Table 6-2 summarizes the results obtained for GeGaS:Er glass. Again, a reasonably high transmission is observed in the visible and near infrared wavelengths, which shows promising use of this glass as an optical amplifier and other optical devices. The JO parameters conclude the nature of the glass to be covalent with a rather "flexible" host matrix. The 1550 nm emission band is broad and strong, which allows for more signal wavelengths to be multiplexed in telecommunications. Finally, the closeness of JO

lifetime and the decay time for the $^4I_{13/2}$ manifold suggests that the dominant relaxation mechanism of Er^{3+} ions from this level to the $^4I_{15/2}$ manifold is via radiative emission. Again, this closeness along with the value of the lifetime itself (relatively large on atomic scale) at 1550 nm corresponding to the $^4I_{13/2} \rightarrow {}^4I_{15/2}$ transition suggest the potential use of this glass for optical amplification at this wavelength.

Table 6-3: Summary of results for FCZ:Er glass.

Transmittance in the visible and near IR wavelengths	N_i (cm^{-3})	Ω_2 ($\times 10^{-20}$ cm^2)	Ω_4 ($\times 10^{-20}$ cm^2)	Ω_6 ($\times 10^{-20}$ cm^2)	τ_{JO} (ms) $^4I_{13/2}$	τ_D (ms) $^4I_{13/2} \rightarrow {}^4I_{15/2}$	β $^4I_{13/2} \rightarrow {}^4I_{15/2}$
~ 90 % (Sample thickness, d = 0.71 mm and refractive index, n = 1.64)	4.64×10^{20}	0.6±0.1	0.9±0.2	1.9±0.3	11±1	12	1

Table 6-3 summarizes the results obtained for FCZ:Er glass. Very high transmission is observed in the visible and near infrared wavelengths, which is very promising for the use of this glass in optical amplifiers and other optical elements. The JO parameters conclude the nature of the glass to be very ionic with a relatively rigid host matrix. Once again, the 1550 nm emission band is observed to be quite broad and intense, which helps in multiplexing more signal wavelengths in telecommunications. Just as in the previous two materials, the JO lifetime and the decay time for the $^4I_{13/2}$ manifold is seen to be very close, which suggests that the dominant relaxation mechanism of Er^{3+} ions is through radiative emission to the $^4I_{15/2}$ manifold. Once again, this along with the really large value of the lifetime (very large on atomic scale) at 1550 nm corresponding to the $^4I_{13/2} \rightarrow {}^4I_{15/2}$

transition suggest that this glass could be an excellent candidate for optical amplification at this wavelength.

7. REFERENCES

1. R. M., *Photonics: Linear and Nonlinear Interaction of Laser Light and Matter*, Springer-Verlag Berlin Heidelberg, 1-9, 2001.

2 . T. Allen, "Experimental and Theoretical Study of Chalcogenide Glasses for Erbium-Doped Waveguide Amplifiers," M. Sc. Thesis, *University of Alberta*, Edmonton, Canada, 2004.

3. Ray DeCorby, "Glasses for Photonic Integration," in *Springer Handbook of Electronic and Photonic Materials*, S. Kasap and P. Capper, Ed. Springer Science + Business Media Inc., New York , 1041-1061, 2006.

4. W. Tan, "Optical Properties of Amorphous Selenium Films," M. Sc. Thesis, U*niversity of Saskatchewan*, Saskatoon, Canada, 2006.

5. A. Zakery and S. R. Elliot, "Optical properties and applications of chalcogenide glasses: a review," *Journal of Non-Crystalline Solids*, **330**, 1-12, 2003.

6. M. Munzar, K. Koughia, D. Tonchev, S. O. Kasap, T. Sakai, K. Maeda, T. Ikari, C. Haugen, R. DeCorby and J. N. McMullin, "Influence of Ga on the optical and thermal properties of Er_2S_3 doped stoichiometric and nonstoichiometric Ge-Ga-Se glasses," *Physics and Chemistry of Glasses* , **46** (2), 215-219, 2005.

7. B. G. Aitken, C.l W. Ponader and R. S. Quimby, "Clustering of rare earths in GeAs sulfide glass," *C. R. Chimie*, **5**, 865-872, 2002.

8. Y. D. Huang, M. Mortier and F. Auzel, "Stark level analysis for Er^{3+} doped ZBLAN glass," *Optical Materials*, **17**, 501-511, 2001.

9. L. Hwa and C. Shu, "The structural Investigation of a ZBLAN Glass by Vibrational Spectroscopy," *Chinese Journal of Physics*, **34**, 1270-1275, 1996.

10. A. Ellison and J. Minelly, "New Materials for Optical Amplifiers," in *Optical Fiber Telecommunications IVA,* Ivan P. Kaminow and Tingye Li, Eds. Academic Press – An Elsevier Science Imprint, 80-174, 2002.

11. G. Androz, M. Bernier, D. Faucher and R. Vallee, "W single transverse mode thulium doped ZBLAN fiber laser at 1480 nm," *Optics Express*, **16**, 16019-16031, 2008.

12. G. Blasse and B.C. Grabmaier, *Luminescent Materials*, Springer – Verlag Berlin Heidelberg, 1-9, 1994.

13. S. O. Kasap, *Optoelectronics and Photonics: Principles and Practices*, Upper Saddle River, New Jersey: Prentice Hall, 2001.

14. H. Kogelnik, "Optical Communication," in *The Optics Encyclopedia*, Th. G. Brown, K. Creath, H. Kogelnik, M. A. Kriss, J. Schmit, M. J. Weber, Eds. WILEY-VCH, Verlag GmbH & Co. KGaA, 1822-1826, 2004.

15. W. J. Miniscalco, "Optical and Electronic Properties of Rare Earth Ions in Glasses," in *Rare-Earth-Doped Fiber Lasers and Amplifiers*, Michel J. F. Digonnet, Ed. Marcel Dekker, Inc., New York, 17-112, 2001.

16. G. C. Righini and M. Ferrari, "Photoluminescence of rare-earth doped glasses," *Rivista Del Nuovo Cimento*, **28**, 1-53, 2005.

17. R. Chang, "Quantum Theory and the Electronic Structure of Atoms" in *Chemistry*, WCB/McGraw-Hill Inc., Unites State of America, 242-279, 1998.

18. S. O. Kasap, "Elementary Materials Science Concepts," in *Principles of Electronic Materials and Devices*, McGraw-Hill Companies, Inc., New York, 3-112, 2006.

19. M. Mayer, "Rare-Earth and Transuranic Elements," *Phys. Rev.*, **60**, 184-187, 1941.

20. S. Hufner, *Optical Spectra of Transparent Rare Earth Compounds*, Academic Press, New York, 1978.

21. S. O. Kasap, H. Ruda, Yann G. Boucher, *Cambridge Illustrated Encyclopedia and Dictionary of Optoelectronics and Photonics*, Cambridge University Press, New York, 118, 2009.

22. G. H. Dieke, and H. M. Crosswhite, "The Spectra of the Doubly and Triply Ionized Rare Rarths," *Applied Optics*, **2**, 675-686, 1963.

23. S. O. Kasap, K. Koughia, J. Singh, H. Ruda and S. K. O'Leary, "Optical Properties of Electronic Materials: Fundamentals and Characterization," in *Springer Handbook of Electronic and Photonic Materials*, S. Kasap and P. Capper, Eds. Springer Science + Business Media Inc., New York , 47-77, 2006.

24. L. A. Riseberg and M. J. Weber, "Relaxation phenomena in rare earth luminescence," in *Progress in Optics*, E. Wolf, Ed. Amsterdam, North Holland Publishing Co., vol. 14, 91-159,1975.

25. B. R. Judd, "Optical Absorption Intensities of Rare-Earth Ions," *Phys. Rev.*, **127**, 750-761, 1962.

26. G. S. Ofelt, "Intensities of Crystal Spectra of Rare-Earth Ions," *J. Chem. Phys.*, **37**, 511-520, 1962.

27. K. Koughia, J. Singh, S. O. Kasap, and H. E. Ruda, "Fundamental Optical Properties of Materials II," in *Optical Properties of Condensed Matter and Applications*, Jai Singh, Ed. John Wiley & Sons Ltd, West Sussex, England, 27-47, 2006.

28. M. J. Weber, "Probabilities for rardiative and nonradiative decay of Er^{3+} in LaF_3," *Physics Review*, **157**, 262-272, 1967.

29. W. T. Carnall, P. R. Fields and B. G. Wybourne, "Spectral Intensities of the Trivalent Lanthanides and Actinides in Solution. I. Pr^{3+}, Nd^{3+}, Er^{3+}, Tm^{3+} and Yb^{3+}," *The Journal of Chemical Physics*, **42**, 3797-3806, 1965.

30. W. T. Carnall, P. R. Fields, and K. Rajnak, "Electronic Energy Levels in the Trivalent Lanthanide Aquo Ions. I. Pr^{3+}, Nd^{3+}, Pm^{3+}, Sm^{3+}, Dy^{3+}, Ho^{3+}, Er^{3+}, and Tm^{3+}," *The Journal of Chemical Physics*, **49**, 4424-4442, 1968.

31. William. F. Krupke, "Induced-Emission Cross Sections in Neodymium Laser Glass," *IEEE J. Quant. Elec*., **QE-10**, 450-457, 1974.

32. William. F. Krupke, "Radiative Transition Probabilities Within the 4f3 Ground Configuration of Nd:YAG," *IEEE J. Quant. Elec*., **QE-7**, 153-159, 1971.

33. Y. Ohishi, "Rare-earth ions in glasses and transitions for optical amplifiers," in *Optical Fiber Amplifiers: Materials, Devices and Applications*, S. Sudo, Ed. Boston: Artech House, Inc., 149-189, 1997.

34. T. Yu. Ivanova, A. A. Man'shina, A. V. Kurochkin, Y. S. Tver'yanovich, V. B. Smirnov, "Er^{3+} to glass matrix energy transfer in Ga-Ge-S:Er^{3+} system," *J. Non-Crys. Solids*, **298**, 7-14, 2002.

35. R. Reisfeld, "Radiative and Non-Radiative Transitions of Rare-Earth Ions in Glasses", in *Rare Earths*, vol. 22 of *Structure and Bonding*, J. D. Dunitz, P. Hemmerich, R. H. Holm, J. A. Ibers, C. K. Jorgensen, J. B. Neilands, D. Reinen, R. J. P. Williams, Ed. Springer-Verlag, New York, 123-175, 1975.

36. L. A. Riseberg and H. W. Moos, "Multiphonon Orbit-Lattice Relaxation of Excited States of Rare-Earth Ions in Crystals," *Physics Review*, **174**, 429-438, 1968.

37. C. B. Layne, W. H. Lowdermilk, and M. J. Weber, "Multiphonon relaxation of rare-earth ions in oxide glasses," *Phy. Rev. B*, **16**, 10-20, 1977.

38. C. B. Layne, and M. J. Weber, "Multiphonon relaxation of rare-earth ions in beryllium-fluoride glass," *Phy. Rev. B*, **16**, 3269-3261, 1977.

39. David P. Machewirth, "Characterization of Novel Rare Earth Doped Laser Glasses," PhD Thesis, *The State University of New Jersey*, New Brunswick, United States of America, 1996.

40. M. Shimizu, M. Yamada, M Horiguchi and E. Sugita, "Concentration Effect on Optical Amplification Characteristics of Er-Doped Silica Single-Mode Fibers," *IEEE Phot. Tech. Lett*., **2**, 43-45, 1990.

41. N. Kagi, A. Oyobe and K. Nakamura, "Efficient Optical Amplifier Using a Low-Concentration Erbium-Doped Fiber," *IEEE Phot. Tech. Lett*., **2**, 559-561, 1990.

42. F. Auzel, "Materials and Devices Using Double-Pumped Phosphors with Energy Transfer," *Proc. IEEE*, **61**, 758-786, 1973.

43. P. C. Becker, N. A. Olsson and J. R. Simpson, "Rare Earth Ions – Introductory Survey," in *Erbium – Doped Fiber Amplifiers: Fundamentals and Technology*, Academic Press, United States of America, 87-120, 1997.

44. M. R. Brown, H. Thomas, J. M. Williams, R. J. Woodward and W. A. Shand, "Experiments on Er^{3+} in SrF_2. III. Coupled-Ion Effects," *The Journal of Chemical Physics,* **51**, 3321-3327, 1969.

45. L. F. Johnson, H. J. Guggenheim, T. C. Rich and F. W. Ostermayer, "Infrared-to-Visible Conversion by Rare-Earth Ions in Crystals," *J. Appl. Phys.*, **43**, 1125-1137, 1972.

46. A. K. Mairaj, A. M. Chardon, D. P. Shepherd and D. W. Hewak, "Laser Performance and Spectroscopic Analysis of Optically Written Channel Waveguides in Neodymium-Doped Gallium Lanthanum Sulphide Glass," *IEEE J. Sel. Top. Quant. Elec*., **8**, 1381-1388, 2002.

47. C. Koughia, G. Soundararajan, S. Kasap, T. Allen, C. Haugen, R. Decorby, N. Ohrui, T. Aoki, C. Fujihashi, " Characterization of $^4I_{9/2} \leftrightarrow {}^4F_{3/2}$ optical transitions in trivalent Nd^{3+} ions in GaLaS glass," *J. Mater. Sci: Mater Electron*, **20**, S19-S22, 2009.

48. E. Desurvire, "Characteristics of Erbium-Doped Fibers," in *Erbium-doped fiber amplifiers*, John Wiley & Sons, Inc., New York, 219, 1994.

49. D. K. Sardar, R. M. Yow, "Inter-Stark Energy Levels and Effects of Temperature on Sharp Emission Lines of Nd^{3+} in $LiYF_4$," *Phys. Stat. Sol.*, (a) **173**, 521-533, 1999.

50. E- Desurvire, J. R. Simpson, "Evaluation of $^4I_{15/2}$ and $^4I_{13/2}$ Stark-level energies in erbium-doped aluminosilicate glass fibers," *Opt. Lett.*, **15**, 547-540, 1990.

51. D. E. McCumber, "Einstein Relations Connecting Broadband Emission and Absorption Spectra," *Phys. Rev.*, **136**, A954-A957, 1964.

52. W. J. Miniscalco, R. S. Quimby, "General procedure for the analysis of Er^{3+} cross sections," *Opt. Lett.*, **16**, 258-260, 1991.

53. S. Kasap, K. Koughia, G. Soundararajan, and M. G. Birk, "Optical and Photoluminescence Properties of Erbium-Doped Chalcogenide Glasses (GeGaS:Er)," *IEEE J. Sel. Top. Quant. Elec*., **14**, 1353-1360, 2008.

54. *Handbook on the physics and Chemistry of rare Earth*, vol. 25**,** K. A. Gschneider, Jr. and L. R. Eryring, Eds. Elsevier, New York**,** 1998.

55. D. S. Sumida and T. Y. Fan, "Effects of radiation trapping on fluorescence lifetime and emission cross section measurements in solid-state laser media," *Opt. Lett.*, **19**, 1343-1345, 1994.

56. F. Auzel, F. Bonfigli, S. Cagliari, and G. Baldacchini, "The interplay of self-trapping and self-quenching for resonant transitions in solids; role of cavity," *J. Lumin.*, **94/95**, 293-297, 2001.

57. M. Mattarelli, M. Montagna, L. Zampedrl, A. Chiasera, M. Ferrari, G. C. Righini, L. M. Fortes, M. C. Goncalves, L. F. Santosa, and R. M. Almeida, "Self-absorption and radiation trapping in Er^{3+}-doped TeO_2-based glasses," *Europhys. Lett.*, **71**, 394-399, 2005.

58. R. El-Mallawany, A. Patra, C. S. Friend, R. Kapoor, and P. N. Prasad, "Study of luminescence properties of Er^{3+}-ions in new tellurite glasses," *Opt. Mater.*, **26**, 267-270, 2004.

59. M. Munzar, K. Koughia, S. O. Kasap, C. Haugen, R. DeCorby, and J. N. McMullin, "Photoluminescence properties of Er-doped Ge-Ga-Se glasses," *Phys. Chem. Glasses: Eur. J. Glass Sci. Technol. B*, **47**, 220-224, 2006.

60. S. Schweizer, L. W. Hobbs, M. Secu, J-M. Spaeth, A. Edgar, G. V. M. Williams, and J. Hamlin, "Photostimulated luminescence from fluorochlorozirconate glass-ceramics and the effect of crystalline size," *J. Appl. Phys*., **97**, 83522-83531, 2005.